UC Irvine
UC Irvine Electronic Theses and Dissertations

Title
Exploring Directional LL'CT in (donor)M(acceptor) Complexes

Permalink
https://escholarship.org/uc/item/8t457914

Author
Kramer, Wesley William

Publication Date
2014

Peer reviewed|Thesis/dissertation

UNIVERSITY OF CALIFORNIA,
IRVINE

Exploring Directional LL′CT in (donor)M(acceptor) Complexes

DISSERTATION

submitted in partial satisfaction of the requirements
for the degree of

DOCTOR OF PHILOSOPHY

in Chemistry

by

Wesley William Kramer

Dissertation Committee:
Professor Alan F. Heyduk, Chair
Professor Andy S. Borovik
Professor Matthew D. Law

2014

Dedication

To friends and family

Table of Contents

Chapter 3

Metal Influence on LL′CT

Chapter 4

Metal-Donor Interactions: The Role of the Chalcogen

Chapter 5

Computational Study of LL′CT Behavior in (donor)Rh(phdi)X2 Complexes

List of Figures

List of Tables

List of Schemes

ACKNOWLEDGMENTS

Wesley W. Kramer

University of California, Irvine   2912 Adobe Circle
Department of Chemistry   Irvine, CA 92617
1102 Natural Sciences II   303-507-4775
Irvine, CA 92697-2025   wkramer@uci.edu
949-824-7479

Education

University of California, Irvine, CA   2009 – 2014
Ph.D., Chemistry

Research advisor: Prof. Alan F. Heyduk

Ph.D. dissertation: "Employing Redox Active Ligands for the Development of Donor-Acceptor Ligand-to-Ligand Charge Transfer Dyes"

Colorado State University, Fort Collins, CO   2005 – 2009
B.S., ACS-Chemistry

*Research Adviso*r*:* Prof. Mathew P. Shores

Research Experience

University of California, Irvine, Department of Chemistry

Graduate Research Advisor: Prof. Alan F. Heyduk

- Synthesis, characterization and computational analysis of (donor)M(acceptor) complexes for the development of a new family of tunable chromophores. For a more detailed summary of this work please see the included research statement.

Colorado State University, Department of Chemistry

Undergraduate Research Advisor: Prof. Mathew P. Shores

- Preparation of new salophen ligands for use in the preparation of one-dimensional $[(salophen)M(CN)_2]_3$ single-molecule magnet materials.

Publications:

- Kramer, W. W.; Zarkesh, R. A.; Heyduk, A. F. "Using Redox-Active Ligands to Prepare Donor-Acceptor Coordination Complexes" *Manuscript Accepted.*
- Kramer, W. W.; Krull, B. T.; Furche, F. U.; Kirk, M. L.; Heyduk, A. F. "Experimental and Computational Investigation of the Metal Influence in (Donor)M(Acceptor) Coordination Complexes" *Manuscript in preparation.*

Contributed Presentations:

- Kramer, W. W.; Fiedler, S. R.; Shores, M. P. "Work Towards 1-D Linear Single-Molecule Magnets" 237th ACS National Meeting, Salt Lake City, UT, March 24, 2009. (*Poster*)
- Kramer, W. W.; Heyduk, A. F. "Nickel(II) Charge Transfer Complexes of Redox-Active Ligands" 241st ACS National Meeting, Anaheim, CA, March 31, 2011. (*Oral Communication*)
- Kramer, W. W.; Heyduk, A. F. "Donor-Acceptor Complexes of Nickel(II) Based on Redox-Active Ligands" Southern California Inorganic Photochemistry Conference, Catalina Island, CA, September 10, 2011. (*Oral Communication*)

- Kramer, W. W.; Heyduk, A. F. "Group 10 Donor-Acceptor Complexes of Redox-Active Ligands" 243rd ACS National Meeting, San Diego, CA, March 28, 2012. (*Oral Communication*)
- Kramer, W. W.; Heyduk, A. F. "Electronic Trends in Donor-Acceptor Complexes of Group 10 Metals" Southern California Inorganic Photochemistry Conference, Catalina Island, CA, September 7, 2012. (*Oral Communication*)
- Kramer, W. W.; Krull, B. T.; Heyduk, A. F. "Examining Electronic Trends in Donor-Acceptor Complexes of Group 10 Metals" 243rd ACS National Meeting, New Orleans, LA, April 7, 2013. (*Oral Communication*)
- Kramer, W. W.; Shaffer, D. W; Heyduk, A. F. "Computational Investigation of Ligand-to-Ligand Charge Transfer in Octahedral Group 9 (donor)M(acceptor)X2 Complexes" Southern California Inorganic Photochemistry Conference, Catalina Island, CA, September 5, 2013. (*Oral Communication*)

Other Skills and Activities:
- Synthesis and handling of air-sensitive coordination complexes using vacuum-line, Schlenk-line and glovebox techniques.
- Ligand design and synthesis.
- Characterization of compounds using standard NMR, IR and UV-vis-NIR spectroscopic techniques.
- Experienced with electrochemical methods, EPR spectroscopy and X-ray crystallography.
- DFT and TD-DFT computational analysis of complex inorganic molecules.
- Participated in fruitful collaborations with other research groups.
- Assisted in the peer-review process of manuscripts prior to publication.
- Mentored junior graduate students and undergraduate students.

Teaching Experience

University of California, Irvine, Department of Chemistry
- Teaching Assistant, Organic Chemistry Laboratory   Fall 2009 - Winter 2010, Winter 2013
  Taught two, four-hour lab sections which covered basic lab techniques and synthesis. Graded lab reports and final practical exams. Held a weekly office hour
- Teaching Assistant, Inorganic Chemistry Lecture   Spring 2010
  Attended lectures and held three, weekly discussion sections for 10-30 students. Graded homework and exams. Held a weekly office hour.
- Teaching Assistant, General Chemistry Lecture   Fall 2010
  Attended lectures and held five, weekly discussion sections for 20-30 students and developed problems for review. Graded and exams. Held a weekly office hour.
- Teaching Assistant, Inorganic Chemistry Lecture   Winter 2011, 2012
  Attended lectures and held three, weekly discussion sections for 10-30 students. Graded homework and exams. Held a weekly office hour.
- Teaching Assistant, Advanced Inorganic Laboratory   Spring 2012
  Supervised one, seven-hour lab section each week with 12 students which covered synthesis, air-free manipulations and spectroscopy. Graded lab reports and final practical exams. Assisted in improving experiments. Held weekly office hour.
- Teaching Assistant, Graduate Inorganic Chemistry Lecture   Fall 2012
  Attended lectures and held weekly discussion sections for 10-15 students. Graded homework.

References:

Prof. Alan F. Heyduk
Department of Chemistry
University of California
Irvine, CA 92697
949-824-8806
aheyduk@uci.edu

Prof. Andrew S. Borovik
Department of Chemistry
University of California
Irvine, CA 92697
949-824-1510
aborovik@uci.edu

Prof. Matt Law
Department of Chemistry
University of California
Irvine, CA 92697
949-824-5996
matt.law@uci.edu

ABSTRACT OF THE DISSERTATION

Exploring Directional LL′CT in (donor)M(acceptor) Complexes

By

Wesley William Kramer

Doctor of Philosophy in Chemistry

University of California, Irvine, 2014

Professor Alan F. Heyduk, Chair

The overarching theme of the work presented in this dissertation is the to develope a better understanding of the factors which govern the properties of donor-acceptor (D-A) LL′CT transition metal complexes.

Chapter 2 describes a series of (catcholate)Ni(diimine) D-A LL′CT complexes. The spectroscopic and electrochemical properties can be tuned independently through variations in donor or acceptor ligand electronics.

Chapter 3 describes the Group 10 series of (cat-tBu$_2$)M(bdi) complexes (M = Ni(II), Pd(II), Pt(II); cat-tBu$_2$ = 3,5 di-$tert$-butylcatecholate; bdi = N,N'- bis(2,4,6-trimethylphenyl)-butane–2,3-diimine). A combination of experimental and computational analyses revealed that the influence of the metal atom in these complexes is limited to the ability of metal ions to participate in π interactions with the bdi ligand.

Chapter 4 describes the synthesis and characterization of (bdt)M(bdi) and (bds)Pt(bdi), (M = Ni(II), Pd(II), Pt(II); bdt = 1,2-benzenedithiolate, bds = 1,2-benzenediselinolate). In this chapter experimental results are supplemented by computational analysis of the Group 10 series

of both donor-acceptor ligand combinations. The results of these investigations indicate that substitution of oxygen for sulfur as the donor ligand heteroatom lowers the donor-localized molecular orbitals and dramatically decreases the variations observed between complexes of different metal ions. Substitution of sulfur for selenium however cause almost no change spectroscopic and electrochemical behavior of the (bds)M(bdi) complexes from the analogous (bdt)M(bdi) complexes.

Chapter 5 provides a thorough computational analysis in to the LL′CT behavior of a series of (donor)Rh(phdi)X$_2$ complexes. These complexes are a rare example of directional LL′CT in an octahedral complex. It was found that alterations of the donor ligand produced predictable changes in the energy of the donor-localized HOMO of these complexes that mirror similar behavior displayed in more traditional square-planar (donor)M(acceptor) LL′CT complexes.

Chapter 1
Introduction to LL′CT

1.1 Solar energy conversion

Due to the rapidly growing need for clean, carbon-neutral sources of energy there has been significant investment into the design and synthesis of compounds that can capture and convert solar energy directly into electricity or store it as chemical fuels. Photo-induced charge separation is the first required step in any photovoltaic or artificial photosynthetic scheme.[1-3] To convert sun light into useable energy the absorption of a photon must result in the generation of a charge-separated excited state (CSS) composed of an excited electron and its corresponding hole. In photovoltaic cells, these charges flow through a circuit to generate electricity (Figure 1.1). In artificial photosynthesis, the electrons are used to generate fuel, such as H_2, and the holes are uses to form an oxidant, such as O_2. For both applications, the design of light absorbing molecules or materials that generate a CSS is an important area of study.[4,5]

Dye-sensitized solar cells (DSSCs) represent an intriguing photovoltaic technology for the capture of solar energy (Figure 1.1). Grätzel cells are a well studied class of DSSC.[6-9] Devices based on the Grätzel design generate current when an excited dye molecule injects an electron from its CSS into the conduction band of an n-type semi-conductor photoanode which is then extracted to do work. While efficiencies of up to 12% have been achieved with Grätzel DSSCs, increased efficiencies can be achieved by combining an n-type photoanode and a p-type photocathode into a tandem single device.[10] To maximize the solar spectrum used by these tandem cells, it would be desirable to develop a family of tunable chromophores, with complementary absorption and excited-state properties that could be used for both electron and hole injection. At present, no single dye platform is capable of acting as a sensitizer for both photo-electrodes. Such a dye platform must meet several requirements to address the unique design challenges presented by tandem DSSCs. To maximize the incident sun light used by a

tandem device, dyes with complimentary absorption properties are needed.[11,12] Such a dye platform must allow for tunable absorptions where the solar irradiance is most intense, between 400–1200 nm. Directional charge transfer and long-lived excited states are necessary to insure that both the electron and the hole are accessible in the CSS. Finally, dyes based on such a platform should be readily synthesized from inexpensive and abundant materials.[10-16] Currently no molecular dye platform satisfies all of these criteria.
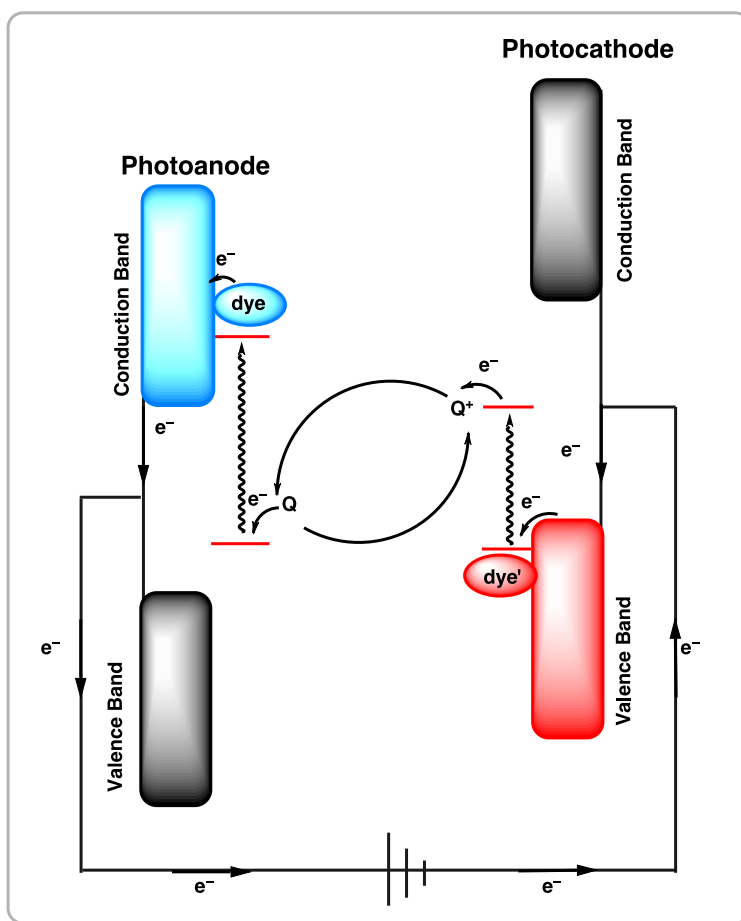
Figure 1.1 Schematic illustrating the mechanism of a tandem DSSC.

1.2 Dyes for Solar Energy Conversion

Dyes that operate via metal-to-ligand charge transfer (MLCT) have received considerable attention in the area of solar energy conversion. The prototypical MLCT chromophore is

$[Ru(bpy)_3]^{2+}$. Its strong absorption at 452 nm corresponds to the transfer of an electron from the ruthenium t_{2g}-like orbitals to π^* orbitals of bipyridine ligand as shown in Figure 1.2.[17-19] These dyes have been successfully exploited as excited state reductants in a number of solar energy conversion systems;[1,6] however, the properties inherent to the MLCT process limit the usefulness of these dyes for other applications. In the CSS, the hole is confined to the t_{2g} orbitals on metal atom, which is 'protected' by the bipyridine ligands, leading to slow hole extraction kinetics.[20] Another shortcoming of MLCT dyes is the limited ability to tune both the HOMO and LUMO. While the LUMO can be tuned through alterations to the bipyridine backbone, the metal-localized HOMO is difficult to tune.[19-22] Also, ruthenium itself is an expensive material. This limits the commercial viability of solar energy conversion schemes which rely on these dyes. While ruthenium polypyridine complexes have become the gold standard of chromophores for electron injection applications these dyes do not meet the requirements for the 'ideal chromophore' laid out above.
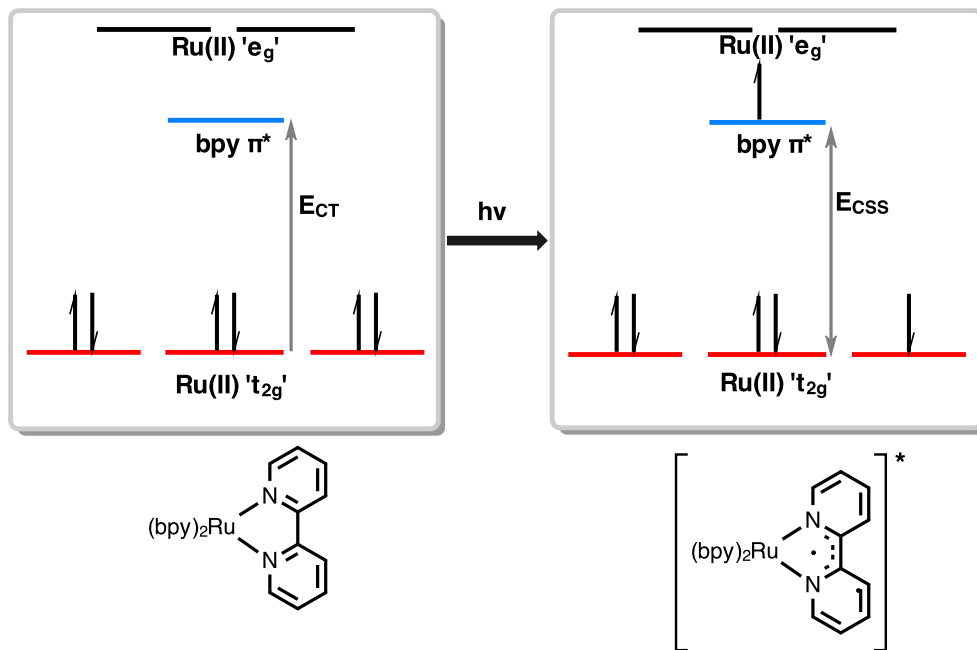
Figure 1.2. MLCT process of in $[Ru(bpy)_3]^{2+}$. E_{hv} is the energy of the absorbed photon, E_{CSS} is the energy stored in the CSS.

Donor-chromophore-acceptor molecular triads (D-C-A) are another well studied category of dyes for photochemical charge separation.[1,2,23-26] This dye design generates a CSS in a similar fashion as in natural photosynthetic systems. Absorption of a photon by the chromophore component forms an excited D–C*–A species. An electron transfer cascade reaction then takes place where the excited chromophore transfers an electron to the acceptor fragment and the donor fragment fills the hole generated on the chromophore to afford a charge-separated state: (D+-C–A−) as shown in Figure 1.3. These D-C-A triads display a number of desirable properties including directional charge transfer, well separated hole and electron pairs, and long-lasting CSSs. Despite these attractive features, DCA triads are limited by difficult and lengthy synthetic procedures and by the fact that light absorption does not directly result in the generation of a CSS. Because the HOMO of the chromophore must be lower in energy than the donor HOMO

and the chromophore LUMO must be higher energy than the acceptor LUMO in order for the electron transfer cascade to take place, the energy stored in the CSS (E_{CSS}) is necessarily less than the energy of the absorbed photon (E_{CT}). This fact significantly limits the efficiency of these dyes and is a major detractor to these systems as a whole.
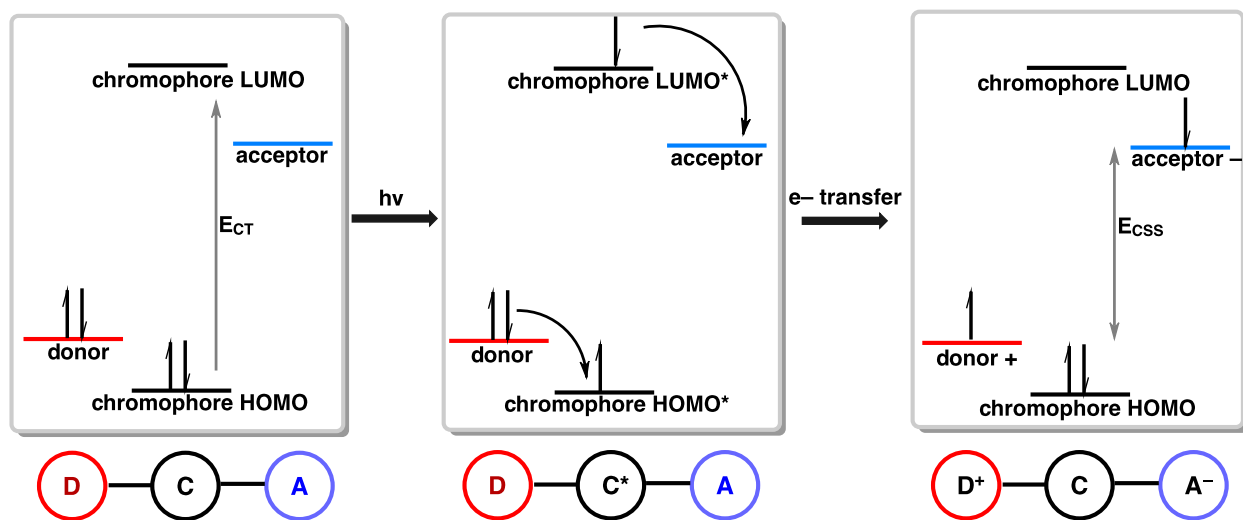
Figure 1.3. Photo-induced electron transfer in a D-C-A triad to generate a CSS. $E_{h\nu}$ is the energy of the absorbed photon, E_{CSS} is the energy stored in the CSS.

1.3 LL′CT Dyes

Complexes that display direct ligand-to-ligand charge-transfer (LL′CT) represent a possible third dye class for photo-induced charge separation.[13,27-29] LL′CT dyes incorporate desirable features of both MLCT and D-C-A triad designs. As shown in Figure 1.4 light absorption directly generates a CSS, and the photo-generated hole and electron are well separated and accessible. LL′CT dyes incorporate an electron-rich donor ligand and an electron-poor acceptor ligand coordinated to a transition metal ion and are designed so that the HOMO is located predominantly on the donor ligand and the LUMO is located predominantly on the acceptor ligand. This electronic configuration necessitates that the metal *d* orbitals be energetically removed from the ligand-based frontier orbitals in order to avoid low-energy,

metal-based excited states that can deactivate the CSS. Additionally, D-A LL′CT dye molecules must adopt a coplanar arrangement of the donor and acceptor ligands to maximize the probability of the LLCT. Deviations from square-planar towards tetrahedral coordination geometries of the ligands about the metal center deactivate the LL′CT absorption until it is entirely symmetry forbidden when the ligands are orthogonal to one another.[30,31] Because of these restrictions, d^8 transition metal ions such as palladium(II) and platinum(II) make up a large majority of metal ions used for these dyes due to their propensity to adopt square-planar coordination geometries. [32-34] While coordination complexes that display LL′CT absorptions are not uncommon in the literature,[30-36] they have not received nearly the same degree of interest as the MLCT and D-C-A triad dyes described above. A fundamental understanding of the role and influence of each component must be developed in order for LL′CT dyes to become viable alternatives to MLCT dyes or D-C-A triads. Progress in this area could have a significant impact on the design of new chromophores for solar energy conversion applications.
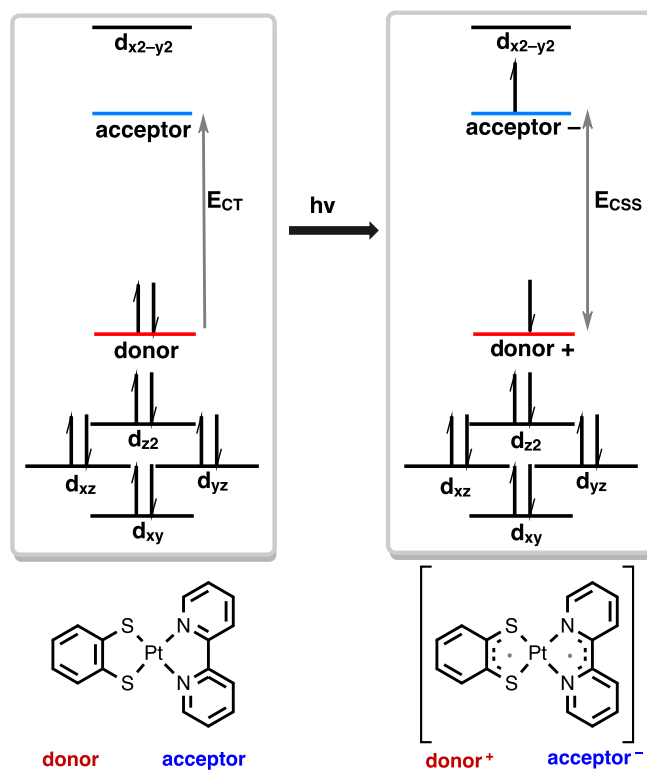
Figure 1.4. Generation of a CSS by LL′CT. E_{CT} is the energy of the absorbed photon, E_{CSS} is the energy stored in the CSS.

Every donor-acceptor LL′CT dye is built from three unique components; the donor ligand, the acceptor ligand and the metal ion. The key feature of D-A LL′CT dyes is that the HOMO and LUMO of the chromophores reside predominantly on the donor ligands and acceptor ligands, respectively. An obvious consequence of this design is that the spectroscopic and electrochemical properties of LL′CT chromophores are in large part dictated by the electronic properties of the ligands. Though, it may be an oversimplification to describe the metal ions role in a D-A LL′CT dye as a scaffold which serves to maximize communication between the donor and the acceptor, this statement provides a useful lens through which to examine the vast majority of the research in this field. Significant insight can be gained into the mechanics of LL′CT dyes by focusing solely on the properties imparted by the donor and acceptor ligands.

1.3.1 (dithiolene)Pt(diimine) Complexes

The first report of ligand-to-ligand charge transfer was by Miller and Dance in 1973 for (dithiolene)Ni(diimine) systems;[37] however, platinum dithiolene-bipyridine complexes (Figure 1.5) were the first class of D-A complexes to garner considerable attention.[30,35,38-41] Eisenberg and co-workers' investigations into the donor-acceptor LL′CT properties displayed by (dithiolene)Pt(diimine) complexes were instrumental in developing a fundamental understanding of how these dyes operate. These complexes are characterized by intense charge-transfer absorptions that display strong solvent dependence on the absorption energy. Luminescence from a mixed metal/dithiolene state is often observed at room temperature and 77 K.[40] Eisenberg and coworkers showed that through systematic variations to the donor and acceptor ligands the energy of the LL′CT absorption and the resulting emission can be tuned across the visible region of the spectrum.[40] Complexes **1-6**, shown in Figure 1.5, each display intense LL′CT absolutions and ligand-centered electrochemistry. The absorption maxima of the LL′CT transitions of these D-A dyes can be tuned over a range of nearly 1 eV.
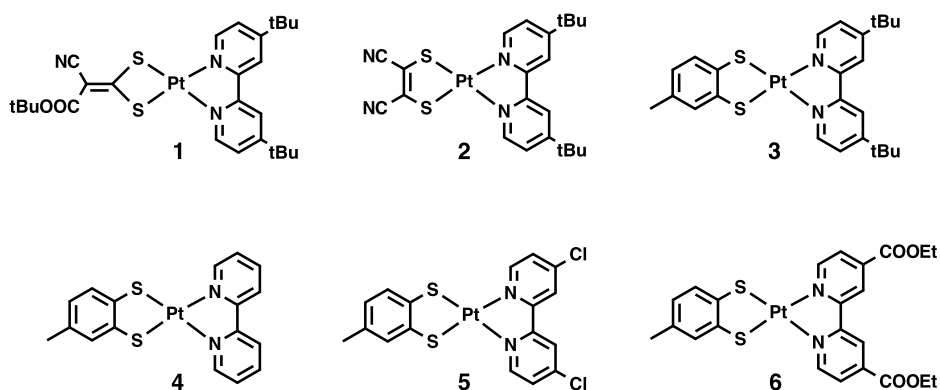
Figure 1.5. (dithiolene)Pt(diimine) donor acceptor complexes **1-6**.

The (donor)Pt(acceptor) complexes **1-3** share the 4,4′-di-*tert*-butyl–2,2′-bipyridine (tBu-bpy) acceptor ligand paired with three different dithiolene donors. Of these three complexes, the dye with the most electron-rich donor 3-tolyldithiolene (tdt), complex **3**, displayed the lowest energy LL′CT transition at 563 nm (2.20 eV), and complex **1**, which uses the most electron poor donor, 1-(*tert*-butylcarboxy)-1-cyanoethylene-2,2-dithiolate (tbcda), showed the highest energy LL′CT absorption (437 nm, 2.84 eV). The LL′CT transition of the intermediate complex, **2**, fell at 497 nm, 2.49 eV. These complexes illustrate that the HOMO energy is determined by the dithiolene ligand, and that when the acceptor is held constant, the LL′CT absorption energy can be tuned by altering the electronics of the donor ligand.

The influence of the acceptor is demonstrated by platinum complexes **3-6**. In this group of complexes, the tdt donor ligand was kept constant and combined with bipyridyl acceptors with substituents in the 4 and 4′ positions, which vary from electron donating to strongly electron withdrawing. The LL′CT absorptions range from 563 nm, with complex **3** where the substituents are the slightly electron donating *tert*-butyl groups, to 679 nm (1.83 eV) for (tdt)Pt(COOEt-bpy), complex **6** (COOEt-bpy = 2,2'-bipyridine-di-4,4'-ethyl ester), which has strongly electron withdrawing –COOEt groups. Complexes **3-6** show that the LL′CT energy and the HOMO-LUMO gap can be tuned by raising or lowering the bipyridyl centered LUMO relative to the donor localized HOMO.

An electrochemical estimate of the HOMO-LUMO gap can be obtained from the difference between the potential of the first oxidation and first reduction (ΔE). In complexes **1-6** ΔE is strongly correlated to the energy of the LL′CT, and the substituent effects discussed above also are observed in the electrochemistry of complexes **1-6**. The potentials of the oxidative and reductive processes observed for these complexes are strongly dependent on the identity of the

donor and acceptor ligands, respectively. Complexes with the most electron-rich donors displayed oxidative processes at less positive potentials than did complexes with electron poor donors. Complexes with electron poor diimine ligands were reduced at less negative potentials than those with more electron-rich acceptors. Changes in the potentials of the oxidative events do not result in significant changes to the reductive events and vice versa, demonstrating the energies of the HOMO and the LUMO can be tuned independently.

1.3.2 Other donor-acceptor Combinations

The dithionlene-bipyridyl ligand combination has been studied extensively, but D-A LL′CT behavior has been also observed with a number of other donor and acceptor ligand combinations. This section will present alternative donor-acceptor combinations that exemplify the different kinds of ligands which can be employed as donors or acceptors to achieve D-A LL′CT behavior.

1.3.2.1 Aryl-E and 1,2-Aryldichalcogenide (E = O,S, Se) Donor Ligands

Donor-acceptor behavior has been demonstrated by complexes with two mono-dentate thiophenol donor ligands (Figure 1.6).[35,42-47] For example, the D-A complex **7**, (tbpS)$_2$Pt(dp-phen) (tbpS = 4-*tert*-butylbenzenethiolate, dp-phen = 7-diphenyl-1,10- phenanthroline), displays an LL′CT absorption at 510 nm (2.43 eV).[42] The LL′CT absorption of **7** is blue-shifted from the analogous dithiolene complex (dtbdt)Pt(dp-phen), **8** (dtbdt = 3,5 di-*tert*-butylbenzenedithiolate), which displays its LL′CT absorption maxima at 634 nm (1.96 eV). The HOMO in complex **7** is localized on both arylthiolate ligands and the platinum *d* orbitals, the same general HOMO composition as observed for D-A complexes with bidentate dithiolene donors. The authors of this study attributed larger metal contribution to the HOMO of complex **7** as the cause of the blue-

shifted LL′CT absorption from its dithiolene analogue, because increased mixing with the metal

d orbitals in the HOMO lowers the energy of the orbital relative to the acceptor localized LUMO.
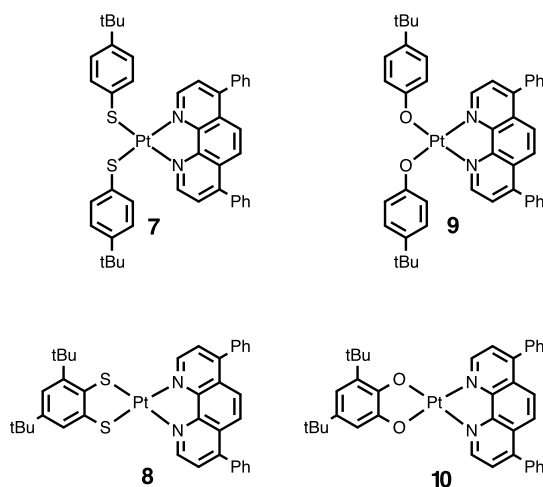
Figure 1.6. Mono- and bidentate sulfur and oxygen donor ligands.

This same study also presents another category of donor ligands in which oxygen

replaces sulfur as the chalcogen heteroatom in the donor ligand(s) as shown in Figure 1.6. The

oxygen containing analogues of **7** and **8**, (tbpO)$_2$Pt(dp-phen), **9,** and (cat-tBu$_2$)Pt(dp-phen), **10**,

respectively (tbpO = 4-*tert*-butylphenolate, cat-tBu$_2$ = 3,5-di-*tert*-butylcatechlate) also display

strong LL′CT absorptions in the visible region.[42] The LL′CT absorption of the catecholate

complex, **10**, is red-shifted (657 nm, 1.89 eV) from the dithiolene complex, **8**. The red-shifted LL

′CT band suggests that the donor-centered HOMO of complex **10** is higher energy than for

complex **8**. The opposite relationship was displayed between the bis-phenolate and bis-

thiophenolate complexes. The LL′CT absorption observed for the bis-phenolate complex, (470

nm, 2.64 eV) is blue-shifted from the bis-thiophenolate complex. The blue-shift in the LL′CT for

the bis-monodentate complex from the mono-bidentate complex is larger when the chalcogen in

donor ligand is oxygen than when it is sulfur because while the π systems of the oxygen based

ligands may be higher energy than their sulfur counterparts, the increase in *d* orbital character in

the HOMO of (tbpO)$_2$Pt(dp-phen) from (cat-tBu$_2$)Pt(dp-phen) is greater than between (tbpS)$_2$Pt(dp-phen) and (dtbdt)Pt(dp-phen). Oxygen-based donor ligands are not well studied in the literature however the work of Srivastava, Weinstein and others concerning catecholate D-A systems show that these complexes can serve as viable alternatives to the more widely used sulfur based donor ligands.[42,48-52] Given that catecholates are generally less oxygen sensitive than dithiolates, D-A complexes with catecholate donors may provide a route to more robust chromophores.

The platinum(II) D-A complexes **1-10** demonstrate that, when paired with a diimine acceptor, both oxygen and sulfur can serve as the donor ligand chalcogen heteroatom in the to achieve D-A LL′CT behavior. The chalcogen series of donor ligands has also been extended to include selenium,however heteroleptic Group 10 diselenolene complexes are quite rare.[53-57] Complex **11a**, (bds)Pt(bpy) (bds = 1,2 benzenediselenol), is a rare but informative example of a diselenolene used as the donor in a D-A LL′CT chromophore.[53] The LL′CT absorption observed for **11a** occurred at 590 nm (2.10 eV), this is almost exactly the same as its analogue dithiolene analogue (bdt)Pt(bpy), **11b** (bdt = 1,2-benzenedithiolate). Identical behavior is observed for the (PhE)$_2$Pt(Me$_2$bpy) complexes, **12a-b** [E: Se = benzeneselenate (**12a**) or S = thiophenolate (**12b**); Me$_2$bpy = 4,4′-dimethyl-2,2′-bipyridine), and the difference in LL′CT absorption maxima between **12a** and **12b** is slight. Unlike the large changes in D-A behavior cause by the substitution of oxygen for sulfur, the substitution of sulfur for selenium has almost no effect on D-A behavior in non-dynamic measurents; however a recent study by Shultz and Kirk shows that selenium substituion has a fairly large effect on the lifetimes of the LL′CT excited states.[54] Unfortunately, due to the lack of literature investigating selenium based D-A LL′CT complexes,

the reason for the all but identical absorption characteristics of sulfur- and selenium-containing

D-A LL′CT chromophores is not well understood.

E = Se **11a**; E = S **11b**   E = Se **12a**; E = S **12b**
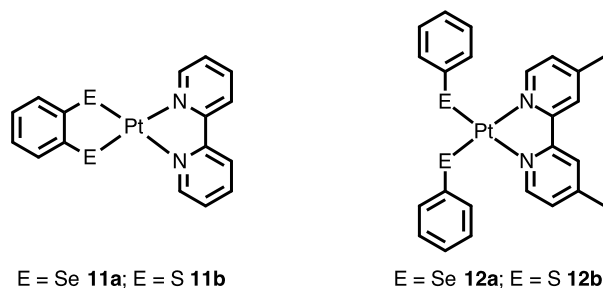
Figure 1.7. Selenium containing D-A LL′CT complexes **11a** and **12a** and their sulfur analogues **11b** and **12b**.

1.3.2.2 Non-bipyridyl Acceptors

The complexes discussed above all employ bipyridyl-type acceptor ligands. Weinstein and coworkers have shown that incorporating the α-diimine acceptor adi (*N*,*N*-diaryl-acenaphthenediimine) with tdt as the donor red-shifts the LL′CT absorption of (tdt)Pt(adi), **13**, compared to complex **6**, the most red-absorbing dye dithiolene-bipyridyl complex, to 748 nm (1.66 eV).[58] A large positive shift in the potential of the first reduction of **7** to –0.62 V vs NHE from –0.96 V vs. NHE for **6** is evidence that the red-shift in the LL′CT absorption in **13** can be attributed to lower energy π* orbitals in the α-diimine acceptor, and therefore the LUMO, compared to the bipyridyl acceptors. Complex **13** indicates that incorporating α-diimine acceptor ligands, in place of the traditional bipyridyl ligands, in D-A LL′CT complexes is a viable route to the synthesis of more red-absorbing dyes which are highly sought after for solar energy conversion applications.[11,12]
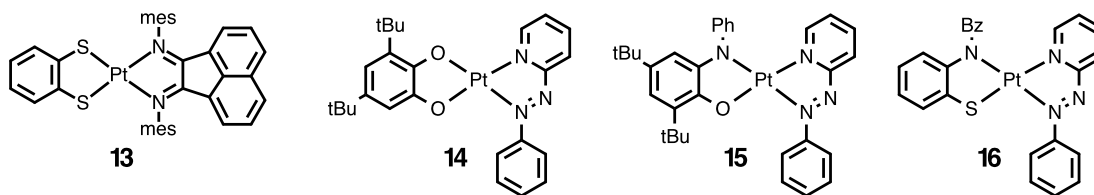
Figure 1.8. D-A LLCT complexes with non-bipyridyl acceptor ligands.

Another ligand that has recently received attention as a donor in D-A LL′CT chromophores is phenylazopyridine (pap). This ligand has been used as an acceptor in platinum complexes with catecholate, amidophenolate, and amidothiophenolate donors as shown in Figure 1.8.[50,51] The LL′CT absorption maxima of complex **14**, (cat-tBu$_2$)Pt(pap), in DCM solution is observed at 970 nm (1.28 eV), which is significantly red-shifted from the analogous catecholate-bipyridyl complex **10** (657 nm, 1.89 eV). Given that catecholate donor and the platinum metal center are the same in both complexes, the red-shift is due to the differences in the energy of the the acceptor ligand π* orbitals where E_{π^*} dp-phen > pap; the shift in the first reduction of complex **14** to less negative potentials vs Fc$^{+/0}$ compared to **10** is further evidence of the lower energy π* orbitals of the pap acceptor.

Aminophenolates are a class of redox-active ligands which are isoelectronic to catecholates. It has been shown that exchange of a catecholate oxygen for nitrogen (Ph-N) raises the energy of the aminophenolate HOMO from the HOMO of catecholate.[59,60] Incorporating an amidophenolate as a donor could with an acceptor like pap could push the LL′CT absorption of a D-A dye further into the NIR. Interestingly, the amidophenolate complex (ap-tBu$_2$)Pt(pap), **15** (ap-tBu$_2$ = 3,5-di-*tert*-butylaminophenolate), displays a strong absorption at 897 nm (1.38 eV), which is blue-shifted from the LL′CT absorption of **14**. At first glance this is a counterintuitive result; the higher energy donor orbital of amidophenolate should decrease the HOMO-LUMO gap of **15**, relative to **14** resulting, in a lower energy LL′CT absorption. Complex **15**

demonstrates the limits of the donor-acceptor model because in this case, the smaller HOMO-LUMO gap results in delocalization of electron density across the molecule and the donor-acceptor model, as defined above, requires that both ligands be electronically isolated and the ground-state of **15** is more similar to bis(dithiolene) complexes than dithiolene-diimine D-A LL′CT complexes.[34] It is possible that D-A behavior could be achieved using an amidophenolates as the donor ligands if they were paired with an acceptor, like bpy, with higher energy π^* orbitals but in this case the pap π^* orbitals are too close in energy to the filled π orbitals of ap-tBu$_2$. The recently reported (bz-atp)Pt(pap), **16** (2-amido-thiophenolate) does display an LL′CT at 855 nm (1.45 eV).[61] In this case the substitution of oxygen for sulfur lowers the acceptor-based HOMO enough that the donor and acceptor ligands are sufficiently electronically isolated from one another.

Table 1.1. Spectroscopic and electrochemical data for complexes **1-16**.

Complex	Formula	λ_{max}	$E^{+/0}$	$E^{0/-}$	ΔE
1	(tbcda)Pt(tBu-bpy)	437 (2.84)	-1.3	0.96	2.26
2	(mnt)Pt(tBu-bpy)	497 (2.49)	-1.27	0.94	2.21
3	(tdt)Pt(tBu-bpy)	563 (2.20)	-1.38	0.39	1.77
4	(tdt)Pt(bpy)	586 (2.12)	-1.34	0.38	1.72
5	(tdt)Pt(Cl-bpy)	630 (1.97)	-1.04	0.38	1.42
6	(tdt)Pt(COOEt-bpy)	679 (1.83)	-0.96	0.41	1.37
7	(tbpS)	510 (2.43)	-1.28	0.45	1.73
8	(dtbdt)Pt(dp-phen)	634 (1.96)	-1.22	0.59	1.81
9	(tdpO)	470 (2.64)	-1.60	0.40	2.00
10	(cat-tBu	657 (1.89)	-1.42	0.22	1.64
11a	(bds)Pt(bpy)	590 (2.10)	-1.78	-0.21	1.57
11b	(bdt)Pt(bpy)	598 (2.07)	-1.8	0.03	1.83
12a	(phSe)	536 (2.31)	N/A	N/A	N/A
12b	(phS)$_2$	524 (2.36)	N/A	N/A	N/A
13	(tdt)Pt(adi)	697 (1.83)	-0.62	1.00	1.62
14	(cat-tBu	970 (1.28)	-0.94	0.12	1.06
15	(ap)Pt(pap)	897 (1.38)	-1.19	-0.09	1.10
16	(bz-atp)Pt(pap)	855 (1.45)	-0.71	0.54	1.25

1.3.3 Building a Ligand 'Toolkit' for D-A LL′CT Dyes

The D-A LL′CT complexes **1-16** illustrate the control over spectroscopic and electrochemical properties that can be obtained through the use of different donor-acceptor ligand combinations. Figure 1.9 summarizes all the different studies discussed in the form of a 'spectrochemical series' for the donor and acceptor ligands presented in this chapter. Table 1.1 contains the absorption maxima, potentials of the first oxidation and first reduction, and ΔE for complexes **1-16**. From these data, we can begin to gather a catelogue of donor and acceptor ligands that can be used in LL′CT dyes, and represents the beginnings of a catalogue for D-A LL

'CT complexes from which one could pick and choose donor or acceptor ligands to prepare a chromophore tailor-made to fit the needs of nearly any application.
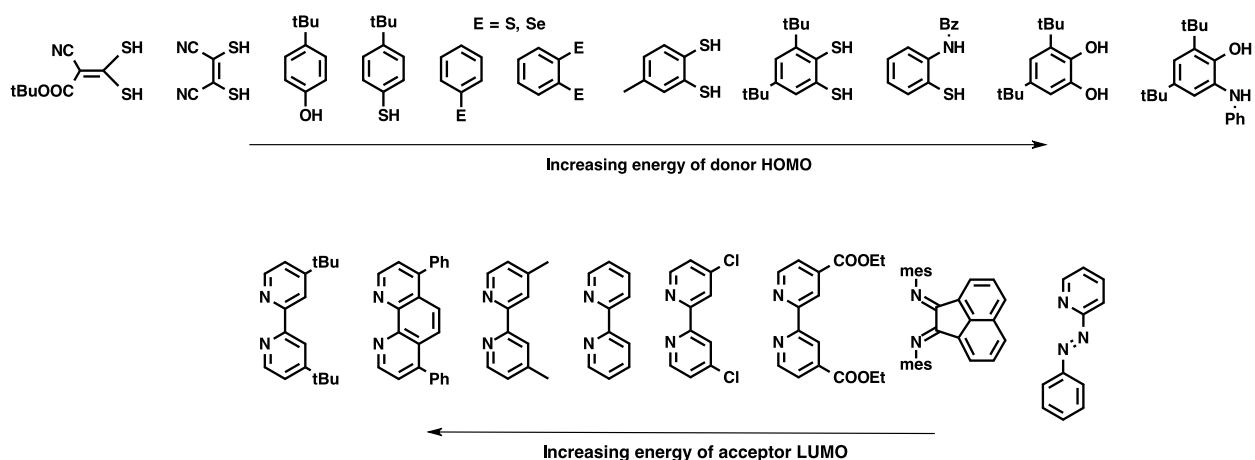
Figure 1.9. Donor and Acceptor ligand 'spectrochemical series'

1.3.4 The Importance of the Metal Ion

All complexes discussed above have general formula (donor)Pt(acceptor) because a large majority of the literature in this developing field use platinum (II) as the metal ion. Studies conducted on D-A complexes that use earth abundant metals like nickel are scant,[29,40] but there are a few reports that examine periodic trends for Group 10 D-A LL′CT dyes.[28,64,65] These studies show only small differences in the spectroscopic and electrochemical behavior of the complexes studied between the different metals. Unlike ruthenium polypyridine dyes that rely on MLCT, the ligand-based frontier orbitals of LL′CT dyes de-emphasize the metal center making it relatively benign in the charge transfer process. It can be conclude from this that it may not be necessary to favor dyes that incorporate precious metals such as platinum or palladium when designing D-A LL′CT dyes.

1.5 Summary

Donor-acceptor LL′CT dye design offers a number of advantages for solar energy conversion applications over MLCT and D-C-A dyes. The directional charge transfer inherent to the design of these dyes enables direct generation of the CSS upon photon absorption, and the localization of the electron- and hole-transfer on opposite sides of the dye molecule should allow for fast charge injection and slow back electron transfer.[66] Through straight forward chemical manipulation of the donor and acceptor ligands the energy of the LL′CT absorption (E_{CT}), the ligand localized redox processes can be controlled. Control of both of these properties means that the excited state oxidation and reduction potentials can be controlled in the same way. Donor-acceptor LL′CT dyes can be prepared using inexpensive and earth-abundant metals since the central metal ion is not a direct participant in the charge-separated state. Collectively, these features make D-A LL′CT dyes candidates for the 'ideal dye' described in Section 1.1.

1.6 References

1. Meyer, T. J. *Accounts Chem Res* **1989**, *22*, 163.
2. Alstrum-Acevedo, J. H.; Brennaman, M. K.; Meyer, T. J. *Inorg Chem* **2005**, *44*, 6802.
3. Bard, A. J.; Fox, M. A. *Accounts Chem Res* **1995**, *28*, 141.
4. Vogler, A.; Kunkely, H. *Comment Inorg Chem* **1997**, *19*, 283.
5. Kaim, W. *Coordination Chemistry Reviews* **2011**, *255*, 2503.
6. Hagfeldt, A.; Boschloo, G.; Sun, L.; Kloo, L.; Pettersson, H. *Chem Rev* **2010**, *110*, 6595.
7. Grätzel, M. *Journal of Photochemistry and Photobiology C: Photochemistry Reviews* **2003**, *4*, 145.
8. Polo, A. S.; Itokazu, M. K.; Murakami Iha, N. Y. *Coordination Chemistry Reviews* **2004**, *248*, 1343.
9. Goetzberger, A.; Hebling, C.; Schock, H.-W. *Materials Science and Engineering: R: Reports* **2003**, *40*, 1.
10. Odobel, F.; Le Pleux, L.; Pellegrin, Y.; Blart, E. *Accounts Chem Res* **2010**, *43*, 1063.
11. Robertson, N. *Angew. Chem. Int. Ed.* **2006**, 45, 2338.
12. Hardin, B. E.; Snaith, H. J.; McGehee, M. D. Nature Photon 2012, 6, 162.
13. Bozic-Weber, B.; Constable, E. C.; Housecroft, C. E. *Coordination Chemistry Reviews* **2013**, *257*, 3089.
14. Gibson, E. A.; Smeigh, A. L.; Le Pleux, L.; Fortage, J.; Boschloo, G.; Blart, E.; Pellegrin, Y.; Odobel, F.; Hagfeldt, A.; Hammarström, L. *Angew. Chem. Int. Ed.* **2009**, *48*, 4402.
15. Ji, Z.; He, M.; Huang, Z.; Ozkan, U.; Wu, Y. *J Am Chem Soc* **2013**, 11696.

16. He, J.; Lindström, H.; Hagfeldt, A.; Lindquist, S.-E. *Solar Energy Materials and Solar Cells* **2000**, *62*, 265.

17. Campagna, S.; Puntoriero, F.; Nastasi, F.; Bergamini, G.; Balzani, V. In *link.springer.com*; Topics in Current Chemistry; Springer Berlin Heidelberg: Berlin, Heidelberg, 2007; Vol. 280, pp. 117–214.

18. Juris, A.; Balzani, V.; Barigelletti, F.; Campagna, S.; Belser, P.; Zelewsky, von, A. *Coordination Chemistry Reviews* **1988**, *84*, 85.

19. Endicott, J. F.; Schlegel, H. B.; Uddin, M. J.; Seniveratne, D. S. *Coordination Chemistry Reviews* **2002**, *229*, 95.

20. Youngblood, W. J.; Lee, S.-H. A.; Kobayashi, Y.; Hernandez-Pagan, E. A.; Hoertz, P. G.; Moore, T. A.; Moore, A. L.; Gust, D.; Mallouk, T. E. J Am Chem Soc 2009, 131, 926.

21. Zhang, C.-R.; Han, L.-H.; Zhe, J.-W.; Jin, N.-Z.; Wang, D.-B.; Wang, X.; Wu, Y.-Z.; Chen, Y.-H.; Liu, Z.-J.; Chen, H.-S. *Computational and Theoretical Chemistry* **2013**, *1017*, 99.

22. Anderson, P. A.; Richard Keene, F.; Meyer, T. J.; Moss, J. A.; Strouse, G. F.; Treadway, J. A. *J. Chem. Soc., Dalton Trans.* **2002**, 3820.

23. Gust, D.; Moore, T. A.; Moore, A. L. *Accounts Chem Res* **2001**, *34*, 40.

24. Ferreira, J. A. B.; Serra, V. V.; Sánchez-Coronilla, A.; Pires, S. M. G.; Faustino, M. A. F.; Silva, A. M. S.; Neves, M. G. P. M. S.; Cavaleiro, J. A. S.; Costa, S. M. B. *Chem. Commun.* **2013**.

25. Wasielewski, M. R. *Chem Rev* **1992**, *92*, 435.

26. Falkenström, M.; Johansson, O.; Hammarström, L. *Inorganica Chimica Acta* **2007**, *360*, 741.

27. McGuire, R., Jr.; McGuire, M. C.; McMillin, D. R. *Coordination Chemistry Reviews* **2010**, *254*, 2574.

28. Mitsopoulou, C. A. 2010; Vol. 254, pp. 1448–1456.

29. Benedix, R.; Hennig, H. *Inorganica Chimica Acta* **1988**, *141*, 21.

30. Koester, V. J. *Chemical Physics Letters* **1975**, *32*, 575.

31. Benedix, R.; Hennig, H.; Kunkely, H.; Vogler, A. *Chemical Physics Letters* **1990**, *175*, 483.

32. Benedix, R.; Vogler, A. *Inorganica Chimica Acta* **1993**, *204*, 189.

33. Weyhermuller, T.; Wieghardt, K. *Dalton Trans.* **2007**.

34. Fox, G. *Inorg Chem* **1992**.

35. Archer, S.; Weinstein, J. A. *Coordination Chemistry Reviews* **2012**, *256*, 2530.

36. Wang, Y.; Hauser, B. T.; Rooney, M. M.; Burton, R. D.; Schanze, K. S. *J. Am. Chem. Soc.* **1993**, *115*, 5675.

37. Miller, T. *J Am Chem Soc* **1973**, 95, 6970.

38. Deplano, P.; Pilia, L.; Espa, D.; Mercuri, M. L.; Serpe, A. *Coordination Chemistry Reviews* **2010**, *254*, 1434.

39. Vogler, A.; Kunkely, H. *J. Am. Chem. Soc.* **1981**, *103*, 1559.

40. Paw, W.; Cummings, S.; Adnan Mansour, M.; Connick, W.; Geiger, D.; Eisenberg, R. *Coordination Chemistry Reviews* **1998**, *171*, 125.

41. Cummings, S.; Eisenberg, R. *J Am Chem Soc* **1996**, *118*, 1949.

42. Weinstein, J. A.; Tierney, M. T.; Davies, E. S.; Base, K.; Robeiro, A. A.; Grinstaff, M. W. *Inorg Chem* **2006**, *45*, 4544.

43. Adams, C. J.; Fey, N.; Parfitt, M.; Pope, S. J. A.; Weinstein, J. A. *Dalton Trans.* **2007**, 4446.

44. Parker, S. F.; Refson, K.; Bennett, R. D.; Best, J.; Mel'nikov, M. Y.; Weinstein, J. A. *Inorg Chem* **2012**, *51*, 9748.

45. Pevny, F.; Zabel, M.; Winter, R. F.; Rausch, A. F.; Yersin, H.; Tuczek, F.; Záliš, S. *Chem. Commun.* **2011**, *47*, 6302.

46. Weinstein, J. A.; Blake, A. J.; Davies, E. S.; Davis, A. L.; George, M. W.; Grills, D. C.; Lileev, I. V.; Maksimov, A. M.; Matousek, P.; Mel'nikov, M. Y.; Parker, A. W.; Platonov, V. E.; Towrie, M.; Wilson, C.; Zheligovskaya, N. N. *Inorg Chem* **2003**, *42*, 7077.

47. Weinstein, J. A.; Zheligovskaya, N. N.; Mel'nikov, M. Y.; Hartl, F. *J. Chem. Soc., Dalton Trans.* **1998**, 2459.

48. Anbalagan, V.; Srivastava, T. *Polyhedron* **2004**, *23*, 3173.

49. Shukla, S.; Kamath, S.; Srivastava, T. *J. of Photochem. & Photobio., A: Chem.* **1989**, 47, 287.

50. Deibel, N.; Schweinfurth, D.; Fiedler, J.; Záliš, S.; Sarkar, B. *Dalton Trans.* **2011**, 40, 9925.

51. Sarkar, B.; Hübner, R.; Pattacini, R.; Hartenbach, I. Dalton Trans. 2009, 4653.

52. Best, J.; Sazanovich, I. V.; Adams, H.; Bennett, R. D.; Davies, E. S.; Meijer, A. J. H. M.; Towrie, M.; Tikhomirov, S. A.; Bouganov, O. V.; Ward, M. D.; Weinstein, J. A. *Inorg Chem* **2010**, 49, 10041.

53. Dibrov, S.; Bachman, R. *Inorganica Chimica Acta* **2004**, 357, 1198.

54. Yang, J.; Kersi, D. K.; Giles, L. J.; Stein, B. W.; Feng, C.; Tichnell, C. R.; Shultz, D. A.; Kirk, M. L. *Inorg Chem* **2014**, ASAP.

55. Zuleta, J. A.; Bevilacqua, J. M.; Proserpio, D. M.; Harvey, P. D.; Eisenberg, R. Inorg Chem 1992, 31, 2396.

56. Espa, D.; Pilia, L.; Marchiò, L.; Pizzotti, M.; Robertson, N.; Tessore, F.; Mercuri, M. L.; Serpe, A.; Deplano, P. *Dalton Trans.* **2012**, 41, 12106.

57. Nomura, M.; Cauchy, T.; Fourmigué, M. *Coord. Chem. Rev.* **2010**, 254, 1406.

58. Shavaleev, N. M.; Davies, E. S.; Adams, H.; Best, J.; Weinstein, J. A. *Inorg Chem* **2008**, *47*, 1532.

59. Deibel, N.; Schweinfurth, D.; Hohloch, S.; Delor, M.; Sazanovich, I. V.; Towrie, M.; Weinstein, J. A.; Sarkar, B. *Inorg Chem* **2014**, ASAP.

60. Deibel, N.; Schweinfurth, D.; Hohloch, S.; Fiedler, J.; Sarkar, B. *Chem. Commun.* **2012**, 48, 2388.

61. Mandal, S.; Paul, N.; Banerjee, P.; Mondal, T. K.; Goswami, S. *Dalton Trans.* **2010**, 39, 2717.

62. Sun, X.; Chun, H.; Hildenbrand, K.; Bothe, E.; Weyhermüller, T.; Neese, F.; Wieghardt, K. *Inorg Chem* **2002**, *41*, 4295.

63. Dibrov, S.; Bachman, R. *Inorganica Chimica Acta* **2004**, *357*, 1198.

64. Cocker, T.; Bachman, R. *Inorg Chem* **2001**, *40*, 1550

65. Espa, D.; Pilia, L.; Makedonas, C.; Marchiò, L.; Mercuri, M. L.; Serpe, A.; Barsella, A.; Fort, A.; Mitsopoulou, C. A.; Deplano, P. *Inorg Chem* **2014**, 140109112322007.

66. Linfoot, C. L.; Richardson, P.; McCall, K. L.; Durrant, J. R.; Morandeira, A.; Robertson, N. *Solar Energy* **2011**, *85*, 1195.

Chapter 2
Square-Planar Donor-Acceptor Complexes of Nickel (II)

2.1 Introduction

Ruthenium poly-bipyridine complexes ($[Ru(bpy)_n]^{n+}$) are prototypical transition metal chromophores and have been successfully exploited in a variety of solar energy conversion applications, including dye-sensitized solar cells.[1,2] These complexes achieve a charge separated state through metal-to-ligand charge transfer (MLCT).[3-5] When a photon is absorbed by the chromophore an electron is promoted from the HOMO, which is located on the ruthenium 't_{2g}' orbitals, to the LUMO, which is localized on the bipyridine π^* orbitals. The LUMO energy can by modulated through substitutions to the bipyridine ligand backbone, but the HOMO, being localized on the metal center, is significantly less tunable. It would be desirable for a family of molecular chromophores to allow the energy of the HOMO and LUMO to be tuned independently as this could enable a tailored, application-specific approach to dye design. If both frontier molecular orbitals (MOs) were ligand localized, this independent tunability could be accomplished through modifications to ligand electronics alone.

Complexes that display ligand-to-ligand charge transfer (LL′CT), or mixed metal-ligand-to-ligand charge transfer (MMLL′CT), possess primarily ligand-centered HOMO and LUMO orbitals.[6-8] In these types of complexes the HOMO is localized on an electron-rich donor ligand and the LUMO is localized on an electron-poor acceptor ligand. Group 10 (dithiolene)M(diimine) complexes (M = Pd, Pt) are well studied LL′CT donor-acceptor (D-A) dyes.[6,9,10] These dithiolene-diimine chromophore systems have shown promise as chromophores for photo-induced charge injection.[11,12]

Donor-acceptor behavior has also been observed from (catcholate)M(diimine) complexes (M = Pd, Pt), in which the catecholate ligand replaces the dithiolene as the donor ligand.[13-17] The sulfur atoms in dithiolene ligands can be sensitive to photooxidation,[18] however catecholate

ligands have three accessible oxidation states (Scheme 2.1) and may provide increased stability towards photooxidation. D-A systems which utilize catecholate donor ligands have received significantly less attention than their dithiolene counterparts.

Scheme 2.1. Accessible oxidation states of donor and acceptor ligands.
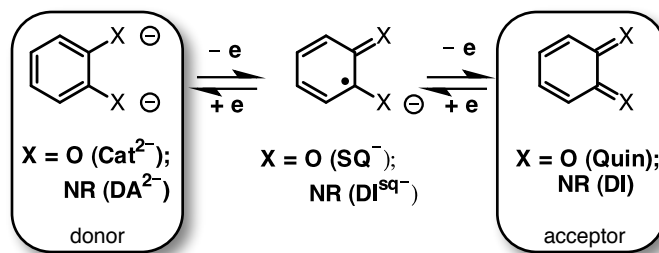
The ligand-centered frontier molecular orbitals (MOs) in D-A LL′CT dyes significantly diminishes the influence of the metal ion compared to MLCT chromophores, and the spectroscopic and electrochemical properties of D-A LL′CT complexes are largely governed by the ligands. Therefore the use of precious metals like platinum and palladium, which dominate the current literature on D-A LL′CT systems, may not be necessary and earth abundant transition metals such as nickel could be employed without significant changes in chromophore performance. Several nickel(II) dithiolene-diimine D-A LL′CT complexes have been reported, [19-21] but the lone example of a nickel(II) catecholate-diimine complex was studied exclusively in the context of olefin polymerization catalysis.[22]

This chapter details a new family of nickel(II) D-A LL′CT complexes. The modular synthetic approach employed in the synthesis of these chromophores enabled us to incorporate a variety of catecholate donor, and diimine acceptor ligands. The (donor)Ni(acceptor) complexes **1-3**, [donor = 3,5-di-*tert*-butylcatecholate (cat-tBu$_2$)$^{2-}$ and tetrachlorocatecholate (catCl$_4$)$^{2-}$; acceptor = N,N'- bis(2,4,6-trimethylphenyl)-butane–2,3-diimine (bdi), N,N'-bis(2,4,6-trimethylphenyl)acenaphthylene-1,2-diimine (adi), and N,N'-bis(2,4,6-

trimethylphenyl)phenantherene–9,10-diimine (pdi); complexes **1-3** are defined in Scheme 2.2] provide the basis for a detailed study into how alterations ligand electronics influence D-A behavior in this class of LL′CT dye. Each of the six complexes has been characterized by single crystal X–ray diffraction. The UV-vis-NIR spectra of **1-3** display intense LL′CT absorptions across the visible and near-IR region and electrochemical studies revealed tunable, ligand-centered reduction and oxidation processes. Chemical reduction and oxidation experiments with complex **2a** confirmed that the frontier MOs of **1-3** are ligand localized.

2.2 Results

2.2.1 Synthesis of (donor)Ni(acceptor) complexes

Nickel(II) donor-acceptor complexes with the general formula (catecholate)Ni(diimine) were readily accessible from the nickel(0) synthon, $Ni(COD)_2$, taking advantage of *o*-quinones' ability to act as a two electron oxidant (Scheme 2.2a). Treatment of a toluene solution containing $Ni(COD)_2$ with the desired diimine ligand resulted in the putative intermediate (diimine)Ni(COD) as evident by the development of a dark purple color in reaction mixture.[23] Subsequent addition of the appropriate quinone to the reaction mixture resulted an immediate color change in reaction mixture, and the (catecholate)Ni(diimine) products were isolated as highly colored microcrystalline solids in 66–86% yields for the complexes using 3,5 di-*tert*-butylcatecholate (**1-3a**) and 86–88% yields for the complexes with tetrachlorocatecholate (**1-3b**).

Compounds **1-3a** could also be prepared starting from a nickel(II) starting material. Treatment of a slurry of $Ni(DME)Cl_2$ with freshly prepared, $Li_2(cat\text{-}tBu_2)$, gave rise to a red-orange solution indicating the formation of the putative $(DME)Ni(cat\text{-}tBu_2)$. Subsequent addition of the diimine afforded the desired donor-acceptor complexes in good yields of 76–77% (Scheme 2.2b).

Scheme 2.2. Synthesis of nickel(II) D-A LL′CT complexes **1-3**.
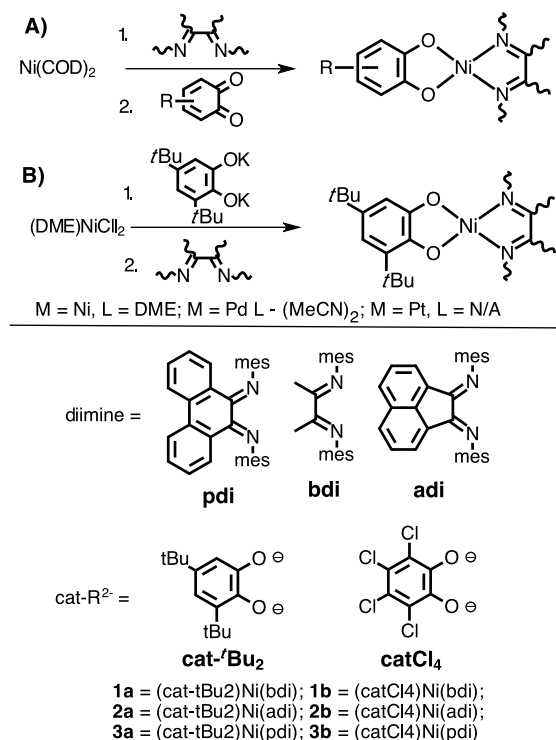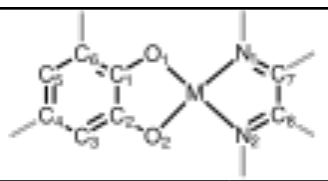
2.2.2 Structural Characterization

Solution phase ¹H and ¹³C NMR spectra obtained for complexes **1-3** are consistent with the formation of the products proposed in Scheme 2.2. The spectra displayed sharp signals in the typical diamagnetic region, suggesting a Ni(II) metal center in a square-planar coordination geometry. Despite the inherent asymmetry imposed by the 3,5-di-*tert*-butylcatecholate ligand, a pseudo-C_{2v} symmetry is observed for the diimine resonances in both the ¹H and ¹³C NMR spectra of complexes **2a** and **3a**. Complex **1a** is the lone exception, and the difference in the chemical environment resulting from the two catecholate *tert*-butyl groups was detected as splitting of the bdi backbone-methyl protons (1.56 and 1.63 ppm) and the aryl–H protons of the mesityl groups (6.93 and 6.97 ppm); this was also evident in the ¹³C NMR. The pseudo C_{2v} symmetry observed for **2-3a** is attributed to negligible influence from the catecholate on the

chemical environment of the acceptor ligands and is not believed to arise from ligands fluxionallity. Complexes **1-3b** display nominal C_{2v} symmetry in their ^{1}H and ^{13}C NMR spectra as expected.
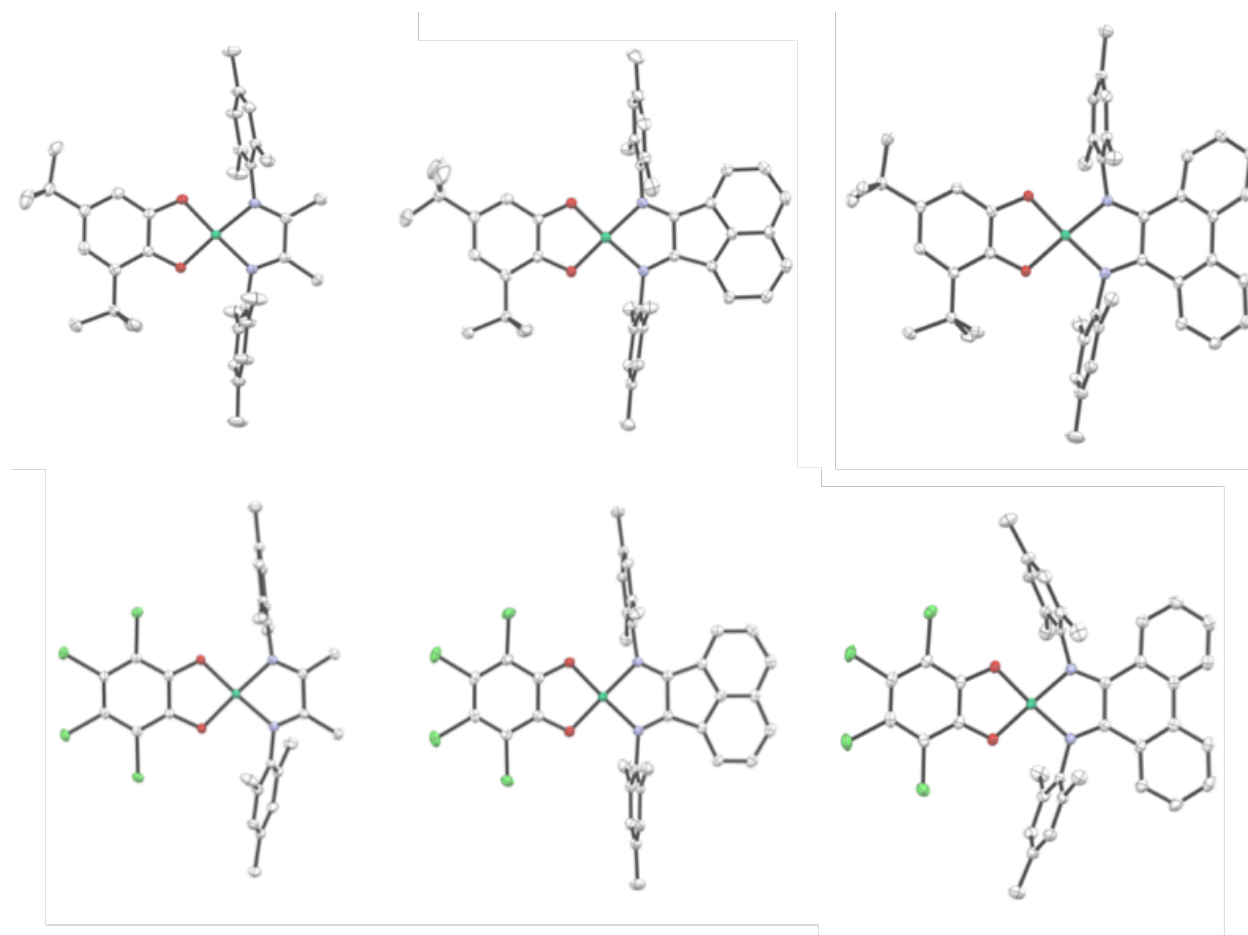
Figure 2.1. Solid state structures of **1-3**. From left to right **1a**, **2a** and **3a** (top), **1b**, **2b** and **3b** (bottom).

Table 2.1. Selected bond distances of **1-3**.

	Bond Distances / Å					
	1a	**1b**	**2a**	**2b**	**3a**	**3b**
Ni–O	1.8184(11)	1.8358(9)	1.8096(12)	1.8331(10)	1.8187(13)	1.8431(13)
Ni–O	1.8101(11)	1.8322(9)	1.8076(13)	1.8299(10)	1.8091(13)	1.8319(13)
Ni–N	1.8703(14)	1.8694(11)	1.8762(15)	1.8996(12)	1.8419(15)	1.8551(15)
Ni–N	1.8617(14)	1.8728(11)	1.8987(15)	1.9044(12)	1.8554(16)	1.8538(15)
O_1	1.350(2)	1.3313(16)	1.356(2)	1.3386(16)	1.351(2)	1.336(2)
O_2	1.3535(19)	1.3291(15)	1.362(2)	1.3309(18)	1.348(2)	1.333(2)
C_1	1.404(2)	1.4184(18)	1.402(2)	1.412(2)	1.399(3)	1.405(3)
C_2	1.405(2)	1.3875(18)	1.400(2)	1.391(2)	1.409(2)	1.388(3)
C_3	1.402(2)	1.4028(18)	1.401(2)	1.401(2)	1.398(3)	1.395(3)
C_4	1.401(3)	1.3903(19)	1.399(3)	1.386(2)	1.408(3)	1.386(3)
C_5	1.398(3)	1.4048(18)	1.395(3)	1.402(2)	1.392(3)	1.403(3)
C_1	1.390(2)	1.3889(18)	1.385(2)	1.386(2)	1.389(3)	1.387(3)
N_1	1.295(2)	1.2961(17)	1.299(2)	1.2936(19)	1.326(2)	1.314(2)
N_2	1.299(2)	1.3010(17)	1.297(2)	1.2906(18)	1.321(2)	1.310(2)
C_7	1.474(2)	1.4871(18)	1.472(2)	1.4803(19)	1.457(2)	1.485(2)

The presence of two redox-active ligands in the nickel complexes **1-3** leads to an inherent ambiguity when attempting to assign the experimental oxidation states of the metal and the ligands. Single-crystal X-ray diffraction studies conducted on each member of the series confirmed the desired donor-acceptor arrangement in **1-3**. Solid state structures, obtained for each member of the series are displayed in Figure 2.1, and relevant bond distances are provided in Table 2.1. Each donor-acceptor complex displayed a square-planar coordination geometry around the nickel center. Intraligand bond distances can be used to differentiate between the possible oxidation states in redox-active ligands. For example, in catecholate ligands the C−O

bond lengths change significantly between the quinone (1.23. Å), semiquinonate (1.29 Å) and catecholate (1.35 Å) oxidation states.[24-27] Complexes **1-3a** display C–O bond distances of 1.36-1.35 Å, consistent with the catecholate oxidation state, and no evidence of double bond localization within the C_6 ring, common of the semiquinonate and quinone oxidation states, could be detected. Complexes **1-3b** display slightly shorter C–O bonds (1.33–1.34 Å) which is typical for the fully reduced tetrachlorocatecholate ligand, also the C–C bonds in the C_6 ring of **1-3b** show no double bond localization.[22] The C–N bond lengths of complexes **1-3** fall within the range 1.29–1.32 Å and are in good agreement with the accepted values for α-diimine ligands (ca. 1.30 Å).[28-30] The C–C bonds distances in the α-diimine backbones are well within the expected values for single bonds between sp^2-hybridized carbon atoms (1.46–1.48 Å). The slightly elongated C–N bond distances found for **3a** (1.32 Å) are still shorter than would be expected for a one or two electron reduced ligand (1.34 and 1.43 Å respectively). A slight contraction of the C–C bond of the pdi backbone (1.46 Å) is also observed in **3a**, but because this bond is part of the aromatic system of the phenantherene backbone, it is difficult to use this bond as metric for oxidation state assignment. Overall, the crystallographic data are consistent with dianionic catecholate donors and neutral diimine acceptors bound to nickel(II) metal centers.

2.2.3 Electronic Properties

Nickel(II) donor-acceptor complexes **1-3** are highly colored in the solid-state and in solution. The UV-vis-NIR spectra of **1-3**, shown in Figure 2.2, are dominated by strong, low-energy absorptions with λ_{max} ranging from 600-1200 nm. The energy and intensity of these low-energy transitions are dependent on both the donor and acceptor ligand identity. The acceptor ligands influence is demonstrated through a comparison of the absorption spectra complexes **1-3a**, which feature the same (cat-tBu$_2$)$^{2-}$ donor ligand (Figure 2.2a). The intense low-energy

feature of complex **1a**, (cat-tBu$_2$)Ni(bdi), occurs at 816 nm (1.52 eV, ε = 6510M^{-1}cm^{-1}). When the bdi acceptor ligand of **1a** was exchanged for acceptors with more extended π systems the low-energy feature red-shifted significantly and absorption maxima for (cat-tBu$_2$)Ni(adi) occurs at 1026 nm (1.21 eV, ε = 10430 M^{-1}cm^{-1}) and is further red-shifted for (cat-tBu$_2$)Ni(pdi) to 1186 nm (1.04 eV, ε = 16500 M^{-1}cm^{-1}). The acceptor influence on the energy of the primary absorption is bdi (**1a)** > adi (**2a)** > pdi (**3a**). Complexes **1-3b,** which use the tetrachlorocatecholate donor ligand, behaved identically to **1-3a** with regards to substitution of the acceptor ligand, but the low-energy absorptions were significantly blue-shifted from their 3,5-di-*tert*-butylcatecholate analogues. The ligand dependence of the low-energy absorptions of **1-3** indicate the D-A LL′CT character of these transitions.
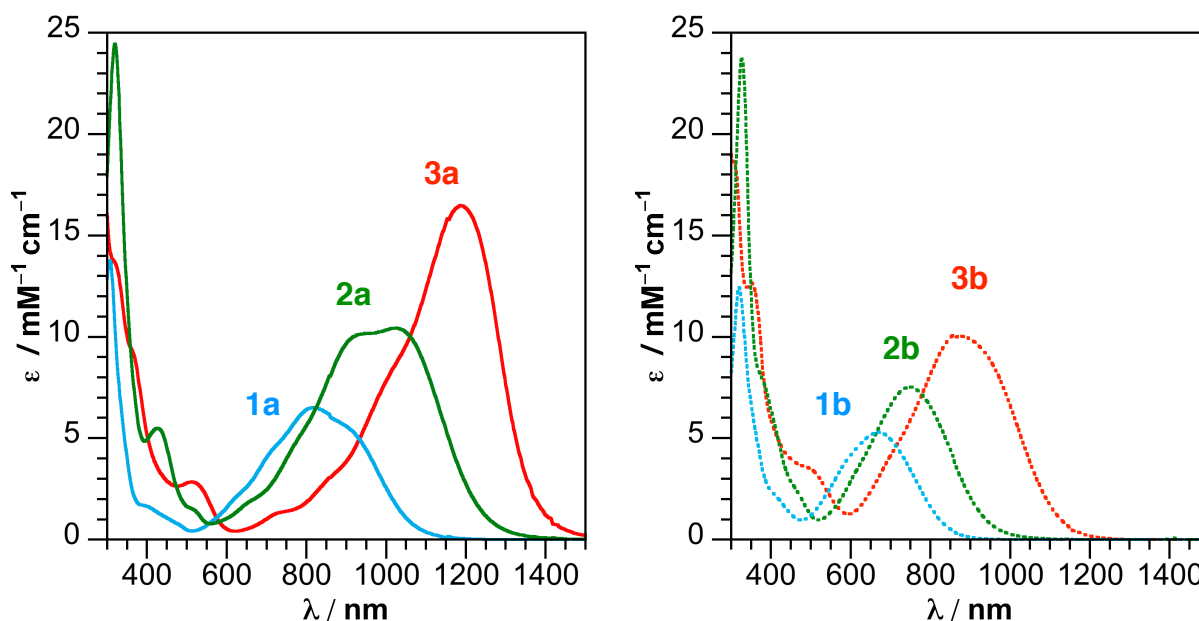
Figure 2.2. UV-vis-NIR absorption spectra of **1-3a** (top) and **1-3b** (bottom) in DCM at 298 K.
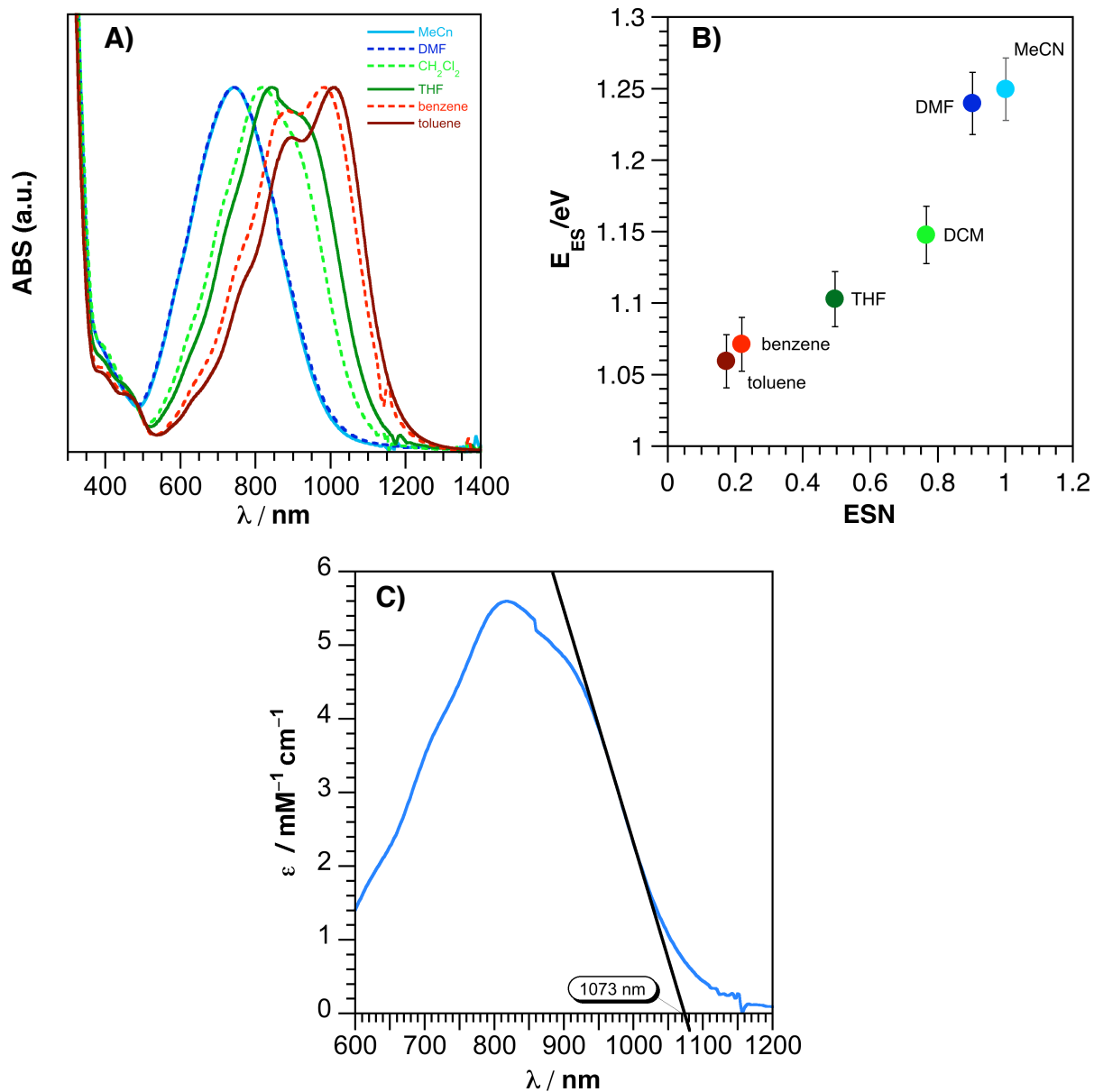
Figure 2.3. (**A**) Normalized absorption spectra of (cat-tBu$_2$)Ni(bdi) in toluene , benzene, THF, DCM, DMF, and acetonitrile. (**B**)Plot of E_{CT} vs. ESN[6] with fit. (**C**) Tangent used to estimate E_{CT}.

The LL′CT absorptions of complexes **1-3** exhibit negative solvatochromatic behavior, where increasing solvent polarity causes a blue-shift of the absorption. This solvent dependence is shown for complex **1a** in Figure 2.3a represents the behavior displayed by the entire series. UV-vis spectra of **1-3** were recorded in MeCN, DMF, DCM, THF, toluene and benzene (spectra for complexes **1-3b** could not be collected in DMF due to instability in this solvent). As depicted

in Figure 2.3b for complex **1a**, the solvatochromic shift (SS) of each complex is determined by the slope of the line generated by plotting the estimated LL′CT excited state energy (E_{CT}) vs Einsenberg and Cummings' empirical solvent number (ESN).[6] The excited state energies used for this analyses were estimated from the low-energy onset of the absorption curve, as shown in Figure 2.3c. Table **2.2** contains λ_{max}, E_{es}, and SS values for complexes **1-3**. The magnitude of the solvatochromic shift observed for **1-3** correlates to energy of the charge transfer absorption. The donor-acceptor complex with the highest energy absorptions display greater SSs. Complexes using the donor $(catCl_4)^{2-}$ ligand generally displayed greater SS values than the corresponding complexes with $(cat\text{-}tBu_2)^{2-}$. The lone exception, $(catCl_4)Ni(bdi)$, displayed an SS (0.19) smaller than $(cat\text{-}tBu_2)Ni(bdi)$ and both **2b** and **3b**. This molecule is the most electron poor member of the series and in polar solvents, solvent molecules interacting with the nickel(II) metal center could cause significant changes in the absorption spectra.

Table 2.2. λ_{max}, E_{CT}, and SS of **1-3**.

	Abs. λ_{max}	estimated E_{es}	solvatochromic shift
1a	818	9320 (1.16)	0.23
1b	670	14900 (1.85)	0.19
2a	1024	8050 (1.02)	0.13
2b	748	10500 (1.31)	0.28
3a	1186	7350 (0.911)	0.02
3b	858	8930 (1.11)	0.19

Electrochemistry provides an equilibrium measurement of HOMO and LUMO energies — which correspond to the redox potentials of the first oxidation ($E^{+/0}$) and first reduction ($E^{0/-}$), respectively — and can give additional insight into the effect of donor and acceptor ligands on

the frontier orbitals in the nickel complexes **1-3**. Cyclic and differential pulse voltammetry experiments were conducted for complexes **1-3**. The cyclic voltammetry data, obtained for each complex dissolved in a DCM solution containing 0.1 M [Bu$_4$N][PF$_6$] and referenced vs. [Cp$_2$Fe]$^{+/0}$, are shown in Figure 2.4. Reduction potentials and ΔE values determined from the differential pulse voltammetry experiments are listed in Table 2.3. Reversible, one-electron reductions were observed in the cathodic portion of the voltammograms, complexes **1-3**. Two reversible reductions were observed in the solvent window with complexes **3a** and **3b**. For the other members of the series, only the first reductive process could be observed with the presumed second reduction occurring outside of the solvent window. The acceptor ligands influence on the potential of E$^{0/-}$ is demonstrated by complexes **1-3a**. The potential of the first reduction event is most negative was for complex **1a**, and is shifted to more positive potentials for **2a** and **3a**, respectively. Substitution of (cat-tBu$_2$)$^{2-}$ for the more electron deficient (catCl$_4$)$^{2-}$ resulted in only a slight positive shift of the reduction potentials for **1-3b**. The anodic portion of the voltammograms show two one-electron oxidation events for all members of the series. The first oxidative processes are fully reversible and the second oxidations are partially reversible or irreversible. The identity of the acceptor ligand had a negligible effect on the potentials observed for the oxidative events though the presence of the electron withdrawing chloride groups of (catCl$_4$)$^{2-}$ caused in a large positive shift in E$^{+/0}$ ($\sim$ 500 mV) of **1-3b** from **1-3a**. The difference in potential between E$^{+/0}$ and E$^{0/-}$, ΔE, provides an estimate of the HOMO-LUMO gap (ΔHL). The trends observed for ΔE mirror those observed spectroscopically, where with respect to the acceptor, ΔE bdi > adi > pdi, and, with respect to the donor, ΔE (catCl$_4$) > (cat-tBu$_2$).
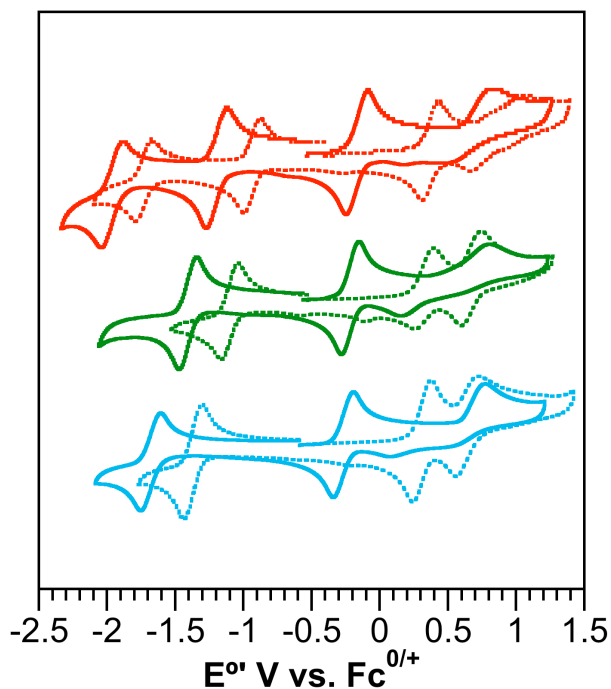
Figure 2.4. Cyclic voltammograms of complexes **1-3a** (solid) and **1-3b** (dashed) as 1 mM solution of analyte in CH$_2$Cl$_2$ with 0.1 M [n-Bu$_4$N][PF$_6$] supporting electrolyte. **1** (blue), **2** (green) and **3** (red).

Table 2.3. Reduction potentials (V vs [Cp2Fe]+/0) for complexes **1-3**.

	$E°'$				
	E	E	E$^{0/1-}$	E	ΔE
1a	0.65	–0.26	–1.68	--	1.41
1b	0.62	0.31	–1.35	--	1.66
2a	0.69	–0.22	–1.41	--	1.19
2b	0.61	0.27	–1.14	--	1.42
3a	0.66	–0.17	–1.22	–1.97	1.05
3b	0.7	0.36	–0.94	–1.74	1.31

2.2.4 Chemical Redox Reactions with (cat-tBu2)Ni(adi).

Chemical oxidation and reduction experiments were conducted to better understand the redox processes observed for complexes **1-3**. The reversible oxidative and reductive processes displayed in the electrochemistry of the nickel(II) D-A complexes indicated that chemically oxidized and reduced species could be isolated and characterized. Complex **2a**, (cat-*t*Bu₂)Ni(adi), was chosen as the ideal candidate for these experiments. The one-electron oxidized cationic species [(sq-*t*Bu₂)Ni(adi)]⁺[OTf]⁻, **[2a]⁺** (sq-*t*Bu₂ = 3,5-di-*tert*-butyl-o-semiquinonate), was prepared by treating an acetonitrile solution containing **2a** with solid AgOTf at room temperature. The paramagnetic product was isolated as a green-brown solid in 98% yield. The one-electron reduction was achieved by treating a MeCN solution of **2a** with decamethylcobaltocene (Cp*₂Co) at − 35 ºC. The product [Cp*₂Co]⁺[(cat-*t*Bu₂)Ni(adiˢᑫ)]⁻, **[2a]⁻**, (adiˢᑫ = N,N'-bis(2,4,6-trimethylphenyl)acenaphthylene−1,2-diiminosemiquinonate) was isolated in near quantitative yield as an amorphous green solid.

Complex **[2a]⁺** was characterized by EPR spectroscopy in dichloromethane as an S = 1/2 ion at 298 K. No signal was observed at 77 K. The X-band EPR spectrum of **[2a]⁺** in CH₂Cl₂ (Figure 5a) gave an isotropic signal at g = 2.00 with a two-line hyperfine splitting pattern (a_H = 4 G). The EPR spectrum of **[2a]⁺** was fit using these parameters. This signal is nearly identical to that observed by Ohtsu et. al. for their nickel(II) 3,5-di-*tert*-butylsemiqunionate complexes.[31,32] The X-band EPR spectrum obtained at 77 K from the S = 1/2 **[2a]⁻** in a 1:1 MeCN/toluene solution is shown in Figure 5b. The axial signal gave $g_∥$ = 2.03 and $g_⊥$ = 1.99 and showed five line hyperfine splitting (a_N = 24 G) consistent with interaction of the radical with the nitrogen atoms of the adi ligand; these parameters were use to fit the spectrum. While the high dielectric

constant of MeCN inhibited collection of a spectrum at 298 K, an isotropic signal with g = 2.00

was observed for [**2a**]⁻ in DCM solution at room temperature.
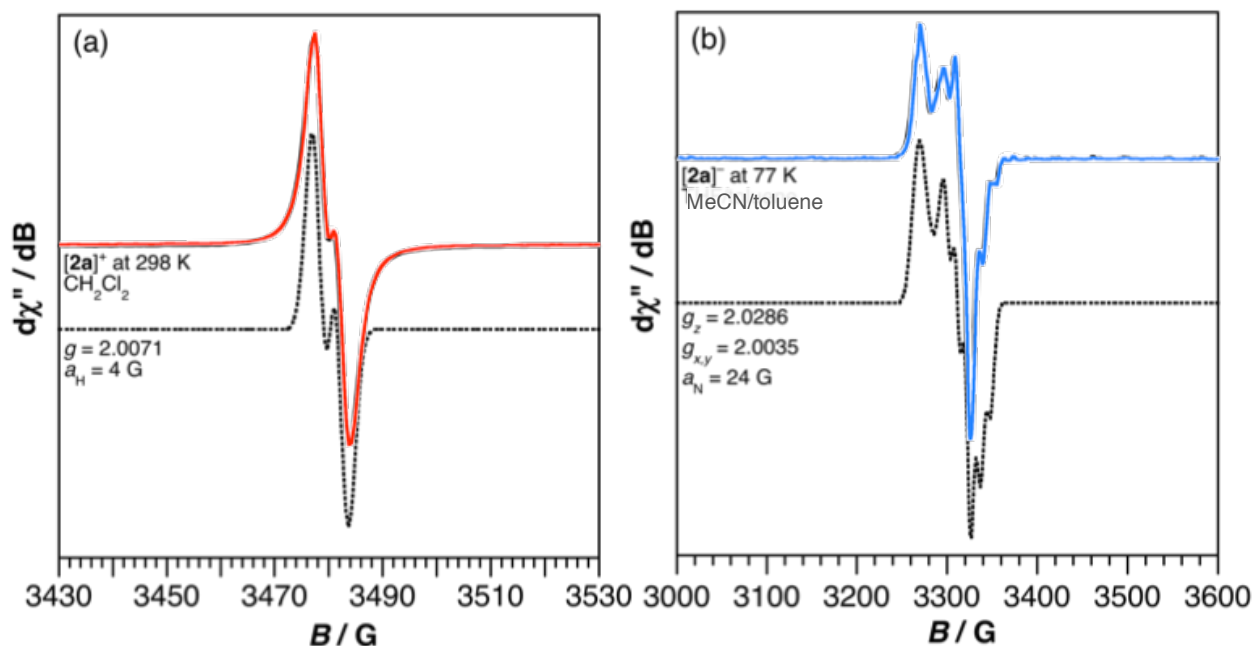
Figure 2.5. X-band EPR (solid) and simulation (dotted) of (a) [**2a**][OTf] in DCM at 298 K and (b) [Cp*₂Co][**2a**] in MeCN/toluene (1:1) at 77 K.

The absorption spectra of the cation [**2a**]⁺ and the anion [**2a**]⁻ were markedly different

from the neutral complex. The UV-vis-NIR absorption spectra of the **2a**, [**2a**]⁺, [**2a**]⁻ taken in

MeCN at 298 K are shown in Figure 6. Upon oxidation to [**2a**]+ the low energy absorption of **2a**

was blue-shifted to 786 nm and almost completely suppressed with an extinction coefficient of

655 M⁻¹ cm⁻¹. Reduction of **2a** to [**2a**]⁻ also resulted in a blue-shift of the low-energy band to 774

nm, though the decrease in the intensity of the absorption was less dramatic (ε = 5053 M⁻¹cm⁻¹).
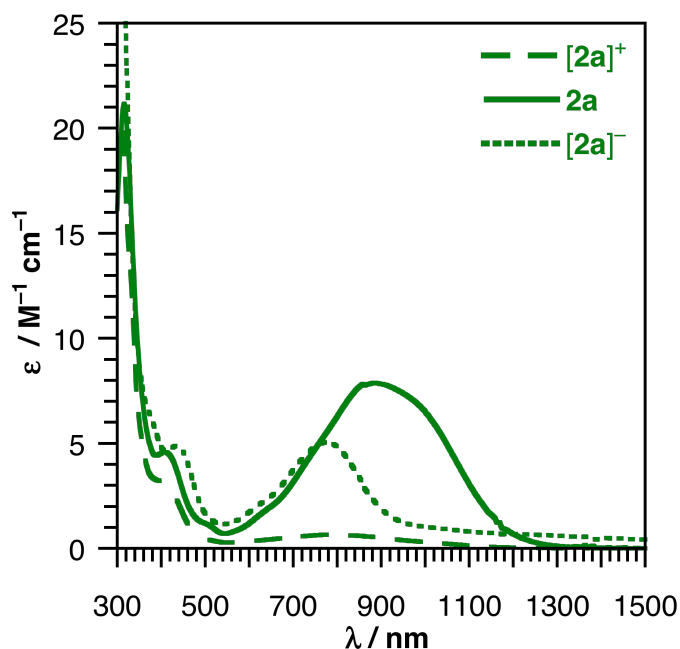
Figure 2.6. UV-vis-NIR absorption spectra of [(cat-tBu$_2$)Ni(adi)]$^+$, **[2a]$^+$**, (cat-tBu$_2$)Ni(adi), **2a**, and [(cat-tBu$_2$)Ni(adi)]$^-$, **[2a]$^-$** in MeCN solution at 298 K.

2.3 Discussion

2.3.1 Influence of the Ligands.

A series of new nickel(II) donor-acceptor complexes with redox-active catecholate donor and diimine acceptor ligands are described in this chapter. Flexible synthetic methods were developed to install the fully reduced catecholates and fully oxidized diimines using both nickel(0) or nickel(II) starting materials (Ni(COD)$_2$ or (DME)NiCl$_2$, respectively). This modular approach to dye synthesis enabled the installation of two different catecholate donor ligands [(cat-tBu$_2$)$^{2-}$ and (catCl$_4$)$^{2-}$] paired with three diimine acceptor ligands (bdi, adi, and pdi) to obtain the nickel(II) donor-acceptor chromophores **1-3** in good yields. Solid state structures obtained by single-crystal X-ray diffraction were used to determine the experimental oxidation states of the complexes, and in all cases the desired (catecholate)Ni(diimine) formation was observed. The ability to easily incorporate a variety of donor and acceptor ligands with different

electronic properties allowed us to investigate how the changes effect the spectroscopic and electrochemical properties of complexes **1-3**. Through the systematic manipulation of the ligand environment we were able to gain a more complete understanding of the electronic structure of these D-A complexes.

The influence of the acceptor is illustrated through examination of complexes **1-3a** which share the same donor ligand, (cat-tBu$_2$)$^{2-}$. The UV-vis-NIR absorption spectra of these complexes are dominated by broad, intense, LL′CT in the visible and near-IR regions of the spectrum (ca. 600-1200 nm). The energy of the absorptions were highly dependent on the identity of the acceptor ligands and a red-shift of the low-energy absorption was observed where **1a** > **2a** > **3a**, emphasizing their involvement in the charge transfer. This trend correlates to lowering diimine LUMO energies from bdi to adi to pdi as π-delocalization increases in the ligand backbone.

The effect of acceptors identity on the frontier molecular orbitals of **1-3a** was also measured electrochemically. Cyclic voltammograms of **1-3a** show reversible, diimine-centered reductive processes, in addition to two catecholate centered oxidative processes. The potential of the first reduction is greatly dependent on the identity of the acceptor ligands, which was most negative for **1a** and shifted to more positive potentials with **2a** and **3a**, respectively. Substitution of the acceptor ligands could be without significantly altering the potential of E$^{0/+}$. This shows that the HOMOs of these complexes are isolated from any changes that occur to the LUMO, and while the LUMO energy levels were altered through substitution of the diimine ligand, the donor-based HOMO was held constant. The trend in ΔE for the identity of the diimine acceptors mirrors the trend observed for the LL′CT absorption. This provides an ordering of the HOMO-LUMO gap (ΔHL) to be established based on the spectroscopic and electrochemical data where ΔHL **1a** > **2a** > **3a**. Changes in acceptor ligand identity of the donor-acceptor complexes **1-3a**

demonstrate that the energy of the acceptor-based LUMO, and therefore ΔHL, is highly tunable through relatively simple modifications to the acceptor ligand electronics.

The electronics of the catecholate donor ligand also play an important role in determining the properties of the (acceptor)Ni(donor) complexes due to the localization of the HOMO on the donor ligand,. The extent of this effect was studied by preparing complexes **1-3b** as analogues of **1-3a**, wherein tetrachlorocatecholate $[(catCl_4)^{2-}]$ was used as the donor in place of $[(cat\text{-}t\text{Bu2})]^{2-}$. The introduction of electron withdrawing chlorine substituents resulted in a significant blue shift of the LL′CT bands for **1-3b** compared to **1-3a**. Electrochemically, the substitution caused a positive shift of ca. 500 mV in the potential of $E^{+/0}$ for complexes **1-3b** vs. **1-3a** and minimal changes in the cathodic portion of the voltammograms again demonstrating our ability to alter the frontier MOs of these complexes independently of one another. This increase in the potential of $E^{+/0}$ corresponded to increased values of ΔE for **1-3b** over **1-3a** by approximately 250 mV. Introduction of electron withdrawing substituents to the donor ligand resulted in a lowering of the HOMO energy and widened ΔHL.
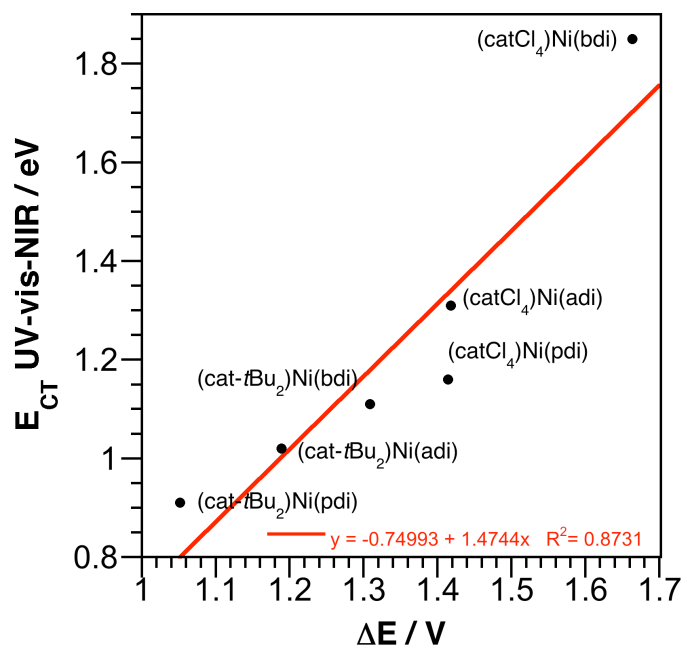
Figure 2.7. Plot of the charge-transfer absorption energy (eV) vs the electrochemical HOMO-LUMO gap (V) for **1-3**.

Complexes **1-3** display absorption profiles that absorb across the entire visible region into the near-IR. The cyclic voltammetry data of **1-3** highlight the fact that this system allows for independent control of the energy of the catecholate centered HOMO and the diimine centered LUMO. A plot of ΔE against the E_{CT} for complexes **1-3** is shown in Figure 4.7 which depicts a strong correlation between these two experimental measurements of ΔHL. This further emphasizes the ligand-centered nature of the frontier molecular orbitals, and consequently the spectroscopic and electrochemical properties, of these complexes and that these properties can be controlled through alterations of either the donor or acceptor ligands alone.

2.3.4 Insights into the Electronic Structure of the (catecholate)Ni(diimine) Complexes

Further insight into the electronic structure of these D-A complexes was obtained through chemical redox reactions with complex **2a**, (cat-tBu$_2$)Ni(adi). The cationic [**2a**]$^+$ as the triflate

salt displayed EPR spectra consistent with the oxidation having taken place on the catecholate. While the EPR spectra of the anion salt $[Cp^*_2Co]^+[2a]^-$ at 77 K was characteristic of a diimine centered radical, the axial signal suggests at least some involvement of the metal in the SOMO. These experiments confirm the ligand-centered nature of the HOMO and LUMO in these complexes. The similar behavior observed for each member of the series allow us to extend this reasoning to the rest of this family of D-A complexes.

Negative solvatochromic behavior of the low-energy absorption feature was observed for all nickel(II) donor acceptor complexes and further reinforces the LL′CT character of the low-energy absorptions of **1-3**. The magnitude of the blue-shift induced through increasing solvent polarity, or the solvatochromic shift, is dependent on the ground state (GS) dipole moment of a particular molecule. The greater the GS dipole moment of a molecule the greater the observed SS should be. Due to presence of the electron-rich catecholate donor ligand and electron-poor acceptor there is a dipole inherent to the ground state of D-A molecules. In an 'ideal' donor-acceptor complex, the concentration of electron density on the donor ligand would give rise to a large ground state dipole. In our (catecholate)Ni(diimine) complexes this can be correlated to the degree to which electron density of the HOMO is localized on the catecholate ligand. Because of this, SS provides a metric with which to estimate charge separation in the ground-state of complexes **1-3** and to understand how ligand substitution affects donor-acceptor character. Increases in the HOMO-LUMO gap of the donor-acceptor complexes results in less delocalization of electron density across the molecule in the GS, resulting in a greater solvatochromic shift. As Δ_{HL} is decreased through alterations of ligand electronics, more mixing of the acceptor-character into the HOMO and donor character in the LUMO occurs decreasing the donor-acceptor character.

2.4 Summary

The flexible synthetic method used to prepare the (catecholate)Ni(diimine) complexes **1-3** provided access to a variety of nickel(II) donor-acceptor LL′CT dyes with a broad range of electronic properties. This enabled a detailed investigation into how changes to the electronics of either ligand influence the electronic structure of these molecules. Because the dye HOMOs are localized on the catecholate ligands and the dye LUMOs are localized on the diimine ligands, the optical and electrochemical properties of the dyes can be tuned independently.Complexes **1-4** display absorption profiles that absorb across the entire visible region into the near-IR as well as electrochemistry in which oxidative and reductive processes are tunable independent of the other. Through careful selection of donor and acceptor ligands, our (catecholate)Ni(diimine) D-A platform could be employed as chromophores for a wide variety of applications due to their inherently tunable thermodynamic parameters. Unlike ruthenium poly-pyridine dyes that rely on MLCT, the ligand-based frontier orbitals of our dyes de-emphasize the role of the metal center making it relatively benign in the charge transfer process. It can be conclude from these results that it is not necessary to favor dyes that incorporate, precious metals such as platinum or palladium when designing chromophores based on this donor-acceptor platform.

2.5 Experimental

General Considerations. All compounds and reactions reported below are air- and moisture-sensitive so all manipulations were carried out using standard vacuum-line, Schlenk-line and glovebox techniques. Solvents were sparged with argon before being deoxygenated and dried by passage through Q5 and activated alumina columns, respectively. To test for effective oxygen and water removal, aliquots of each solvent were treated with a few drops of a purple solution of sodium benzophenone ketyl radical in THF. The reagents 3,5-di-*tert*-butyl-1,2-quinone (Aldrich), tetrachloro-1,2-quinone (Acros), and Ni(cod)$_2$ (Strem) were reagent grade or better and used as

received. The diimine ligands *N,N′*-bis(2,4,6-trimethylphenyl)-2,3-butanediimine (bdi),[33] *N,N′*-bis(2,4,6-trimethylphenyl)acenaphthenediimine (adi),[34] and *N,N′*-bis(2,4,6-trimethylphenyl)-9,10-phenanthrenediimine (pdi)[35] were prepared according to published procedures.

Spectroscopic Measurements. NMR spectra were collected at 298 K on a Bruker Avance 500 MHz spectrometer in dry, degassed $CDCl_3$. ^{1}H NMR spectra were referenced to tetramethylsilane (TMS) using the residual proteo impurities of the solvent (7.26 ppm); ^{13}C NMR spectra were referenced to TMS using the natural abundance ^{13}C impurities of the solvent (77.16 ppm). All chemical shifts are reported using the standard δ notation in parts per million; positive chemical shifts are to a higher frequency from the given reference. Electronic absorption spectra were recorded with a Perkin-Elmer Lambda 900 UV-vis-NIR spectrophotometer in CH_2Cl_2 using 1-cm path-length cells at ambient temperature (20-24 °C).

Electrochemical Methods. Electrochemical experiments were performed on a Gamry Series G300 potentiostat/galvanostat/ZRA (Gamry Instruments, Warminster, PA) using a 3.0 mm glassy carbon working electrode, a platinum wire auxiliary electrode, and a silver wire reference electrode. Reversibility was judged based on the ratio of the anodic (i_{pa}) to the cathodic (i_{pc}) current for a given process. Electrochemical experiments were performed at ambient temperature (20-24 °C), either in a nitrogen-filled glovebox or under an atmosphere of argon. Sample concentrations were 1.0 mM in analyte in THF solution containing 100 mM [NBu4][PF6] as the supporting electrolyte. All potentials are referenced to $[Cp_2Fe]^{+/0}$ using ferrocene or decamethylferrocene (–0.49 V vs $[Cp_2Fe]^{+/0}$) as an internal standard added at the end of a sample run. The typical potential window for our configuration was +1.0 V for the oxidation limit and –3.4 V for the reduction limit (vs $[Cp_2Fe]^{+/0}$). Ferrocene and decamethylferrocene (Acros) were purified by sublimation under reduced pressure and tetrabutylammonium hexafluorophosphate (Acros) was recrystallized from ethanol three times and dried under vacuum.

General (catecholate)Ni(diimine) Synthesis, Method A. A solution of Ni(cod)$_2$ in 10 mL of benzene or toluene was treated with the appropriate diimine ligand as a solid. The solution was stirred at ambient temperature for 12 h during which time the solution color changed from yellow to red or purple. Solid quinone was then added to the solution resulting in the formation of a dark suspension/solution over the course of 3 h. For complexes incorporating the tetrachlorocatecholate ligand, the reaction mixture was filtered through a sintered glass frit to obtain the product as a darkly colored solid. In the case of complexes incorporating the 3,5-di-*tert*-butylcatecholate ligand, the solution volume was reduced in vacuo, diluted with pentane and stored at –35 °C. The resulting precipitate was collected by filtration, washed with aliquots of cold pentane and dried under reduced pressure to obtain the desired product as a darkly colored solid.

General (catecholate)Ni(diimine) Synthesis, Method B. A frozen solution containing 3,5-di-*tert*-butylcatechol in THF was thawed and immediately treated with two equivalents of nBuLi (2.49 M in hexanes). The mixture was stirred and allowed to warm to room temperature before being combined with a suspension of (dme)NiCl$_2$ in 10 mL of THF. The reaction was stirred for 12 h at ambient temperature to afford a red-orange solution which was treated with a solid portion of the appropriate diimine ligand. The reaction mixture was stirred for an additional 12 h before the solvent was removed under reduced pressure. The solid residue was co-evaporated with Et$_2$O and pentane and then extracted with toluene and filtered to remove LiCl. The volume of the filtrate was reduced, diluted with pentane and cooled to –35 °C. A first crop of the product

was collected from the cold solution by filtration. A second crop of product was obtained by reprocessing the filtrate.

Synthesis of (cat-*t*Bu₂)Ni(bdi) (1a). Complex **1a** was prepared according to Method A in using N,N'-bis(2,4,6-trimethylphenyl)-2,3-butanediimine (160 mg, 0.500 mmol, 1.0 equiv), Ni(cod)₂ (138 mg, 0.500 mmol, 1.0 equiv), and 3,5-di-*tert*-butyl-*o*-benzoquinone (110 mg, 0.5000, 1.0 equiv). The product was isolated as a dark green solid in 77% yield (231 mg).

The preparation of **1a** by Method B proceeded using 222 mg of 3,5-di-*tert*-butylcatechol (1.00 mmol, 1 .0 equiv), 220 mg of (dme)NiCl₂ (1.00 mmol, 1.0 equiv), and 320 mg of N,N'-bis(2,4,6-trimethylphenyl)-2,3-butanediimine (1.00 mmol, 1.0 equiv). The product was isolated as a dark green solid in 76% yield (454 mg). X-ray quality crystals were grown by layering a solution of **1** in toluene with pentane.

Anal. Calcd. (Found) for $C_{36}H_{48}N_2O_2Ni$: C, 72.13 (71.93); H, 8.07 (8.13); N, 4.67 (4.37). ¹H NMR (CDCl₃, 500 MHz) δ/ppm: 0.90 (s, 9H, tBu), 1.12 (s, 9H, tBu), 1.56 (s, 3H, N=CMe), 1.63 (s, 3H, N=CMe), 2.32 (s, 12H, *o*-Me), 2.36 (s, 6H, *p*-Me), 6.24 (s, 2H, cat-*H*), 6.94 (s, 2H, aryl-*H*), 6.96 (s, 2H, aryl-*H*). ¹³C NMR (CDCl₃, 125.8 MHz) δ/ppm: 167.0 (*C*=N), 166.5 (*C*=N), 161.8 (*C*–O), 157.5 (*C*–O), 142.3 (aryl-*C*), 137.7 (aryl–*C*), 136.5 (aryl–*C*), 136.4 (aryl-*C*), 134.5 (aryl–*C*), 130.2 ((aryl–*C*), 129.8 (aryl–*C*), 128.8 (aryl–*C*), 110.6 (aryl–*C*), 110.1 (aryl–*C*), 34.4 (*C*(CH₃)₃) 34.2 (*C*(CH₃)₃), 32.4 (*C*(CH₃)₃), 29.5 (*C*(CH₃)₃), 21.6 (*p*–CH₃), 21.4 (*p*–CH₃), 18.8 (*o*–CH₃), 18.7 (*o*–CH₃), 17.9 (N=C–CH₃). UV-vis-NIR (CH₂Cl₂) λ_{max}/nm (ε/M⁻¹ cm⁻¹): 308 (13,700), 816 (6510).

Synthesis of (catCl₄)Ni(bdi) (1b). Complex **1b** was prepared according to Method A using N,N'-bis(2,4,6-trimethylphenyl)-2,3-butanediimine (117 mg, 0.364 mmol, 1.0 equiv), Ni(cod)₂ (100 mg, 0.364 mmol, 1.0 equiv), and tetrachloro-1,2-quinone (89 mg, 0.364 mmol, 1.0 equiv). The product was isolated as a dark blue solid in 88% yield (199 mg). X-ray quality crystals were grown by slow evaporation of a CH₂Cl₂ solution of **1**.

Anal. Calcd. (Found) for $C_{28}H_{28}N_2O_2Cl_4Ni$: C, 53.80 (53.93); H, 4.42 (4.37); N, 4.48 (4.07). ¹H NMR (CDCl₃, 500 MHz) δ/ppm: 1.84 (s, 6H, N=CMe), 2.44 (s, 12H, *o*-Me), 2.34 (s, 6H, *p*-Me), 7.00 (s, 4H, aryl-*H*). ¹³C NMR (CDCl₃, 125.8 MHz) δ/ppm: 171.0 (*C*=N), 157.6 (*C*–O), 140.5 (aryl–*C*), 137.9 (aryl–*C*), 130.1 (aryl–*C*), 129.3 (aryl–*C*), 117.1 (aryl–*C*), 115.5 (aryl–*C*), 21.5 (*p*–CH₃), 18.9 (*o*–CH₃), 18.4 (*CH₃*). UV-vis-NIR (CH₂Cl₂) λ_{max}/nm (ε/M⁻¹ cm⁻¹): 320 (12,400), 670 (5280).

Synthesis of (cat-*t*Bu₂)Ni(adi) (2a). Complex **2a** was prepared according to Method A using N,N'-bis(2,4,6-trimethylphenyl)acenaphthenediimine (212 mg, 0.500 mmol, 1.0 equiv), Ni(cod)₂ (138 mg, 0.500 mmol, 1.0 equiv), and 3,5-di-*tert*-butyl-*o*-benzoquinone (110 mg, 0.5000, 1.0 equiv). The product was isolated as a yellow-green solid in 86% yield (299 mg).

The preparation of **2a** by Method B proceeded using 506 mg of 3,5-di-*tert*-butylcatechol (2.28 mmol, 1.0 equiv), 500 mg of (dme)NiCl₂ (2.28 mmol, 1.0 equiv), and 946 mg of N,N'-bis(2,4,6-trimethylphenyl)acenaphthenediimine (2.28 mmol, 1.0 equiv). The product was isolated as a yellow-green solid in 77% yield (1.22 mg). X-ray quality crystals were grown by vapor diffusion of pentane in to a solution of **2** in toluene.

Anal. Calcd. (Found) for $C_{44}H_{48}N_2O_2Ni$: C, 75.98 (75.45); H, 6.96 (7.30); N, 4.03 (3.68). ¹H NMR (CDCl₃, 500 MHz) δ/ppm: 0.98 (s, 9H, tBu), 1.16 (s, 9H, tBu), 2.41 (s, 6H *o*-Me), 2.51 (s, 12H, *p*-Me), 6.30 (s, 1H, cat-H), 6.39 (s, 1H, cat-H) 6.77 (broad s, 2H, aryl-H), 7.05 (s, 4H, aryl-H), 7.39 (t, ³J_{HH} = 7.7 Hz, 2H, Ar–*H*), 7.98 (d, ³J_{HH} = 8.3 Hz, 2H, Ar–*H*). ¹³C NMR (CDCl₃

125.8 MHz) δ/ppm: 162.1 (C=N), 157.9 (C–O) , 143.3 (aryl–C), 142.0 (aryl–C), 138.6 (aryl–C), 136.9 (aryl–C), 135.2 (aryl–C), 131.5 (aryl–C), 130.1 (aryl–C), 129.8 (aryl–C), 129.3 (aryl–C), 127.0 (aryl–C), 122.9 (aryl–C), 111.0 (aryl–C), 110.8 (aryl–C), 34.2 (C(CH$_3$)$_3$) 34.1 (C(CH$_3$)$_3$), 32.2 (C(CH_3)$_3$), 29.3 (C(CH_3)$_3$), 21.4 (p–CH_3), 18.6 (o–CH_3). UV-vis-NIR (CH$_2$Cl$_2$) λ_{max}/nm (ε/ M^{-1} cm^{-1}): 320 (24,400), 426 (5490), 1026 (10,400)

Synthesis of (catCl$_4$)Ni(adi) (2b). Complex **2b** was prepared according to Method A using N,N'-bis(2,4,6-trimethylphenyl)acenaphthenediimine (152 mg, 0.364 mmol, 1.0 equiv), Ni(cod)$_2$ (100 mg, 0.364 mmol, 1.0 equiv), and tetrachloro-1,2-quinone (89 mg, 0.364 mmol, 1.0 equiv). The product was isolated as a dark green solid in 86% yield (225 mg). X-ray quality crystals were grown by vapor diffusion of pentane into a THF solution of the product.

Anal. Calcd. (Found) for C$_{36}$H$_{28}$N$_2$O$_2$Cl$_4$Ni: C, 59.96 (59.86); H, 3.91 (3.91); N, 3.88 (3.77). ^{1}H NMR (CDCl$_3$, 500 MHz) δ/ppm: 2.41 (s, 6H, o-Me), 2.56 (s, 12H, p-Me), 6.87 (d, $^3J_{HH}$ = 7.0 Hz, 2H, aryl-H), 7.07 (s, 4H, aryl-H), 7.50 (t, $^3J_{HH}$ =7.7 Hz, 2H, aryl-H), 8.08 (d, $^3J_{HH}$ = 8.4 Hz, 2H, aryl-H). ^{13}C NMR (CDCl$_3$, 125.8 MHz) δ/ppm: 169.2 (C=N), 157.5 (C–O), 146.0 (aryl-C), 140.1 (aryl–C), 138.0 (aryl–C).131.9 (aryl–C), 131.4 (aryl–C), 130.4 (aryl–C), 129.5 (aryl–C), 129.5 (aryl–C), 125.5 (aryl–C), 124.3 (aryl–C), 117.1 (aryl–C), 21.5 (aryl–CH_3), 18.8 ((aryl–CH_3). UV-vis-NIR (CH$_2$Cl$_2$) λ_{max}/nm (ε/M^{-1} cm^{-1}): 328 (23,700), 748 (7260).

Synthesis of (cat-tBu$_2$)Ni(pdi) (3a). Complex **3a** was prepared according to Method A using N,N'-bis(2,4,6-trimethylphenyl)-9,10-phenanthrenediimine (221 mg, 0.500 mmol, 1.0 equiv), Ni(cod)$_2$ (138 mg, 0.500 mmol, 1.0 equiv), and 3,5-di-$tert$-butyl-o-benzoquinone (110 mg, 0.500 mmol, 1.0 equiv). The product was isolated as a dark red solid in 86% yeild (298 mg).

The preparation of **3a** by Method B proceeded using 222 mg of 3,5-di-$tert$-butylcatechol (1.00 mmol, 1.0 equiv), 220 mg of (dme)NiCl$_2$ (1.00 mmol, 1.0 equiv), and 443 mg of N,N'-bis(2,4,6-trimethylphenyl)-9,10-phenanthrenediimine (1.00 mmol, 1 equiv). The product was isolated as a dark red solid in 77% yield (556 mg). X-ray quality crystals were grown by vapor diffusion of pentane into a solution of **3a** in toluene.

Anal. Calcd. (Found) for C$_{46}$H$_{50}$N$_2$O$_2$Ni: C, 76.57 (76.41); H, 6.98 (7.33); N, 3.88 (3.75). ^{1}H NMR (CDCl$_3$, 500 MHz) δ/ppm: 0.99 (s, 9H, tBu), 1.16 (s, 9H, tBu), 2.33 (s, 12H, o-Me), 2.45 (s, 6H, p-Me), 6.37 (s, 1H, cat-H), 6.38 (s, 1H, cat-H), 7.03-7.06 (m, 5H, aryl-H), 7.36 (d, $^3J_{HH}$ = 8.5 Hz, 2H, aryl-H), 7.61 (t, $^3J_{HH}$ = 7.5 Hz, 2H, aryl-H), 8.16 (d, $^3J_{HH}$ = 7.7 Hz, 2H, aryl-H). ^{13}C NMR (CDCl$_3$, 125.8 MHz) δ/ppm: 163.4 (C–O), 160.0 (C–O), 156.6 (C=N), 146.3 (aryl–C), 141.1 (aryl–C), 137.0 (aryl–C), 136.6 (aryl–C), 132.0 (aryl–C), 130.6 (aryl–C), 130.3 (aryl–C), 129.4 (aryl–C), 129.0 (aryl–C), 127.5 (aryl–C), 126.8 (aryl–C), 124.6 (aryl–C), 113.0 (aryl–C), 111.9 (aryl–C), 34.3 (C(CH$_3$)$_3$) 34.2 (C(CH$_3$)$_3$), 32.0 (C(CH_3)$_3$), 29.4 (C(CH_3)$_3$), 21.6 (p–CH_3), 19.0 (o–CH_3). UV-vis-NIR (CH$_2$Cl$_2$) λ_{max}/nm (ε/M^{-1} cm^{-1}): 260 (35,400), 512 (2840), 1186 (16,500).

Synthesis of (catCl$_4$)Ni(pdi) (3b). Complex **3b** was prepared according to Method A using N,N'-bis(2,4,6-trimethylphenyl)-9,10-phenanthrenediimine (161 mg, 0.364 mmol, 1.0 equiv), Ni(cod)$_2$ (100 mg, 0.364 mmol, 1.0 equiv), and tetrachloro-1,2-quinone (89 mg, 0.364 mmol, 1.0 equiv). The product was isolated as a dark red-orange solid in 88% yield (238 mg). X-ray quality crystals were grown from a CH$_2$Cl$_2$ solution of the complex chilled to –35 °C.

^{1}H NMR (CDCl$_3$, 500 MHz) δ/ppm: 2.38 (s, 12H, o-Me), 2.40 (s, 6H, p-Me), 7.08 (s, 4H, aryl-H), 7.12 (t, $^3J_{HH}$ =7.8 Hz, 2H, aryl-H), 7.48 (d, $^3J_{HH}$ = 8.4 Hz, 2H, aryl-H), 7.68 (t, $^3J_{HH}$ = 7.5 Hz, 2H, aryl-H), 8.12 (d, $^3J_{HH}$ = 8.1 Hz, 2H, aryl-H). ^{13}C NMR (CDCl$_3$, 125.8 MHz) δ/ppm: 160.1

(C=N), 157.2 (C–O), 144.4 (aryl-C), 137.9 (aryl-C), 133.5 (aryl-C), 133.1 (aryl-C), 130.0 (aryl-C), 129.8 (aryl-C), 128.3 (aryl-C), 126.5 (aryl-C), 125.0 (aryl-C), 117.8 (aryl-C), 115.9 (aryl-C), 21.5 (p–CH_3), 19.1 (o–CH_3). UV-vis-NIR (CH_2Cl_2) λ_{max}/nm (ε/M^{-1} cm^{-1}): 352 (12,600), 876 (10,000). **Oxidation of (cat-tBu$_2$)Ni(adi) (2a).** Solid AgOTf (108 mg, 0.419 mmol, 1.0 equiv) was added to a stirred solution of **2a** (292 mg, 0.419 mmol, 1.0 equiv) in 10 mL of MeCN. An immediate change in the solution color from green to brown occurred with concomitant precipitation of a dark solid. The reaction mixture was stirred for 12 hr and then filtered. The solvent was removed from the filtrate under reduced pressure and the residue was washed three times with Et$_2$O. The product, [(cat-tBu$_2$)Ni(adi)][OTf], **[2a][OTf]**, was isolated as a brown solid in 96% yield (341 mg). UV-vis-NIR (MeCN) λ_{max}/nm (ε/M^{-1} cm^{-1}): 390 (3250), 786 (655).

Reduction of (cat-tBu$_2$)Ni(adi) (2a). A cold (–35 °C) solution of **2a** (300 mg, 0.431 mmol, 1.0 equiv) in MeCN was combined with decamethylcobaltocene (142 mg, 0.431 mmol, 1.0 equiv) and stirred at ambient temperature for 30 h. The solvent was removed under reduced pressure. The green residue was washed with toluene and then with pentane to afford the product, [Cp*$_2$Co][(cat-tBu$_2$)Ni(adi)], **[Cp*$_2$Co][2a]**, in 94% yield (417 mg). UV-vis-NIR (MeCN) λ_{max}/nm (ε/M^{-1} cm^{-1}): 434 (4880), 774 (5050).

X-ray Data Collection and Reduction. X-ray diffraction data for **1-6** were collected for single crystals mounted on a glass fiber using Paratone oil. Data was acquired using a Bruker CCD platform diffractometer equipped with a CCD detector at 143 K using Mo Kα (λ = 0.71073 Å) radiation, which was wavelength selected with a single-crystal graphite monochromator. The SMART program package was to determine unit-cell parameters and for data collection. The raw frame data were processed using SAINT and SADABS to yield the reflection data file. Subsequent calculations were carried out using the SHELXTL program suite. Analytical scattering factors for neutral atoms were used throughout the analyses. Hydrogen atoms were generated in calculated positions and refined using a riding model. ORTEP diagrams were generated using *ORTEP-3* for Windows. Diffraction data for complexes **1-3** are shown in Table 2.4.

2.6 References

1. Hagfeldt, A.; Boschloo, G.; Sun, L.; Kloo, L.; Pettersson, H. *Chem Rev* **2010**, *110*, 6595.
2. Meyer, T. J. *Accounts Chem Res* **1989**, *22*, 163.
3. Campagna, S.; Puntoriero, F.; Nastasi, F.; Bergamini, G.; Balzani, V. In *link.springer.com*; Topics in Current Chemistry; Springer Berlin Heidelberg: Berlin, Heidelberg, 2007; Vol. 280, pp. 117–214.
4. Juris, A.; Balzani, V.; Barigelletti, F.; Campagna, S.; Belser, P.; Zelewsky, von, A. *Coordination Chemistry Reviews* **1988**, *84*, 85.
5. Endicott, J. F.; Schlegel, H. B.; Uddin, M. J.; Seniveratne, D. S. *Coordination Chemistry Reviews* **2002**, *229*, 95.
6. Cummings, S. D.; Cheng, L.-T.; Eisenberg, R. *Chem. Mater* **1997**, *9*, 440.
7. Weinstein, J. A.; Tierney, M. T.; Davies, E. S.; Base, K.; Robeiro, A. A.; Grinstaff, M. W. *Inorg Chem* **2006**, *45*, 4544.
8. Mitsopoulou, C. A. 2010; Vol. 254, pp. 1448–1456.

9. Deplano, P.; Pilia, L.; Espa, D.; Mercuri, M. L.; Serpe, A. *Coordination Chemistry Reviews* **2010**, *254*, 1434.

10. Paw, W.; Cummings, S.; Adnan Mansour, M.; Connick, W.; Geiger, D.; Eisenberg, R. *Coordination Chemistry Reviews* **1998**, *171*, 125.

11. Zhang, J.; Du, P.; Schneider, J.; Jarosz, P.; Eisenberg, R. *J Am Chem Soc* **2007**, *129*, 7726.

12. Linfoot, C. L.; Richardson, P.; McCall, K. L.; Durrant, J. R.; Morandeira, A.; Robertson, N. *Solar Energy* **2011**, *85*, 1195.

13. Sarkar, B.; Hübner, R.; Pattacini, R.; Hartenbach, I. *Dalton Trans*. **2009**, 4653.

14. Shavaleev, N. M.; Davies, E. S.; Adams, H.; Best, J.; Weinstein, J. A. *Inorg Chem* **2008**, *47*, 1532.

15. Anbalagan, V.; Srivastava, T. S. *Journal of Photochemistry and Photobiology A: Chemistry* **1995**.

16. Anbalagan, V.; Srivastava, T. *Polyhedron* **2004**, *23*, 3173.

17. Deibel, N.; Schweinfurth, D.; Fiedler, J.; Záliš, S.; Sarkar, B. *Dalton Trans*. **2011**, *40*, 9925.

18. Vogler, A.; Kunkely, H. *J. Am. Chem. Soc*. **1981**, *103*, 1559.

19. Espa, D.; Pilia, L.; Makedonas, C.; Marchiò, L.; Mercuri, M. L.; Serpe, A.; Barsella, A.; Fort, A.; Mitsopoulou, C. A.; Deplano, P. *Inorg Chem* **2014**, 140109112322007.

20. Benedix, R.; Hennig, H. *Inorganica Chimica Acta* **1988**, *141*, 21.

21. Miller, T. R.; Dance, I. G. *J. Am. Chem. Soc*. **1973**, *95*, 6970.

22. Brasse, M.; Cámpora, J.; Davies, M.; Teuma, E.; Palma, P.; Álvarez, E.; Sanz, E.; Reyes, M. L. *Adv. Synth. Catal*. **2007**, *349*, 2111.

23. Sgro, M. J.; Stephan, D. W. *Dalton Trans*. **2010**, *39*, 5786.

24. Carugo, O.; Djinovi, K.; Rizzi, M.; Castellani, C. B. *J. Chem. Soc., Dalton Trans*. **1991**, 1551.

25. Bill, E.; Bothe, E.; Chaudhuri, P.; Chlopek, K.; Herebian, D.; Kokatam, S.; Ray, K.; Weyhermüller, T.; Neese, F.; Wieghardt, K. *Chemistry–A European Journal* **2005**, *11*, 204.

26. Chlopek, K.; Bothe, E.; Neese, F.; Weyhermuller, T.; Wieghardt, K. *Inorg Chem* **2006**, *45*, 6298.

27. Cope-Eatough, E.; Mair, F.; Pritchard, R.; Warren, J.; Woods, R. *Polyhedron* **2003**, *22*, 1447.

28. Best, J.; Sazanovich, I. V.; Adams, H.; Bennett, R. D.; Davies, E. S.; Meijer, A. J. H. M.; Towrie, M.; Tikhomirov, S. A.; Bouganov, O. V.; Ward, M. D.; Weinstein, J. A. *Inorg Chem* **2010**, *49*, 10041.

29. Adams, C. J.; Fey, N.; Parfitt, M.; Pope, S. J. A.; Weinstein, J. A. *Dalton Trans*. **2007**, 4446.

30. Oblad, P. F.; Bercaw, J. E.; Hazari, N.; Labinger, J. A. *Organometallics* **2010**, *29*, 789.

31. Ohtsu, H.; Tanaka, K. *Angew. Chem. Int. Ed*. **2004**, *43*, 6301.

32. Ohtsu, H.; Tanaka, K. *Chemistry–A European Journal* **2005**, *11*, 3420.

33. Zhong, H. A.; Labinger, J. A.; Bercaw, J. E. *J Am Chem Soc* **2002**, *124*, 1378.

34. Liu, J.; Li, Y.; Li, Y.; Hu, N. *J. Appl. Polym. Sci*. **2008**, *109*, 700.

35. Ketterer, N.; Ziller, J.; Rheingold, A. *Organometallics* **2007**.

Chapter 3
Metal Influence on LL′CT

3.1 Introduction

Dye-sensitized solar cells (DSSCs) have been widely studied for their potential as low-cost, renewable energy solutions.[1,2] The most well studied transition-metal dyes used in DSSCs are the ruthenium poly-bipyridine [Ru(bpy)$_n$] family of chromophores.[3-5] While efficiencies of up to 12% have been reported by Grätzel and coworkers for their DSSCs employing these dyes, ruthenium is rare and expensive, limiting the viability of these 'Grätzel cells' as a large scale source of renewable energy. Ru(bpy)$_n$ dyes operate via metal-to-ligand charge transfer (MLCT) from the ruthenium 't_{2g}' orbitals to the π^* orbitals of the bipyridine ligands. Because the donor orbitals originate from the metal atom, changes to the identity of the metal atom (i.e. from ruthenium to iron or osmium) have a substantial impact on the photo- and electrochemical properties of the chromophores.[6-8] The metal dependent behavior of MLCT chromophores is best illustrated through a comparison of the excited state behavior of the Group 8 series of tris-polypyridine complexes. In [M(bpy)$_n$]$^{2+}$ complexes when M = Ru(II) or Os(II) the metal 'e_g' orbitals are higher energy than the bpy π^* orbitals and the ^{1}MLCT excited state of the Ru(II) and Os(II) complexes quickly decay to a long-lived ^{3}MLCT excited-state. However, in [Fe(bpy)$_3$]$^{2+}$ the metal 'e_g' orbitals are lower energy than the bpy π^* orbitals which leads to significantly divergent excited state behavior.[7-12] The ^{1}MLCT excited-state of the Fe(II) analogue undergoes an ultrafast relaxation through a number of different states to the ^{5}d-d state.[13] This difference in excited state properties has a significant impact on the potential usefulness of first-row metal chromophores.

Prior to the revelation that charge injection from an excited chromophore- into TiO$_2$ occurs on ultra-fast time scales (> 1 ps)[14], dye design for DSSCs was largely focused on second- and third-row transition metal compounds due to their propensity for producing long lived triplet

states that facilitated charge injection into the semiconductor. Since this discovery there has been renewed interest in the use of first-row transition metal dyes which had been thought to possess insufficient lifetimes to act as sensitizers for DSSCs. In fact, iron analogues to the traditional ruthenium chromophores have been successfully implemented in DSSCs as sensitizers for TiO$_2$.[15-17] Although these devices display significantly decreased efficiencies, compared to the ruthenium DSSCs, these new systems represent a step forward for first row transition MLCT dyes.

Another approach to dye design with first-row transition metals is one that deprecates the metals role in the light absorbing processes. The most well studied dye molecules of this type are (dithiolene)M(diimine) complexes, which give rise to photo-induced charge separation through ligand-to-ligand charge transfer (LL′CT) from the dithiolene donor to the diimine acceptor.[18] These donor-acceptor (D-A) complexes have been implemented as sensitizers in solar energy conversion applications.[19,20] A majority of D-A LL′CT dyes employ platinum or palladium. The ligand dominated properties of these chromophores leads one to question if it is necessary to use the expensive metals typically employed in these LL′CT chromophores. There are relatively few studies which examine the entire Group 10 series for a specific donor-acceptor combination to determine the metal atoms importance in the LL′CT process.[21-27] Still, the available data suggests that, compared to the MLCT dyes, the metal atom has a much smaller influence on the properties of D-A LL′CT dyes.

The previous chapter discussed a new series of nickel(II) D-A LL′CT dye molecules that use electron-rich, catecholate donor, and electron-poor α-diimine acceptor ligands. This family of complexes display D-A behavior comparable to (dithiolene)M(diimine) complexes, and the spectroscopic and electrochemical properties of these dyes were found to be highly tunable

through alterations to donor and acceptor ligands. Donor-acceptor complexes that use catecholates donor are less well studied than their dithiolene analogues and importance of the metal ions identity to the properties displayed by these systems is even less well understood.[28-30]

M = Ni (1), Pd (2), Pt (3)
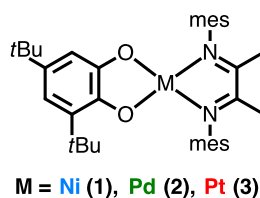
Figure 3.1. Complexes **1-3**.

To better understand the metal atoms role in the D-A behavior of catecholate-diimine complexes palladium(II) and platinum(II) analogues of the D-A LL′CT complex (cat-tBu$_2$)Ni(bdi) (Figure 3.1), presented in Chapter 1, were prepared [(cat-tBu$_2$)$^{2-}$ = 3,5 di-$tert$-butylcatecholate, bdi = N,N′-bis(2,4,6-trimethylphenyl)–2,3-butanediimine]. The UV-vis-NIR absorption spectra of complexes **2** and **3** feature strong LL′CT absorptions with maxima near the maxima of complex **1**. Complexes **2** and **3** also display electrochemical behavior remarkably similar to the nickel complex. Though the three complexes are similar in many ways there are small metal dependencies observed in the spectroscopic and electrochemical properties of the dyes. DFT and TD-DFT calculations were performed for each complex to supplement experimental data and to gain insight into changes to the electronic structure and LL′CT transitions caused by substitution of the metal ion. These calculations revealed that the metal dependencies are due to variations in the amount of metal d orbital character in the bdi centered LUMO.

51

3.2 Results

3.2.1 Synthesis and Characterization of (cat-tBu2)M(bdi) Complexes.
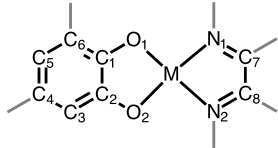
Palladium(II) and platinum(II) analogues of complex **1** were prepared as outlined in Scheme 3.1. The synthesis of the palladium complex, **2**, was accomplished by the addition of a slurry of K_2(cat-tBu$_2$) in Et$_2$O to (bdi)PdCl$_2$ suspended in Et$_2$O. The blue-green (cat-tBu$_2$)Pd(bdi) was isolated in 67% recrystallized yield. Complex **3** was obtained in a similar manner from (bdi)PtCl$_2$ with THF as the solvent and was isolated as a dark blue solid in 53% recrystallized yield.

Scheme 3.1. Synthesis of **2** and **3**.
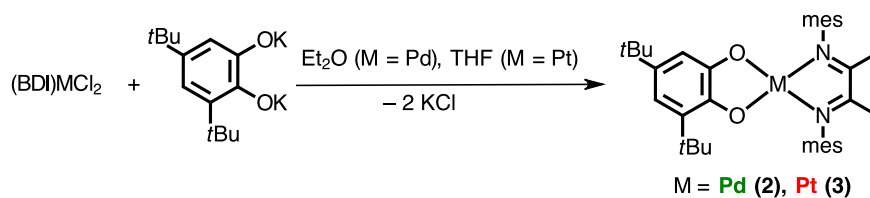
Solution phase ^{1}H and ^{13}C NMR spectra of **2** and **3** are consistent with the NMR spectra of **1** and are consistent with the formation of the desired products. Sharp signals observed in the normal diamagnetic region for both complexes suggested diamagnetic M(II) species in square-planar coordination environments. As was observed for **1**, complexes **2** and **3** displayed *Cs* symmetry in solution arising from the asymmetric chemical environment imposed by the 3,5 di-*tert*-butylcatecholate donor ligand. In complex **1** only the backbone methyl groups, and aryl protons of the mesityl substituents of the bdi ligand appeared as two separate peaks. The asymmetry was more pronounced in the NMR spectra of **2** and **3**, and all resonances corresponding to the bdi acceptor ligand were observed as two discrete signals.

Table 3.1 Selected bond distances (Å) for donor-acceptor complexes **1** and **3**.

	Bond Distances / Å	
	1 (M = Ni)	**3 (M = Pt)**
M–O	1.8184(11)	1.9671(30)
M–O	1.8101(11)	1.9881(29)
M–N	1.8703(14)	1.9730(38)
M–N	1.8617(14)	1.9731(34)
O	1.350(2)	1.3512(49)
O	1.3535(19)	1.3512(49)
C	1.404(2)	1.4036(60)
C	1.405(2)	1.4061(61)
C	1.402(2)	1.4014(60)
C	1.401(3)	1.4021(66)
C	1.398(3)	1.3954(64)
C	1.390(2)	1.3959(59)
N	1.295(2)	1.3125(56)
N	1.299(2)	1.3071(56)
C	1.474(2)	1.4653(62)
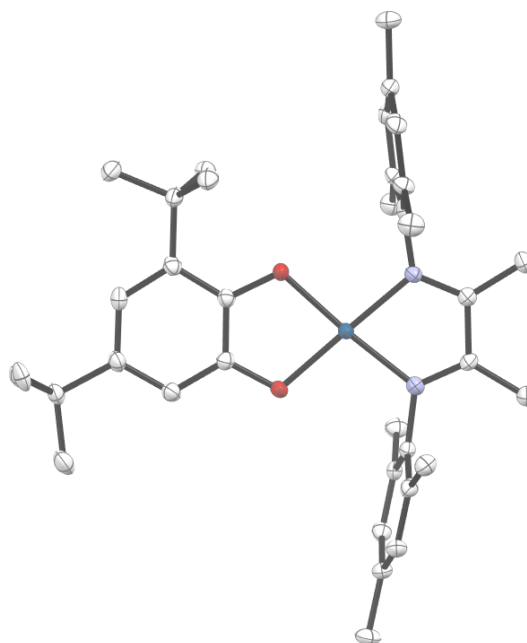
Figure 3.1 ORTEP diagram of (cat-tBu$_2$)Pt(bdi), **3**. Ellipsoids are drawn at 50% probability. Hydrogen atoms and solvent molecules have been omitted for clarity.

As bond lengths within redox-active ligands are generally oxidation state dependent single crystal X-ray diffraction can be particularly useful when making experimental oxidation state assignments. The solid-state structure of complex **3** could obtained for this report, but at this time single crystals of **2** suitable for X-ray diffraction have been elusive. Figure 3.1 shows

the molecular structure of complex **3** and Table 3.1 contains selected bond distances and angles for **1** and **3**. The molecular geometry of **3** reveals the ligands bound in a square-planar arrangement around the metal center. The metal-ligand bonds in **3** are consistent with those expected for a platinum(II) bound to catecholate and α-diimine ligands. The bond distances found for complex **3** are consistent with a Pt(II) metal center bound to a fully-reduced catecholate and a fully-oxidized diimine. The C–O bond distances of **3** match those expected bond for a C–O single-bond (1.35 Å) and are significantly longer than the C–O bonds of the semi-quinonate or quinone (1.31 and 1.23, respectively).[31-34] Additionally, no evidence of the double-bond localization in the C_6 ring, typical observed for oxidized catecholates, was detected. The distances C-N bond lengths of the bdi ligand in complex **3** were 1.31 Å, slightly elongated compared to the C-N bonds of **1**, and the long C–C bond in the diimine back bone in **3** (1.47 Å), is within the range expected for a C–C single bond. Both metrics are consistent with the bdi ligand in the fully oxidized diimine state.[35-37] The crystallographic data obtained **3** provides evidence that the complex exits as (cat-tBu$_2$)Pt(bdi) with all components in the desired oxidation states.

3.2.3 Electronic Properties

The intense LL′CT band at 816 nm (1.52 eV) that dominates the absorption profile of the nickel(II) complex **1**, is also observed in complexes **2** and **3**. The UV-vis-NIR absorption spectra of **1-3**, dissolved in dichloromethane at 298 K, are depicted in Figure 3.2. Substitution of nickel for palladium in resulted in a red-shift of the charge-transfer in **2** to 878 nm (1.41 eV) and a decrease in intensity (ε = 4970 $M^{-1}cm^{-1}$). For complex, **3**, a significant blue-shift and increase in intensity of the charge-transfer band from both **1** and **2** was observed (λ_{max} = 754 nm, 1.64 eV ; ε

= 9570 M^{-1}cm^{-1}). Overall, a non-periodic trend in the energy and intensity of the LL′CT absorptions in this Group 10 series emerged where Pt > Ni > Pd.

Table 3.2. Absorption data in dichloromethane solution and solvatochromic shift of **1-3**.

	Abs. λ_{max}	estimated E_{es}	solvatochromic shift
1	818	9320(1.16)	0.23
2	874	8205 (1.02)	0.23
3	754	10561 (1.31)	0.18
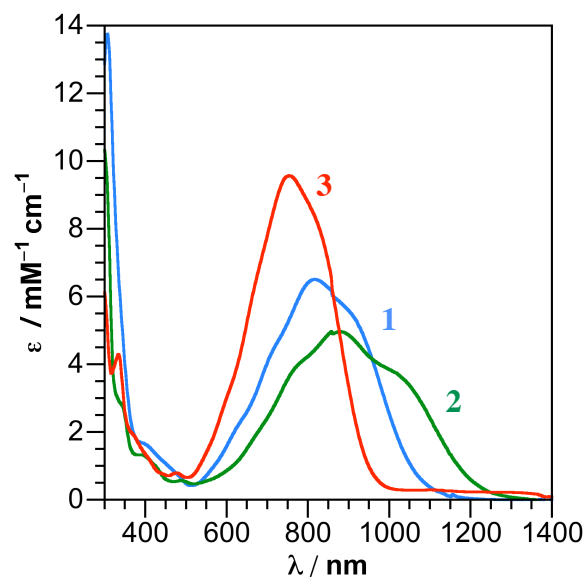
Figure 3.2. UV-vis-NIR absorption spectra of complexes **1-3** in DCM at 298 K.

Negative solvatochromic behavior is a common feature observed in LL′CT dyes as a result of the large ground-state dipole moment caused by the localization of electron density on the donor ligand. Figure 3.3a shows the solvent dependent UV-vis-NIR absorption spectra of **3**. The solvatochromic shift (SS) of **1-3** was calculated from the slope of the line generated by a plot of the LL′CT excited state energy as a function of the Eisenberg and coworkers' empirical solvent number (ESN)[18] as shown in Figure 3.3b. The excited state energies used in Figure 3.3b were estimated from the low-energy onset of the absorption curve as described in Chapter 2. Table 3.2 tabulates the absorption maxima, estimated excited state energies, and solvatochromic shifts of **1-3**. In Chapter 2 where it was found that complexes with higher energy LL′CT absorption have larger SS values. No such trend emerged between complexes **1-3**. Complexes **1**

and **2** have the same SS (0.23) and complex **3,** which has the highest energy LL′CT, has the

smallest SS (0.18). Because SS is related to the ground state dipole of the D-A complex, and

because complexes **1-3** use the same donor and acceptor ligands it is not surprising that the

ground state dipoles, and SSs of these complexes are very similar.
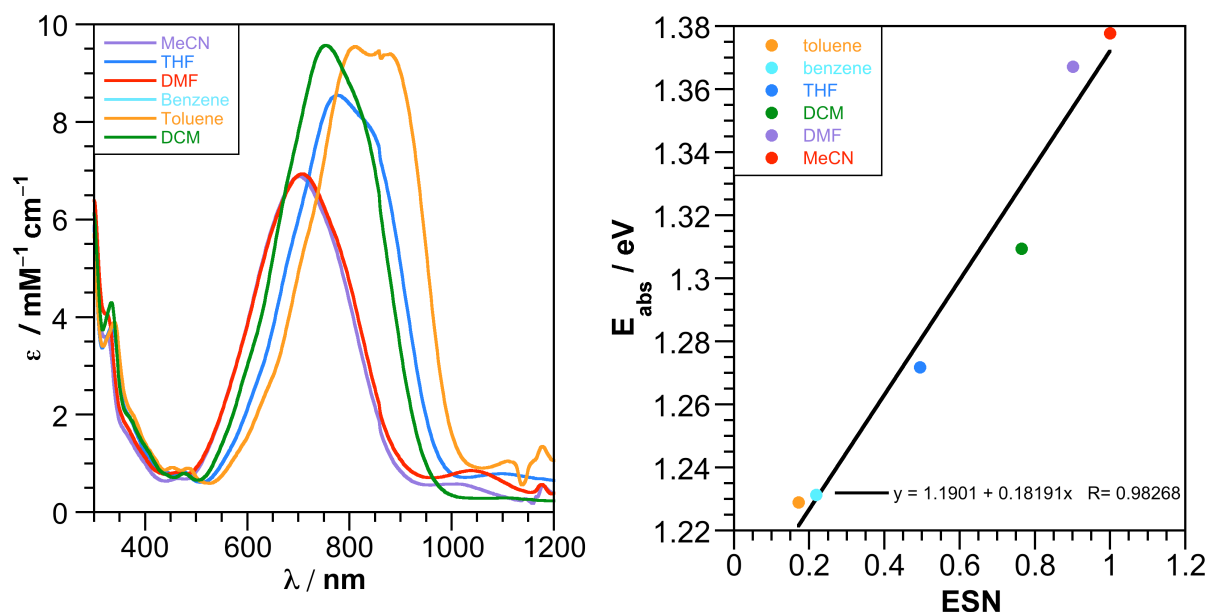
Figure 3.3. (a) UV-vis-NIR spectra of **3** in different solvents at 298 K. (b) plot of the estimated excited state energy for **1a** vs. ESN[18] for each solvent.

Cyclic and differential pulse voltammetry experiments were preformed for complexes **1-3**

to obtain more information about their electronic structure. The potentials of the first oxidative (E

$^{+/0}$) and the first reductive (E$^{0/−}$) processes provide equilibrium HOMO and LUMO energy levels,

respectively. The difference between the two redox events (ΔE = E$^{+/0}$ − E$^{0/−}$) can therefore be

correlated to the HOMO-LUMO gap (ΔHL). Cyclic voltammograms of each complex, taken in

0.1 M [Bu$_4$N][PF$_6$] THF solutions and referenced to the [Cp$_2$Fe]$^{+/0}$ redox couple, are shown in

Figure 3.4. Reduction potentials and ΔE values, obtained using differential pulse voltammetry

are provided in Table 3.3. The cyclic voltammetry of complex **1** in DCM solution was discussed

in Chapter 1, it showed two catecholate-centered oxidative events and a single bdi-based

reduction. Performing the electrochemical experiments in THF, which allows scans to more negative potentials, revealed a second reversible, diimine-centered reductive event that could not be observed in DCM. The cyclic voltammograms of **2** and **3** in THF are remarkably similar to that of **1.** Each complex displayed two reversible, bdi-centered reductive processes and two, catecholate-centered oxidative processes. The first oxidative event displayed by each complex was reversible and the reversibility of second oxidation ($E^{2+/+}$) varied depending on the metal center. Complexes **1** and **2** display nearly identical potentials for $E^{+/0}$, but the first oxidation of complex **3** was shifted nearly 150 mV more positive. The potentials of $E^{0/-}$ for complexes **1** and **3** are virtually identical, but the first reduction of complex **2** was 150 mV more positive. A non-periodic trend in ΔE of the (cat-tBu$_2$)M(bdi) complexes where ΔE **3** > **1** > **2**, which mirrors the trend in the LL′CT energy of **1-3** discussed above.
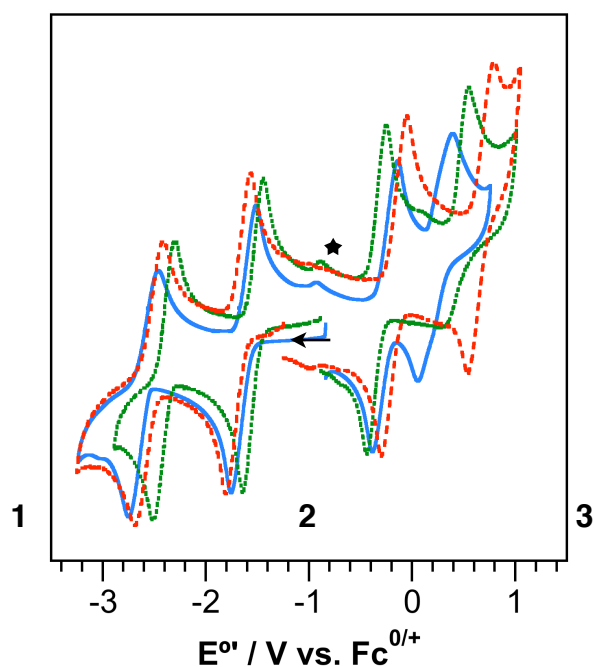
Figure 3.4. Cyclic voltammetry plots for complexes **1** (blue), **2** (green) and **3** (red). Data were collected at 298 K in THF solutions that were 1.0 mM in analyte and 0.1 M in [Bu$_4$N][PF$_6$] electrolyte using a glassy carbon working electrode. All potentials were referenced to [Cp$_2$Fe]$^{+/0}$ using an internal standard.

Table 3.3. Reduction potentials (V vs [Cp$_2$Fe]$^{+/0}$) for complexes **1-3**.

		$E^{\circ\prime}$			
	$E^{2-/1-}$	$E^{1+/0}$	$E^{0/1-}$	$E^{1-/2-}$	ΔE
1	-2.66	-1.67	-0.30	0.18	1.38
2	-2.38	-1.52	-0.32	0.58	1.20
3	-2.54	-1.68	-0.17	0.66	1.51

3.2.4 DFT Calculations

Table 3.4. Calculated and experimental bond distances of (cat-tBu$_2$)M(bdi) complexes **1-3**.

	Calculated Bond Distances (Experimental) / Å		
	1	**2**	**3**
M–O	1.83 (1.818)	1.983	1.989 (1.967)
M–O	1.84 (1.810)	1.989	1.994 (1.988)
M–N	1.863 (1.870)	1.988	1.980 (1.973)
M–N	1.865 (1.862)	1.989	1.982 (1.973)
O	1.337 (1.350)	1.336	1.340 (1.351)
O	1.340 (1.354)	1.338	1.342 (1.351)
N	1.334 (1.295)	1.335	1.341 (1.313)
N	1.335 (1.299)	1.335	1.341 (1.307)
C	1.432 (1.474)	1.433	1.426 (1.465)

Density functional theory (DFT) calculations were performed for the (cat-tBu$_2$)M(bdi) model complexes **1-3** to get a more detailed description of the electronic structure of these

complexes. Geometry optimizations performed on **1** and **3** at the PBE/TZVP level of theory[38-40]

produced bond lengths in good agreement with the experimental data, with calculated bond

lengths within 0.04 Å. Table 3.4 contains metrical parameters of the optimized structures of **1-3**

along with experimental data for **1** and **3**. Calculated bond distances of **2** were quite similar to the

other members of the series.
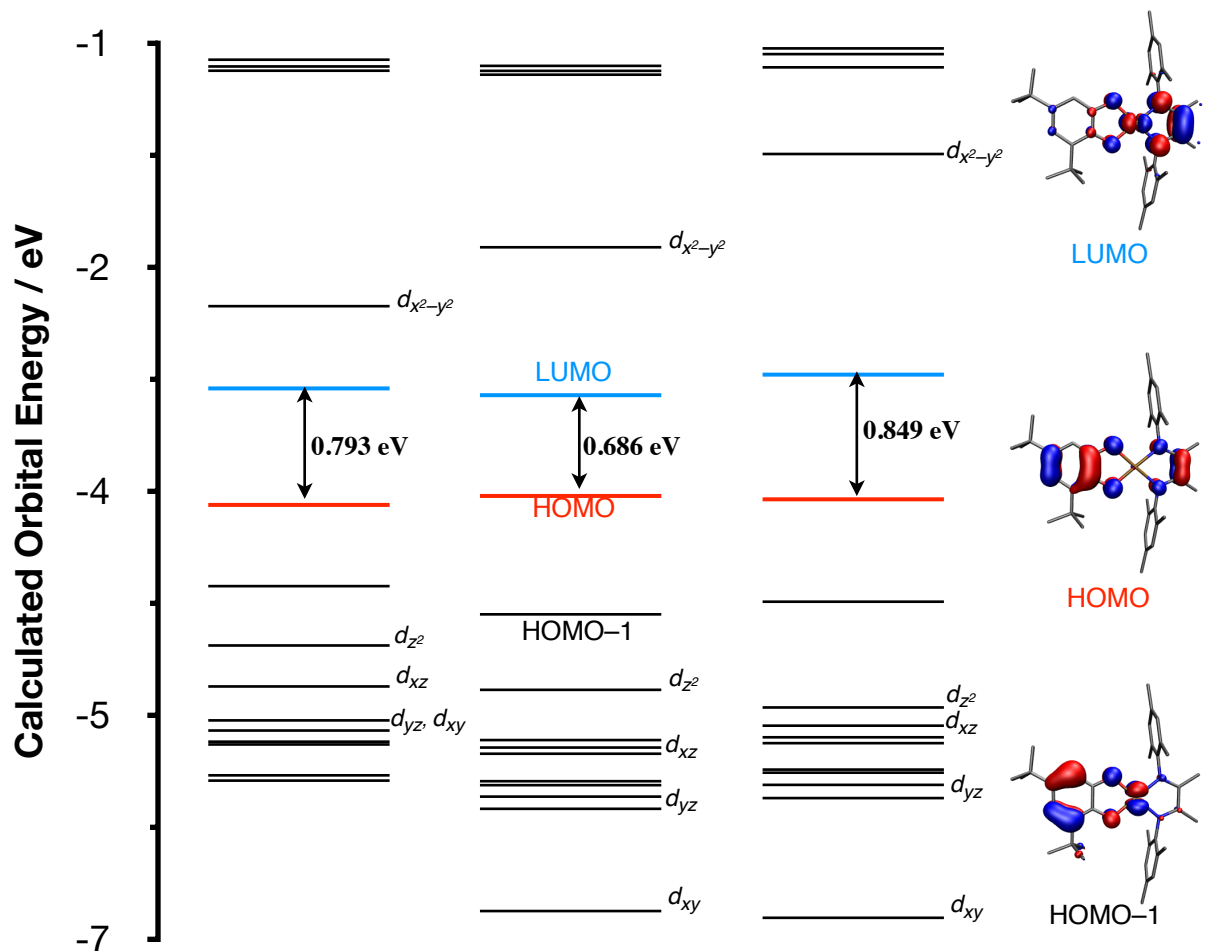
Figure 3.5. Calculated MO diagram and Δ_{HL} for **1-3** (left). Calculated KS orbitals of **3** (representative of the KS orbitals of the entire series) that are involved in the LL′CT excitations as representative of the series (right).

Electronic structure calculations produced frontier molecular orbitals for **1-3** that were

strikingly consistent across the series. The calculated molecular orbital diagrams of **1-3** and the

HOMO–1, HOMO and LUMO Kohn-Sham (KS) orbitals of complex **3** are shown in Figure 3.5.

The non-periodic trend found in the experimental measurements of ΔHL in **1-3** is reflected in the calculated values of ΔHL where **3** > **1** > **2** as shown in Figure 3.5. Mulliken population analysis (MPA) was used to quantify the parentage of the frontier orbitals in terms of the percentage of each molecular orbital originating from the catecholate, diimine or metal. The results of the MPA calculations for **1-3** are compiled in Table 3.5. Between 71–72% of the HOMOs of **1-3** are localized on the catecholate donor ligand. The HOMO of each complex also showed significant diimine character (23–24%) and metal orbitals accounted for only 3–4%. The LUMOs of **1-3** are primarily composed of bdi π^* orbital character (60–63%) with 24–26% catecholate character. Significantly higher metal d_{yz} orbital character was calculated in the LUMOs of these complexes that was observed in the HOMOs. The amount of metal character in the LUMO is dependent on the metal atom and increases in the order Pd (11%) < Ni (15%) < Pt (16%) which follows the trend in ΔHL observed for these complexes.

Table 3.5. Calculated energies and composition of selected molecular orbitals of **1-3**.

Compound	Orbital	Energy / eV	Composition / %			
			M	d orbital	(cat-	bdi
1	LUMO+1	-2.69	51.8	x^2	21.2	27
	LUMO	-3.25	14.7	yz	22.7	62.6
	HOMO	-4.04	3.8	N/A	72.9	23.3
	HOMO–1	-4.59	45.9	xz	50	4.1
2	LUMO+1	-2.29	43.5	x^2	20.9	35.6
	LUMO	-3.29	11.5	yz	25	63.5
	HOMO	-3.98	3.2	N/A	72.5	24.3
	HOMO–1	-4.79	12.3	xz	87.1	0.6
3	LUMO+1	-1.65	25.5	x^2	12.1	62.4
	LUMO	-3.15	16.3	yz	24.1	59.6
	HOMO	-4	3.6	N/A	72.3	24.1
	HOMO–1	-4.7	22	xz	73.7	4.3

Time dependent DFT (TD-DFT) calculations (PBE/TZVP) were performed using the optimized ground state (GS) molecular structures to aid the interpretation of the electronic transitions observed in the absorption spectra. The calculated excitations energies for **1-3** with the highest oscillator strengths (f), a measure of the electronic transitions probability comparable to the extinction coefficient, were in excellent agreement with the observed LL′CT absorptions. The first 40 singlet excitations, calculated for **1-3** plotted vs f are shown in Figure 3.6 with their UV-vis-NIR absorption spectra. Table 3.6 contains the energies, oscillator strengths and composition of the predicted excitations that display LL′CT character. The calculated low-energy excitation with the greatest f for **1-3** were primarily HOMO→LUMO transitions. Two

excitations with HOMO→LUMO character were predicted for complexes **1** and **3**, each displaying mixing from a HOMO–1→LUMO component. For both, the excitation with dominant HOMO→LUMO character has a much larger oscillator strength than the primarily HOMO–1→LUMO excitation. Complex **2** was predicted to have only one HOMO→LUMO excitation, and this excitation did not show any mixing with a HOMO–1→LUMO transition. These calculations provide additional evidence that the charge transitions displayed by these complexes are catecholate-to-diimine excitations.

Table 3.6. Calculated and Experimental LL′CT absorptions for **1-3**

	Energy / eV (nm)		f	State no.	Composition
	Calculated	Observed			
1	1.48 (837)		0.03	2	HOMO–1→LUMO (81%), HOMO→LUMO (17%)
	1.53 (803)	1.52 (818)	0.18	3	HOMO→LUMO (81%), HOMO–1→LUMO (17%)
2	1.45 (849)		0.22	1	HOMO→LUMO (95%)
	1.64 (754)	1.42 (874)	0.01	2	HOMO–1→LUMO (97%)
3	1.68 (739)		0.2	1	HOMO→LUMO (72%), HOMO–1→LUMO (26%)
	1.75 (707)	1.65 (754)	0.08	2	HOMO–1→LUMO (72%), HOMO→LUMO (26%)
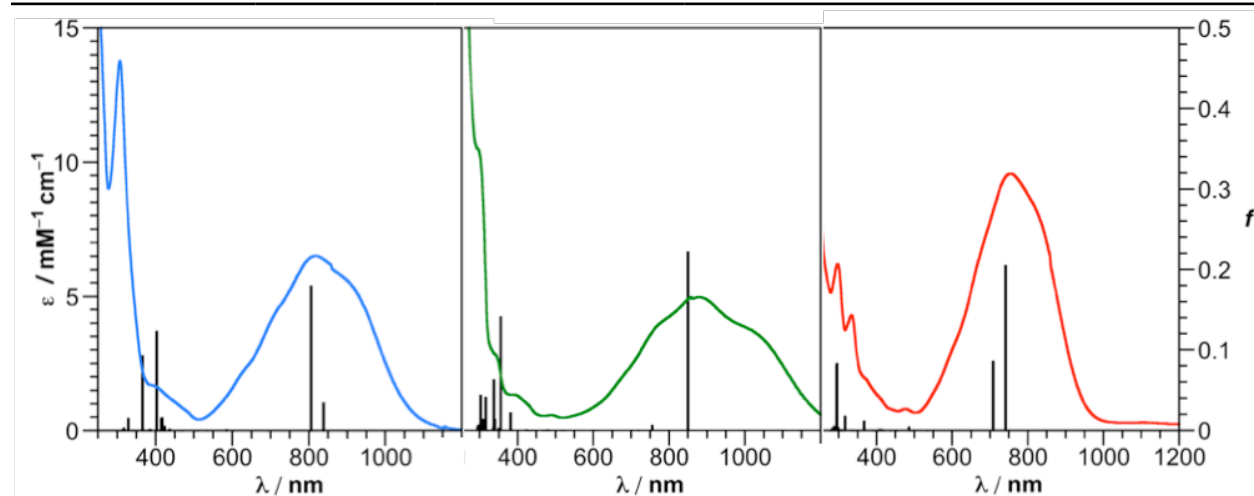
Figure 3.6. Calculated excitations of **1-3** vs. f with experimentally obtained UV-vis-NIR spectra. (a) **1** (b) **2** (c) **3**.

3.3 Discussion

3.3.1 Synthesis and Characterization of (cat-tBu2)M(bdi) D-A LL′CT complexes.

This chapter presents our investigations into the role of the metal in the LL′CT behavior of our (cat-tBu$_2$)M(bdi) model system. The influence of metal atom identity in catecholate-diimine D-A LL′CT dyes was investigated by preparing palladium(II) and platinum(II) analogues of the (cat-tBu$_2$)Ni(bdi) D-A LL′CT complex discussed in Chapter 1. Complexes **2** and **3** were obtained in reasonable yields by treating the (bdi)MCl$_2$ starting material with the doubly deprotonated catecholate. The X-ray structure of complex **3** was strikingly similar that of complex **1** and confirmed the desired catecholate, diimine and platinum(II) oxidation states in the complex. DFT optimized GS structures for complexes **1** and **3** accurately described the X-ray structures of both complexes, and the calculated structure of **2** was nearly identical to the other members of the series. So while X-ray quality crystals of **2** proved elusive, the similarities observed in the NMR spectra and calculated geometry of **2** to those of **1** and **3** provided the confidence to infer that **2** also exists in the desired (cat-tBu$_2$)Pd(bdi) conformation.

The spectroscopic and electrochemical behavior displayed by these (cat-tBu$_2$)M(bdi) model complexes is remarkably consistent across the series. Regardless of metal identity, the LL′CT band is the dominant feature in the UV-vis-NIR spectra and the cyclic voltammograms of each complex displays two, diimine-centered reductions and two catecholate-centered oxidations. However, distinct differences between the three complexes were detected in these data. Spectroscopically, the metal dependence on the energy and intensity of the absorption was Pt > Ni > Pd. TD-DFT excited state calculations produced energies for the LL′CT excitations that are in excellent agreement with the experimental values. The same trend is observed electrochemically in the values of ΔE', and in the calculated Δ_{HLG} where for both Pt > Ni > Pd. Though the differences between complexes **1-3** described above small, it is clear that substitution

to the metal center in these donor-acceptor complexes results in clear and consistent changes to the energies of the frontier orbitals of these donor acceptor complexes.

3.3.2 Investigation of the Metal Influence.

Often (dithioloene)M(diimine) D-A complexes have significant metal d orbital character in their HOMOs, which is why the charge transfer in those complexes is often described as mixed metal-ligand-to-ligand charge transfer (MMLL$'$CT).[23,27] There is negligible contribution from the metal atoms in the catecholate centered HOMOs of complexes **1-3**, the MMLL$'$CT description does not seem to fit the (cat-tBu$_2$)M(bdi) complexes presented here with **1-3.** It is variations in the interactions between the metal atoms and the bdi ligand that provide an explanation for the observed trends. The bdi localized LUMOs displayed significant mixing from the metal d_{xz} orbitals, which arises from the anti-bonding combination of the metal dxx and the bdi π^* orbital and. The energy of the LUMOs are much more sensitive to the identity of the metal atom than the HOMOs. Qualitatively, the frontier molecular orbitals of **1-3** appeared nearly identical, in composition but MPA calculations offered insight into the underlying cause of the observed non-periodic trends found for these model complexes. The calculated and experimental measurements of ΔHL directly correlate to the amount of metal d_{xz} character in the LUMO (Pt > Ni > Pd).

The strength of the π-donating interaction, from the metal d_{xz} orbital to the bdi π^* orbital, that forms the LUMO in complexes **1-3** is a function of the amount of metal d orbital character in the orbital, as reflected by the magnitude of destabilization of the bdi π^* orbitals. Experimental evidence to support this hypothesis is founds in the electrochemical data. The first reduction of **2** was observed at a more positive potential than for complexes **1** and **3** .The positive shift in the reduction potential of indicates that the bdi ligand of complex **2** is more electron poor and is

therefore easier to reduce, due to a weaker π donation form the metal center. The metal effect on the frontier orbitals of these model complexes is different

An examination of the orbitals involved in the LL′CT using TD-DFT revealed another in the behavior of the palladium complex from the nickel and platinum derivatives. The LL′CT excitation energies provided by these calculations are nearly identical to the experimentally observed values. The calculated excitations were depicted as primarily catecholate→diimine charge transfer transitions. Complex **2** was the only member in the series for which the LL′CT originates exclusively from the HOMO→LUMO transition and is the only member of the series that can be described as exhibiting 'pure LL′CT'. Both complexes **1** and **3** show significant mixing from the HOMO–1→LUMO transition in the HOMO→LUMO, LL′CT transition. While both the HOMO and HOMO–1 orbitals of these complexes were largely located on the catecholate ligand the amount of metal character in these orbitals was significantly higher in the HOMO–1. This is especially pronounced in the nickel derivative in which the metal d_{yz} orbital makes up nearly half of the HOMO–1, while the platinum d_{xz} made up only a quarter of the HOMO–1 in the complex **3**. The HOMO–1(catecholate+d_{yz})→LUMO(diimine) character predicted in the primarily HOMO(catecholate)→LUMO(diimine) excitations of **1** and **3** suggests some amount of 'MMLL′CT' character, especially for complex **1**. Comparable calculations on group 10 dithiolene-diimine D-A complexes show greater metal d-orbital involvement in the HOMO, and therefore that LL′CT, than is observed with **1-3**. Relatively large metal d orbital contributions to the LUMO is common to nearly all D-A systems. This suggests that regardless of the metal character in the HOMO, the metal atom plays some role in the donor→acceptor charge transfer, and a more accurate description of the metals role in these D-A

65

complexes perhaps, metal-mediated ligand-to-ligand charge transfer is a more suitable definition of MMLL′CT.

In terms of metal ligand interactions, the palladium complex is an outlier and the nickel and platinum complexes are consistently very similar to each other. The small differences between the D-A properties show that metal serves more as a conduit through which the donor and accept ligands can communicate and the electrochemical and spectroscopic properties of these complexes are largely determined by the intrinsic properties of donor and acceptor ligands. Based on the finding presented in this chapter it is reasonable to conclude that no substantial reason exists for the use of the expensive second and third row Group 10 metals in D-A LL′CT dyes. Future chromophores built on these platforms should focus on nickel as the TM atom.

3.4 Summary

To the best of our knowledge, this report represents the first comprehensive examination of a catecholate-diimine donor-acceptor system incorporating the entire Group 10 series. Though the metal atom clearly is involved in the LL′CT, its effect is relatively minor. These results indicate that the extent of the metals influence on the properties of the D-A complexes is largely dictated by the degree of configuration interaction between the metal d orbitals and the diimine ligand π system. For this series of compounds palladium was consistently shown to have less metal-ligand interaction than both nickel and platinum. The previous chapter examining donor and acceptor ligand substitutions in (catecholate)Ni(diimine) complexes showed that ligand electronics play a much larger role in determining the spectroscopic and electrochemical properties of these D-A chromophores. This is significant in that it allows future work on molecular dyes based on this platform to focus on chromophores incorporating earth abundant

first-row metals without the need to overcome the significant performance decreases observed

with $M(bpy)_n$ MLCT dyes.

3.5 Experimental

General Methods. The complexes described below are air- and moisture-sensitive; therefore, manipulations were carried out under an inert atmosphere of argon or nitrogen using standard Schlenk, vacuum-line, and glovebox techniques. All reactions were carried out at ambient temperature (20–28 °C). Hydrocarbon solvents were sparged with argon then passed through activated alumina and Q5 columns to remove water and oxygen respectively. Ethereal and halogenated solvents were were sparged with argon, then dried by passage through two activated alumina columns. To test for water and oxygen removal, nonhalogenated solvents were treated with a drop of a solution of sodium benzophenone ketyl in THF. The ligand *mes*-BDI was prepared according to established procedures.[41] The metal precursers $(BDI)MCl_2$ (M = Pd, Pt) were prepared by a previously reported procedure.[42]

Physical Methods. NMR spectra were collected on Bruker Avance 500 MHz spectrometers in dry, degassed $CDCl_3$. ^{1}H NMR spectra were referenced to tetramethylsilane (TMS) using the residual proteo impurities of the solvent; ^{13}C NMR spectra were referenced to TMS using the natural abundance ^{13}C impurities of the solvent. All chemical shifts are reported using the standard à notation in parts per million; positive chemical shifts are to a higher frequency from the given reference. IR spectra were recorded as KBr pellets with a Perkin-Elmer Spectrum One FTIR spectro- photometer. Electronic absorption spectra were recorded with a Perkin-Elmer Lambda 800 UV-vis spectrophotometer. Perpendicular-mode X-band EPR spectra were collected using a Bruker EMX spectrometer equipped with an ER041XG microwave bridge.

Electrochemical Methods. Electrochemical Methods. Electrochemical experiments were performed on a Gamry Series G 300 potentiostat/galvanostat/ ZRA (Gamry Instruments, Warminster, PA) using a 3.0 mm glassy carbon working electrode, a platinum wire auxiliary electrode, and a silver wire reference electrode. Electrochemical experiments were performed at ambient temperature (20–24 °C), either in a nitrogen-filled glovebox or under an atmosphere of argon. Sample concentrations were 1.0 mM in THF with 0.10 M NBu4PF6 as the supporting electrolyte. All potentials are referenced to $[Cp_2Fe]^{+/0}$ using ferrocene or decamethylferrocene as an internal standard (–0.49 V vs $[Cp_2Fe]^{+/0}$). The typical solvent system window 2with our configuration was +1.0 V for the oxidation limit and –3.4 V for the reduction limit (vs $[Cp_2Fe]^{+/0}$). Decamethylferrocene (Acros) was purified by sublimation under reduced pressure and tetrabutylammonium hexafluorophosphate (Acros) was recrystallized from ethanol three times and dried under vacuum.

Synthesis of (cat-*t*Bu₂)Pd(bdi), 2. A slurry of $K_2[cat-tBu2]$, prepared from an Et_2O solution of $H_2[cat-tBu_2]$ (111.1 mg, 0.05 mmol, 1 equiv) and 2 equivalents of KO*t*Bu, was added to an Et_2O suspension of $(BDI)PdCl_2$. The reaction mixture was let stir 8 h, during which the solution had turned a dark green, then filtered to remove KCl. Solvent was removed from the filtrate and the resulting solid was redissolved in THF. The THF solution was concentrated to 5 mL under

vacuum, upon addiction of pentane (15 mL) and storage in a –35 ºC freezer over night, the product precipitated as a dark green microcrystalline solid. The mother liquor was reconcentrated and pentane (15 ml) was added and the mixture was stored at – 35 °C to yield a second crop of 2 and to give a final recrystallized yield of 217.3 mg (67% yield)

Anal. Calcd. (Found) for $C_{36}H_{48}N_2O_2Pd$: C, 66.81 (66.39); H, 7.48 (7.01); N, 4.33 (3.97). ^{1}H-NMR (500 MHz; CDCl3): δ 6.97 (s, 2H, aryl–H), 6.94 (s, 2H, aryl–H), 6.31 (d, J = 2.2 Hz, 1H, cat–H), 6.28 (d, J = 2.2 Hz, 1H, cat--H), 2.34 [s, 3H, p-Me], 2.34 [s, 3H, p-Me], 2.30 [s, 6H, o-Me], 2.27 [s, 6H, o-Me], 1.95 [s, 3H, N=CMe], 1.87 [s, 3H, N=CMe], 1.14 [s, 9H, tBu], 0.96 [s, 9H, tBu]. ^{13}C-NMR (126 MHz; CDCl$_3$): δ 171.2 (C=N), 170.5 (C=N), 163.3 (C–O), 159.0 (C–O), 141.5 (aryl–C), 141.3 (aryl–C), 137.9 (aryl– C), 137.18 (aryl–C), 137.07 (aryl– C), 134.6 (aryl– C), 129.41 (aryl–C), 129.21 (aryl– C), 129.08 (aryl– C), 128.93 (aryl– C), 111.5 (aryl– C), 110.5 (aryl– C), 34.25 (C(CH_3)$_3$), 34.10 (C(CH_3)$_3$), 32.2 (C(CH_3)$_3$), 29.3 (C(CH_3)$_3$), 21.25 (p–CH_3), 21.10 (p–CH_3), 18.33 (o–CH_3), 18.20 (o–CH_3), 17.89 (N=C– CH_3), 17.87 (N=C– CH_3). UV-vis-NIR [CH2Cl2; λ_{max}/nm (ε/M^{-1}cm^{-1})]: 288 (10732), 878 (4972).

Synthesis of (cat-tBu$_2$)Pt(bdi), 3. Complex **3** was prepared in a manner similar to that used for 8 with 77.8 mg of H$_2$(cat-tBu$_2$) (0.341 mmol, 1 equiv) and 2 equiv of KH, 200.0 mg of (BDI)PtCl$_2$ (0.341 mmol, 1 equiv) in THF. The dark green reaction mixture was concentrated and redissolved in Et$_2$O then filtered to remove KCl and a darkly colored solid byproduct. After washing these solids with a large amount of Et$_2$O the solvent was removed from the filtrate under vacuum. The resulting solid was redissolved in THF and the volume was concentrated to approximately 5 mL under reduced pressure. A solid was precipitated by the addition of pentane and storage at –35 ºC for 12 h. This solid was collected over a glass frit then washed with copious amounts of Et$_2$O until no color was observed in the washings. Upon removal of the Et$_2$O from the washings complex 3 was isolated as a blue solid (133.7 mg, 53% yield).

^{1}H-NMR (400 MHz; CDCl$_3$): δ 7.03 (s, 2H, aryl–H), 7.00 (s, 2H, aryl–H), 6.58 (d, J = 2.2 Hz, 1H, cat-H), 6.32 (d, J = 2.0 Hz, 1H, cat-H), 2.41 [s, 3H, p-Me, 2.39 [s, 3H, p-Me], 2.26 [s, 6H, o-Me], 2.23 [s, 6H, o-Me], 1.43 [s, 3H, N=CMe], 1.35 [s, 3H, N=CMe], 1.16 [s, 9H, tBu], 1.05 [s, 9H, tBu]. ^{13}-C NMR (126 MHz; CDCl$_3$): δ 170.3 (C=N), 169.6 (C=N), 163.2 (C–O), 159.4 (C–O), 143.1 (aryl–C), 142.8 (aryl–C), 138.6 (aryl–C), 137.30 (aryl–C), 137.17 (aryl–C), 134.8 (aryl–C), 130.24 (aryl–C), 130.16 (aryl–C), 129.3 (aryl–C), 128.9 (aryl–C), 111.15 (aryl–C), 111.11 (aryl–C), 34.4 (C(CH_3)$_3$), 34.1 (C(CH_3)$_3$), 32.2 (C(CH_3)$_3$), 29.3 (C(CH_3)$_3$), 21.1(p–CH_3), 17.85 (o–CH_3), 17.80 (N=C–CH_3), 17.72 (o–CH_3). UV-vis-NIR [CH$_2$Cl$_2$; λ_{max}/nm (ε/M^{-1}cm^{-1})]: 298 (6191), 344 (4960), 754 (9568).

Computational Methods: All calculations were performed using the TURBOMOLE program package. The geometric and electronic structures were optimized without symmetry constraints using the PBE functional[38-40] and a polarized triple-ζ basis set (TZVP).[40] All molecules were treated in the gas phase without accounting for solvent. The energy was converged to 10^{-7} Hartree. Mulliken population analyses [43] and plots were also obtained at the PBE/ TZVP level; the contour values were 0.03 for the molecular orbital plots.

Crystallographic Methods. X-ray diffraction data were collected on crystals mounted on glass fibers using a Bruker CCD platform diffractometer equipped with a CCD detector. Measurements were carried out at 93 or 163 K using Mo Kα (λ = 0.710 73 Å) radiation, which was wavelength-selected with a single-crystal graphite monochromator. The SMART program package was used to determine unit-cell parameters and to collect data. The raw frame data were processed using SAINT and SADABS to yield the reflection data files. Subsequent calculations were carried out using the SHELXTL program suite. Structures were solved by direct methods

and refined on F^2 by full-matrix least-squares techniques. Analytical scattering factors for neutral atoms were used throughout the analyses. Hydrogen atoms were included using a riding model. ORTEP diagrams were generated using ORTEP-3 for Windows.

3.6 References

1.   Hagfeldt, A.; Boschloo, G.; Sun, L.; Kloo, L.; Pettersson, H. *Chem Rev* **2010**, *110*, 6595.
2.   Meyer, T. J. *Accounts Chem Res* **1989**, *22*, 163.
3.   Campagna, S.; Puntoriero, F.; Nastasi, F.; Bergamini, G.; Balzani, V. In *link.springer.com*; Topics in Current Chemistry; Springer Berlin Heidelberg: Berlin, Heidelberg, 2007; Vol. 280, pp. 117–214.
4.   Juris, A.; Balzani, V.; Barigelletti, F.; Campagna, S.; Belser, P.; Zelewsky, von, A. *Coordination Chemistry Reviews* **1988**, *84*, 85.
5.   Endicott, J. F.; Schlegel, H. B.; Uddin, M. J.; Seniveratne, D. S. *Coordination Chemistry Reviews* **2002**, *229*, 95.
6.   Amouyal, E.; Bahout, M.; Calzaferri, G. *J. Phys. Chem.* **1991**, *95*, 7641.
7.   Johansson, E. M. J.; Odelius, M.; Plogmaker, S.; Gorgoi, M.; Svensson, S.; Siegbahn, H.; Rensmo, H. *J. Phys. Chem. C* **2010**, *114*, 10314.
8.   Creutz, C.; Chou, M.; Netzel, T. L.; Okumura, M.; Sutin, N. *J. Am. Chem. Soc.* **1980**, *102*, 1309.
9.   Wadman, S. H.; Geer, E. P. L. V. D.; Havenith, R. W. A.; Gebbink, R. J. M. K.; Klink, G. P. M. V.; Koten, G. V. *Journal of Organometallic Chemistry* **2008**, *693*, 3188.
10.   Zhou, X.; Ren, A.-M.; Feng, J.-K. *Journal of Organometallic Chemistry* **2005**, *690*, 338.
11.   Ferguson, J.; Herren, F. *Chemical Physics Letters* **1982**, *89*, 371.
12.   Johnson, P. S.; Cook, P. L.; Zegkinoglou, I.; García-Lastra, J. M.; Rubio, A.; Ruther, R. E.; Hamers, R. J.; Himpsel, F. J. *J. Chem. Phys.* **2013**, *138*, 044709.
13.   McCusker, J. K.; Walda, K. N.; Dunn, R. C.; Simon, J. D.; Magde, D.; Hendrickson, D. N. *J. Am. Chem. Soc.* **1993**, *115*, 298.
14.   McCusker, J. K. *Accounts Chem Res* **2003**, *36*, 876.
15.   Ferrere, S. *Chem. Mater* **2000**, *12*, 1083.
16.   Ferrere, S. *Inorganica Chimica Acta* **2002**, *329*, 79.
17.   Ferrere, S.; Gregg, B. A. *J Am Chem Soc* **1998**, *120*, 843.
18.   Cummings, S.; Eisenberg, R. *J Am Chem Soc* **1996**, *118*, 1949.
19.   Linfoot, C. L.; Richardson, P.; McCall, K. L.; Durrant, J. R.; Morandeira, A.; Robertson, N. *Solar Energy* **2011**, *85*, 1195.
20.   Archer, S.; Weinstein, J. A. *Coordination Chemistry Reviews* **2012**, *256*, 2530.
21.   Cummings, S. D.; Cheng, L.-T.; Eisenberg, R. *Chem. Mater* **1997**, *9*, 440.
22.   Fox, G. *Inorg Chem* **1992**.
23.   Mitsopoulou, C. A. 2010; Vol. 254, pp. 1448–1456.
24.   Makedonas, C.; Mitsopoulou, C.; Lahoz, F.; Balana, A. *Inorg Chem* **2003**, *42*, 8853.
25.   Pilia, L.; Espa, D.; Barsella, A.; Fort, A.; Makedonas, C.; Marchiò, L.; Mercuri, M. L.; Serpe, A.; Mitsopoulou, C. A.; Deplano, P. *Inorg Chem* **2011**, *50*, 10015.
26.   Espa, D.; Pilia, L.; Makedonas, C.; Marchiò, L.; Mercuri, M. L.; Serpe, A.; Barsella, A.; Fort, A.; Mitsopoulou, C. A.; Deplano, P. *Inorg Chem* **2014**, ASAP.

27.   Cocker, T.; Bachman, R. *Inorg Chem* **2001**, *40*, 1550.
28.   Anbalagan, V.; Srivastava, T. *Polyhedron* **2004**, *23*, 3173.
29.   Deibel, N.; Schweinfurth, D.; Fiedler, J.; Záliš, S.; Sarkar, B. *Dalton Trans*. **2011**, *40*, 9925.
30.   Benedix, R.; Hennig, H. *Inorganica Chimica Acta* **1988**, *141*, 21.
31.   Carugo, O.; Djinovi, K.; Rizzi, M.; Castellani, C. B. *J. Chem. Soc., Dalton Trans*. **1991**, 1551.
32.   Bill, E.; Bothe, E.; Chaudhuri, P.; Chlopek, K.; Herebian, D.; Kokatam, S.; Ray, K.; Weyhermüller, T.; Neese, F.; Wieghardt, K. *Chemistry–A European Journal* **2005**, *11*, 204.
33.   Chlopek, K.; Bothe, E.; Neese, F.; Weyhermuller, T.; Wieghardt, K. *Inorg Chem* **2006**, *45*, 6298.
34.   Cope-Eatough, E.; Mair, F.; Pritchard, R.; Warren, J.; Woods, R. *Polyhedron* **2003**, *22*, 1447.
35.   Best, J.; Sazanovich, I. V.; Adams, H.; Bennett, R. D.; Davies, E. S.; Meijer, A. J. H. M.; Towrie, M.; Tikhomirov, S. A.; Bouganov, O. V.; Ward, M. D.; Weinstein, J. A. *Inorg Chem* **2010**, *49*, 10041.
36.   Adams, C. J.; Fey, N.; Parfitt, M.; Pope, S. J. A.; Weinstein, J. A. *Dalton Trans*. **2007**, 4446.
37.   Oblad, P. F.; Bercaw, J. E.; Hazari, N.; Labinger, J. A. *Organometallics* **2010**, *29*, 789.
38.   Perdew, J. P.; Burke, K.; Ernzerhof, M. *Phys. Rev. Lett*. **1996**, *77*, 3865.
39.   Perdew, J. P.; Burke, K.; Ernzerhof, M. *Phys. Rev. Lett*. **1997**, *78*, 1396.
40.   Weigend, F.; Ahlrichs, R. *Phys. Chem. Chem. Phys*. **2005**, *7*, 3297.
41.   Zhong, H. A.; Labinger, J. A.; Bercaw, J. E. *J Am Chem Soc* **2002**, *124*, 1378.
42.   van Asselt, R.; Elsevier, C. J.; Amatore, C.; Jutand, A. *Organometallics* **1997**, *16*, 317.
43.   Mulliken, R. S. *J. Chem. Phys*. **1955**, *23*, 1833.

Chapter 4
Metal-Donor Interactions: The Role of the Chalcogen

4.1 Introduction

It has been well established that (dithiolene)M(diimine) ligand-to-ligand charger transfer (LL′CT) donor-acceptor (D-A) chromophores show significant metal d orbital character in the primarily dithiolene-localized HOMOs.[1,2] Investigations into the influence of the metal atom on the D-A properties of catecholate-diimine complexes presented in Chapter 3 revealed practically no metal character in the catecholate-localized HOMOs. In these complexes metal-diimine π interactions accounted for the entirety of the small differences that were seen upon substitution of the metal atom. For dithiolene D-A LL′CT complexes, the role of the metal atom in the charge transfer absorptions is exemplified by the fact that the term mixed metal-ligand-to-ligand charge transfer is often used instead of simply LL′CT.[3,4] Given that metal-donor π interactions are the cause of the metal-donor orbital mixing, one might expect that substitution of sulfur for selenium as the donor ligand chalcogen might increase the strength of these metal-donor π interactions (at least with second and third row transition metals) and an increased role for the metal atom in determining the spectroscopic and electrochemical properties D-A LL′CT complexes with selenium based donors. There are only a few examples of heteroleptic D-A LL′CT complexes with diselenolene donor ligands in the literature.[5-7] Interestingly, for the diselenolene D-A complexes that have direct dithiolene analogues show only slight differences in D-A behavior was observed between the ditholene and diselenolene complexes is observed.

There has yet to be a combined experimental and computational investigation into the effect of donor ligand chalcogen identity of the on metal contribution in the HOMO and LUMO of D-A LL′CT complexes or whether this would effect the metal ions influence over D-A behavior changes with the identity of the donor chalcogen heteroatoms. Toward this end we have prepared (donor)M(bdi) model complexes using the donor ligands 1,2-benzenedithiol (bdt) and

1,2-benzenediselenol (bds). Three new compounds of the formula (bdt)M(bdi) [bdi = N,N′-bis(2,4,6-trimethylphenyl)–2,3-butanediimine; M = Ni(II), **1a**; Pd(II), **1b**, and Pt(II), **1c**], along with the (bds)Pt(bdi) (**2c**) have been prepare and characterized by UV-vis-NIR absorption spectroscopy and electrochemical methods. Additionally, a detailed DFT and TD-DFT study, has been conducted for **1a-c** as well for **2c** and its the nickel (**2a**) and palladium (**2b**) analogues. The D-A complexes **1a-c** displayed a significantly smaller metal influence on the spectroscopic and electrochemical properties than was observed for the (cat-tBu$_2$)M(bdi) complexes detailed in Chapter 3 [(cat-tBu$_2$)$^{2-}$ = 3,5 di-$tert$-butylcatecholate M = Ni(II), **3.1**; Pd(II), **3.2**, and Pt(II), **3.3**]. Substitution of bdt for bds caused virtually no discernible change in the UV-vis absorption spectrum or cyclic voltammogram of **2c** form to **1c**. This finding was supported by DFT calculations for **1a-c** and **2a-c** which showed that substitution bds for bdt had little effect on the frontier orbitals responsible for D-A behavior.

4.2 Results

4.2.1 Synthesis and characterization of bdt and bds complexes.

Dithiolene-diimine D-A complexes are generally prepared under fairly harsh conditions in protic or very polar solvents, like MeOH or DMSO, with strong bases, under heat or reflux. [1,8-10] The (bdt)M(bdi) D-A LL′CT complexes were prepared using much milder conditions in non-protic solvents (THF or DCM) with mild amine bases (NEt$_3$ or H$_2$NtBu) at room temperature taking advantage of the chelate-effect and the formation of insoluble ammonium chloride salts (HNEt$_3$Cl in THF or H$_3$NtBuCl in DCM) to drive the reaction to completion. Treatment of a slurry of the (bdi)MCl$_2$ precursor with one equivalent of bdt in the presence of 2.2 equivalents of the amine base, as shown in Scheme 1, resulted in the rapid development of a dark blue-green color in the reaction mixture. After removal of the resulting insoluble ammonium

salts the desired D-A complexes were precipitated from the filtrate by the addition of pentane and cooling at –35 °C. Complexes **1a-c** were isolated as intensely colored solids in high yields (77 - 85 %). The ^{1}H NMR spectra of each (bdt)M(bdi) complexe indicate that a C_2 symmetric structure is adopted in solution.

Scheme 4.1. Synthesis of complexes **1a-c**.

$$M = \text{Ni (1a), Pd (1b), Pt (1c)}$$
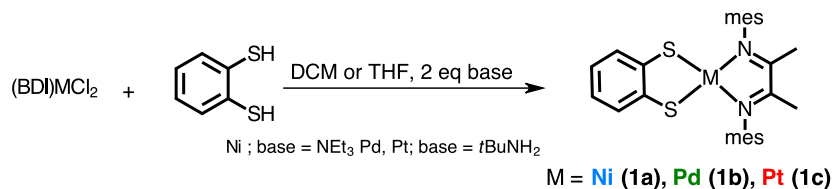
The diselenolene complex (bds)Pt(bdi), **2c**, was synthesized using a modified procedure for the preparation of the (bds)$^{2-}$ monomer from the oligomeric (bds)$_n$.[5]Addition of excess (bds)$^{2-}$ monomer dissolved in THF to a slurry of (bdi)PtCl$_2$ (Scheme 2) immediately caused in the development of a dark blue solution indicating the formation of **2c**. Complex **2c**, was obtained as a dark-blue solid in 60% yield after recrystallization from DCM and pentane. The ^{1}H and NMR spectra of **2c** displayed resonances in accordance with a C_2 symmetric species in solution. Unfortunately this synthesis could not be extended to the other Group 10 (bds)M(bdi) complexes (M = Ni, Pd), nor could they be obtained using an alternative method to prepare the (bds)$^{2-}$ monomer.[11,12]Initial attempts at the synthesis of (bds)Ni(bdi) gave promising results, but pure samples of this complex could not be obtained at the time of this report. All the attempts to isolate (bds)Pd(bdi) were unsuccessful which is unsurprising given the rarity of heteroleptic palladium-diselenolene complexes in the literature. [6,11]
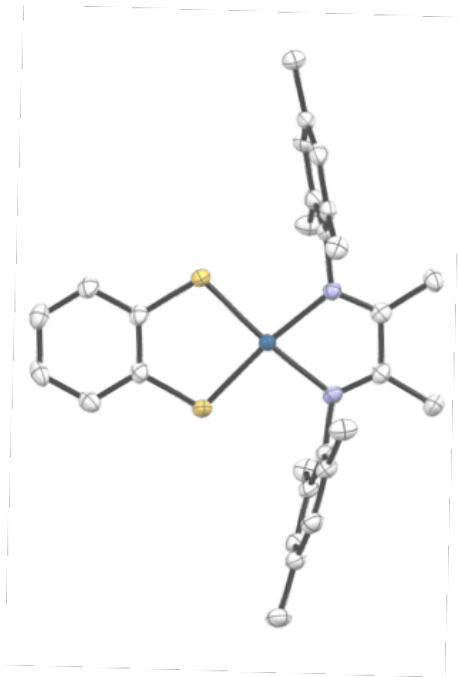
Scheme 4.2. Synthesis of complex **2c**, (bds)²⁻ was prepared according to a previously published procedure.[5]
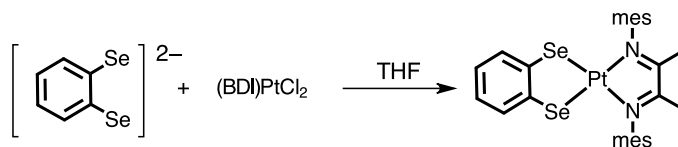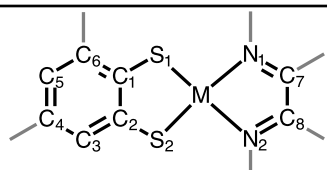
4.2.2 Structural Characterization of (bds)M(bdi) complexes.

Single crystal X-ray diffraction studies carried out for complexes **1a** and **1c** confirmed that they exist as the desired (bdt)M(bdi) complexes in the solid state. The X-ray structure of **1c**, shown in Figure 4.2, and selected bond distances for **1a** and **1c** are shown in Table 1. The molecular geometries of the two complexes are very similar. Each displays a square-planar geometry around the metal center with a slight puckering of the bdt ligand. The plane C_6 ring of the ligand formed a 6.43° and 5.42° angle with the MN2S2 mean plane, for **1a** and **1c** respectively. The M–S and M–N bond lengths of complexes **1a** and **1c** are in good agreement with previously reported (dithiolene)M(diimine) complexes,[1,2,8,13-15] The M-N bonds are slightly longer (M–N **1a** = 1.90 Å; **1c** = 2.02 Å) than was observed for their catecholate analogues in Chapter 3 (M–N **3.1** = 1.87, 1.86 Å; **3.3** = 1.97 Å), this is likely caused by differences in trans influence between the dithiolene and catecholate donor ligands. Intra-ligand bond distances of the bdi in **1a** and **1c** show C–N and C–C bonds consistent with a C-N double bond and a C-C single bond, respectively, indicating the ligands are in the diimine oxidation state.[16-18] The observed C–S bond distances for both complexes are consistent with other fully reduced dithiolene ligands (1.74 - 1.78 Å).[1,2,8,14,19] These data confirm that both ligands and the metal ions are in the expected oxidation states for complexes **1a** and **1c**.

Table 4.1 Selected bond distances (Å) for donor-acceptor complexes **1a** and **1c**.

	Bond Distances / Å	
	1a	**3a**
M–S	2.1340(5)	2.2428(10)
M–S	2.1378(5)	2.2490(9)
M–N	1.9020(14)	2.013(3)
M–N	1.9045(14)	2.027(3)
S_1	1.7495(18)	1.752(4)
S_2	1.7455(18)	1.748(4)
C	1.395(2)	1.394(5)
C	1.397(2)	1.407(6)
C	1.383(3)	1.383(6)
C	1.392(3)	1.387(6)
C	1.382(3)	1.378(6)
C	1.398(2)	1.398(5)
N	1.297(2)	1.294(5)
N	1.301(2)	1.306(5)
C	1.472(2)	1.468(5)

Figure 4.2 ORTEP diagram of (bds)Pt(bdi), **3**. Ellipsoids are drawn at 50% probability. Hydrogen atoms have been omitted for clarity.

4.2.3 Absorption spectroscopy of (donor)M(bdi) D-A complexes.
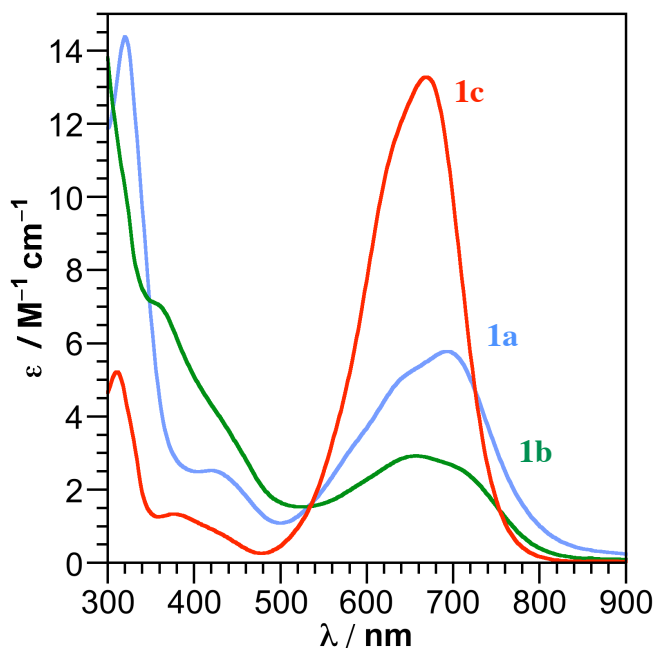
Figure 4.3. UV-vis-NIR absorption spectra of complexes **1a**, **1b** and **1c** in DCM solution at 298 K.

The intense charge transfer absorptions characteristic of D-A LL′CT dyes were observed in the absorption spectra of the (bdt)M(bdi) complexes. UV-vis-NIR spectra of **1a-c** collected in DCM solution are shown in Figure 4.3. Absorption maxima, and E_{CT} data of **1a-c** are given in Table 4.2. The absorption maxima of the complexes **1a-c** differ by no more than 35 nm. The LL ′CT absorption manifolds of **1a-c** exhibit fine-structure characteristic of vibronic coupling. The apparent changes in the dominant vibronic level (e.g. ν_0–ν_0' vs. ν_0–ν_1') made a comparison of the energy of the LL′CT transition using λ_{max} uninformative. To avoid uncertainty E_{CT} (estimated as described in Chapter 2) was chosen as a more accurate estimate of the excited state energy. Based on this metric complex **1c** displayed the highest energy LL′CT transition followed by **1a** and **1b**. The extinction coefficients of the LL′CT excitations are more dependent on the identity of the metal center and increased in the order Pd < Ni < Pt.

Table 4.2. Absorption data in dichloromethane solution and of **1a-c** and **2c**.

	Abs. λ_{max}	estimated E_{es}	ε / M
1a	692 (1.79)	1.56	5700
1b	658 (1.88)	1.55	2900
1c	670 (1.85)	1.66	13300
2c	664 (1.87)	1.67	18100

The UV-vis absorption spectrum of (bds)Pt(bdi), **2c**, in DCM solution is shown, with that of **1c,** in Figure 4.4. Complex **2c** also displayed a strong charge transfer band with an absorption maxima at 664 nm (1.87 eV). Aside from the large increase in the extinction coefficient, the absorption spectra of **2c** was nearly identical to the spectra collected for the bdt analogue **1c**. This is similar to results reported by Bachman and coworkers who found that the LL′CT absorptions of (bdt)Pt(bpy) and (bds)Pt(bpy) occur at virtually the same energy with λ_{max} of 598 (2.07 eV) nm and 590 nm (2.10 eV), respectively.[5]
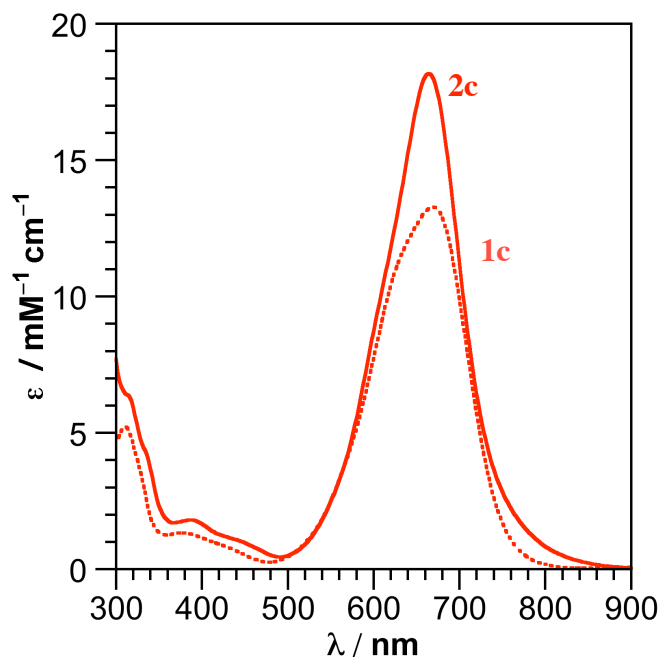
Figure 4.4. UV-vis-NIR absorption spectra of complexes **1c** (̈) and **2c** (—) in DCM solution at 298 K.

4.2.4 Electrochemistry of (donor)M(bdi) complexes.

To further probe the frontier molecular orbitals of the Group 10 D-A LL′CT complexes, electrochemical experiments were performed for each member of the series. Cyclic voltammograms obtained for **1a-c** and **2c** in THF solution are shown in Figure 4.5 and Table 4.3 contains redox potential data for **1a-c** and **2c**, which were collected using differential pulse voltammetry to obtain accurate potentials for the non reversible redox events. Each complex displayed two diimine localized one-electron reduction processes. In all cases the first reductive event ($E^{-/0}$) are completely reversible. The second reductions of **1a**, **1c** and **2c** are reversible, but is only partially reversible for **1b**. The first oxidative event ($E^{0/+}$) displayed by each complex was irreversible. Complex **1c**, shows a second, more reversible oxidative process not observed for the other complexes. This second oxidation did not appear to be a byproduct of the first oxidation, as the ratio between the currents of the anodic and cathodic waves did not change upon varying

scan rates. The potentials of $E^{0/-}$ in the bdt series showed slight differences depending on the identity of the metal center. The nickel complex, **1a**, displays the most negative $E^{0/-}$ followed by the platinum. The palladium complex (**1b**), as with the catecholate complex of Chapter 3, displays the most motive potential for $E^{0/-}$. The first oxidation for this series was most positive for **1c** and shifted less positive for **1a** and **1b**. For the bds complex **2c**, both $E^{+/0}$ and $E^{0/-}$ are shifted approximately 100 mV more negative than in **1c**.
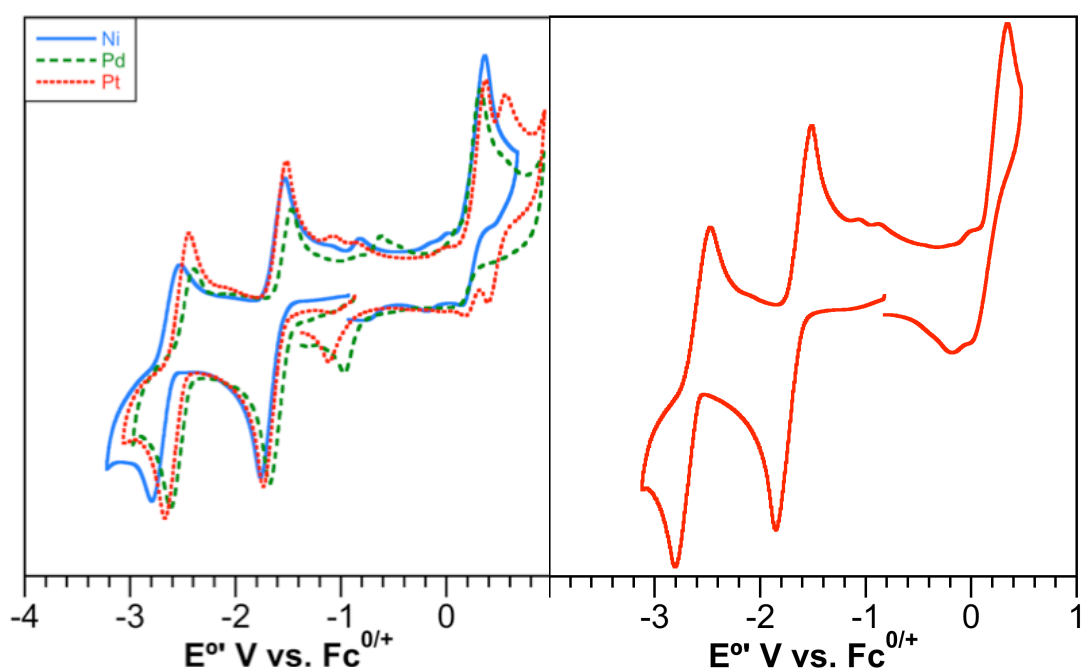
Figure 4.5. (A) Cyclic voltammetry plots for complexes **1a** (blue), **1b** (green) and **1c** (red). **(B)** Cyclic voltammetry plot for complexes **2c.** Data were collected at 298 K in THF solutions that were 1.0 mM in analyte and 0.1 M in [Bu$_4$N][PF$_6$] electrolyte using a glassy carbon working electrode. All potentials were referenced to [Cp$_2$Fe]$^{+/0}$ using an internal standard.

The difference in potential between the first oxidation and first reduction ($\Delta E = E^{+/0} - E^{0/-}$) is an electrochemical estimate of the HOMO-LUMO gap (ΔHL). Complexes **1a-c** displayed ΔE values differing by only a total of 120 mV across the entire series. The nickel (**1a**) and platinum (**1c**) complexes displayed the nearly identical values of ΔE, 1.86 V and 1.85 V respectively, while ΔE of the palladium derivative, **1b**, was slightly smaller at 1.74 V. Complex

2c displayed ΔE = 1.83 V which, as was observed with the absorption spectrum, was nearly identical to **1c**.

Table 4.3. Reduction potentials and ΔE of complexes **1a-c** and **2c**.

	$E°$				
	E	E	E	E	ΔE
1a	0.88	0.22	−1.65	-2.69	1.86
1b	—	0.18	−1.56	-2.52	1.74
1c	0.46	0.25	−1.60	-2.54	1.85
2c	0.62	0.12	-1.71	-2.61	1.83

4.2.3 Computational Analysis.

Density functional theory (DFT) analysis of the (bdt)M(bdi) complexes was performed in an effort to better understand the electronic structure of these D-A LL′CT complexes. All calculations described in this chapter were performed using the PBE functional[20,21] with the triple-ζ basis set TZVP.[22] The optimized molecular structures obtained for complexes **1a** and **1c** are in good agreement with the X-ray crystal structures and all calculated bond lengths are within 0.03 Å of the experimental values. Given the good agreement found for the molecular structures, calculations on the ground state (GS) electronic structures of **1a-c** were carried out.

The molecular orbital (MO) diagrams obtained from these calculations are shown in Figure 4.5a and the HOMO–1, HOMO and LUMO Kohn-Sham (KS) orbitals are shown in Figure 4.5c for each member of the series. The highest occupied orbitals of the (bdt)M(bdi) donor-acceptor complexes were different depending on the identity of the metal center. For (bdt)Ni(bdi), the HOMO was is an orbital with π^* character between the metal d_{yz} and the sulfur p_z orbitals of the dithiolene, while the HOMO–1 originates from the bdt π system, or the 'donor-

HOMO' orbital. For complex **1a** the calculated energies of the HOMO and HOMO–1 are virtually identical at –4.406 eV and –4.409 eV, respectively. Alternatively for complexes **1b** and **1c**, the HOMOs are the dithiolene centered 'donor-HOMO' orbitals and the M-bdt π^* orbital, which is the HOMO in **1a**, represented HOMO–1. The LUMOs of each complex are very similar in composition and were primarily localized on the diimine ligand with some mixing from the metal d_{xz} orbital. Mulliken population analysis (MPA) provides the composition of the frontier MOs in terms of percent contribution to each orbital from the dithiolene, the diimine and metal atom. Table 4.5 lists the energies, contributions of the metal, donor and diimine for the HOMO–1, HOMO, and LUMO of the complexes **1a-c**. This analysis showed that for each of complexes **1a-c** the LUMO is primarily bdi acceptor ligand in character with some contribution from the metal d_{xz} and the donor ligand. The contribution to the LUMO from the metal is variable depending on the identity of the metal atom with metal contribution increasing in the order Ni > Pt > Pd. Population analysis of the HOMO–1 and HOMOs of **1a-c** showed that both orbitals are mostly centered on the dithiolene. The 'donor-HOMO' orbitals of each complex showed significant contributions from metal d_{xz} and bdi centered orbitals. Metal character in both the 'donor-HOMO' and the M-bdt π^* orbitals vary with the metal identity and percentage d_{xz} Ni > Pt > Pd. The M-donor π^* orbitals expectedly displayed more metal d orbital contribution than the 'donor-HOMO'.
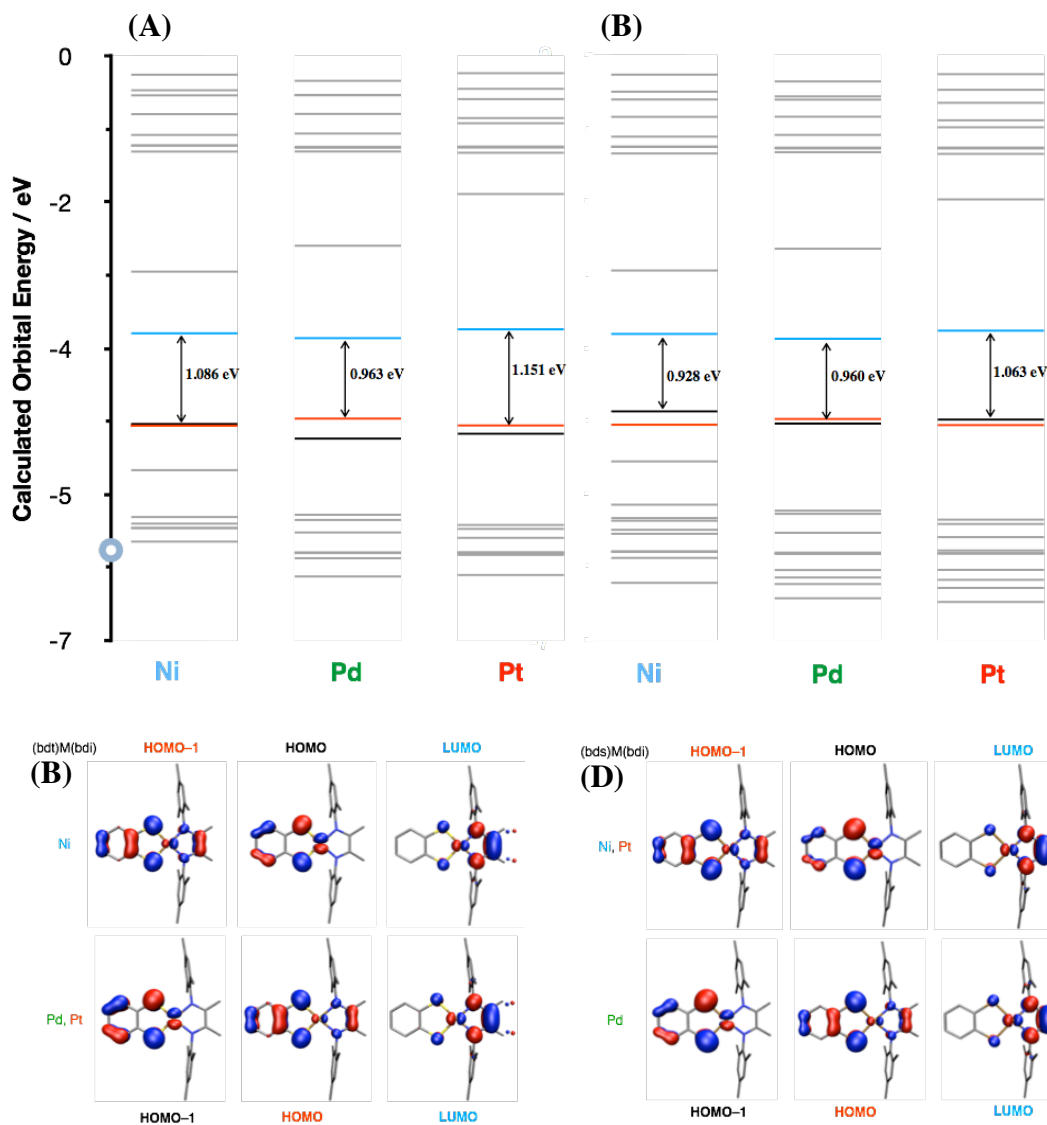
Figure 4.6. (A): Calculated MO diagram and ΔHL for **1a-c** (right) and **2a-c** (left). (B) Calculated KS orbitals of **1a** and **1b** (also representative for **1c**) (left) and **2a** (also representative for **2c**) and **2b** (right) involved in the LL′CT excitations.

Calculations were also performed for the (bds)M(bdi) series model complexes. Although no crystallographic data was available with which to compare the calculated structures of **2a-c**, the predicted bond lengths were consistent with previously reported (bds)ML and L′M(bdi) complexes.[5,6,11,23] The calculated MO diagrams for **2a-c** are shown in Figure 4.5c and the KS orbitals are shown in Figure 4.5d. The frontier MOs of theses complexes are very similar in

composition to their bdt analogues. The HOMOs of the nickel and platinum diselenolene complexes are the M-donor π^* orbitals and the 'donor-HOMO' orbitals are the HOMO–1s. For the palladium derivative the 'donor-HOMO' stayed higher in energy than the M-donor π^* orbital. Again, for complexes **2a-c** the LUMO was shown to be primarily bdi based. The energies, and contributions of the metal, donor and diimine for the HOMO–1, HOMO, and LUMO of the (bds)M(bdi) D-A complexes are given in Table 4.5. The metal contributions to the frontier orbitals of **2a-c** depend on the identity of the metal atom and follow the same trends as their dithiolene analogues. In both donor centered orbitals the contribution observed from the selenide heteroatom of the bds increased significantly from the contribution form the sulfur atom of the bdt ligand in **1a-c**.

Even though in **2a** and **2c** the 'donor-HOMO' is not the overall HOMO in the complex the donor-acceptor behavior remains exclusively between the 'donor-HOMO' and the diimine-centered LUMO. Additionally, because the bds-M π^* is the HOMO in **2a** and **2c**, the ΔHL does not accurately predict the D-A properties of these two complexes and complex **2c** (1.06 eV) shows a smaller HOMO-LUMO gap than **1c** (1.15 eV) even though, experimentally, the two complexes were almost indistinguishable. For these complexes, the difference between the 'donor-HOMO' and the LUMO, ΔDA, is a more informative metric, and ΔDA for **1c** (1.15 eV) and **2c** (1.13 eV) differ by only 20 meV which is much closer to what is observed experimentally. Also, the ΔDAs of **2a** and **2c** match the ΔHLs of **1a** and **1c** almost exactly.

Table 4.5. Calculated energy and MPA orbital composition of the HOMO–1, HOMO and LUMO for complexes **1a-c** and **2a-c**. 'donor-HOMO' (red), M-donor π* (black) and LUMO (blue).

| | M | Orbital | E / eV | ΔDA / eV | % Composition | | | |
					M	donor	acceptor	E (S, Se)
(bdt)M(bdi)	Ni	HOMO–1	–4.41		10.1	68.6	21.3	38.3
		HOMO	–4.41	1.09	39.9	58.7	1.3	37.4
		LUMO	–3.32		14.1	17.4	68.4	12.4
	Pd	HOMO–1	–4.58		17.4	83.2	0.0	50.2
		HOMO	–4.34	0.96	7.9	72.7	19.4	41.9
		LUMO	–3.38		10.3	18.2	71.5	13.2
	Pt	HOMO–1	–4.52		22.3	77.2	3.0	47.7
		HOMO	–4.42	1.15	8.4	67.9	24.1	38.6
		LUMO	–3.27		13.4	21.3	65.4	16
(bds)M(bdi)	Ni	HOMO–1	–4.42		10.3	69.3	20.4	44.4
		HOMO:	–4.26	1.08	36.0	62.9	1.1	46.4
		LUMO:	–3.34		14.9	15.5	69.6	12.8
	Pd	HOMO–1	–4.41		15.3	84.7	0.0	61.4
		HOMO:	–4.35	0.96	7.5	74.1	18.3	48.8
		LUMO:	–3.39		10.4	16.4	73.2	13.6
	Pt	HOMO–1	–4.43		8.0	69.2	22.7	45.1
		HOMO:	–4.36	1.13	19.6	78.9	1.4	57.4
		LUMO:	–3.30		13.5	19.8	66.7	16.8

TD-DFT calculations, performed at the PBE/TZVP level of theory, were conducted for the (bdt)M(bdi) series in the gas phase to determine which molecular orbitals are involved in the LL′CT. The first 40 singlet excitations calculated for complexes **1a-c** and **2c** plotted vs oscillator strength are shown with their UV-vis-NIR absorption spectra in Figure 4.7. The calculated energy, oscillator strengths and orbital contributions of the LL′CT excitations for each D-A complex are tabulated in Table 4.6. The calculated LL′CT excitations of **1a-c** were in good agreement with the experimental value. The largest discrepancy from the experimental LL′CT energy was observed for (bdt)Pd(bdi) which was underestimated by 0.28 meV. The low-energy excitations of **1b** and **1c** with the highest oscillator strength were determined to be exclusively HOMO→LUMO transitions, and the LL′CT excitation of **1a** was HOMO–1→LUMO. The

oscillator strength calculated for the HOMO→LUMO transition of (bdt)Ni(bdi) is two orders of magnitude smaller than the HOMO–1→LUMO transition. The low-energy excitation with the highest oscillator strength calculated for (bds)Pt(bdi) was calculated with an energy 1.79 eV and was in good agreement with the observed LL′CT absorption (1.87 eV). Calculated energies of the transitions for the nickel and palladium derivates were 1.66 and 1.55 eV respectively. For **2a** and **2c** these excitations occurred from HOMO–1→LUMO while for **2b** the transition was from HOMO→LUMO. These data for model complexes **2a** and **2b** agree with the trends found in the calculated and experimental data of the dithiolene D-A complexes.
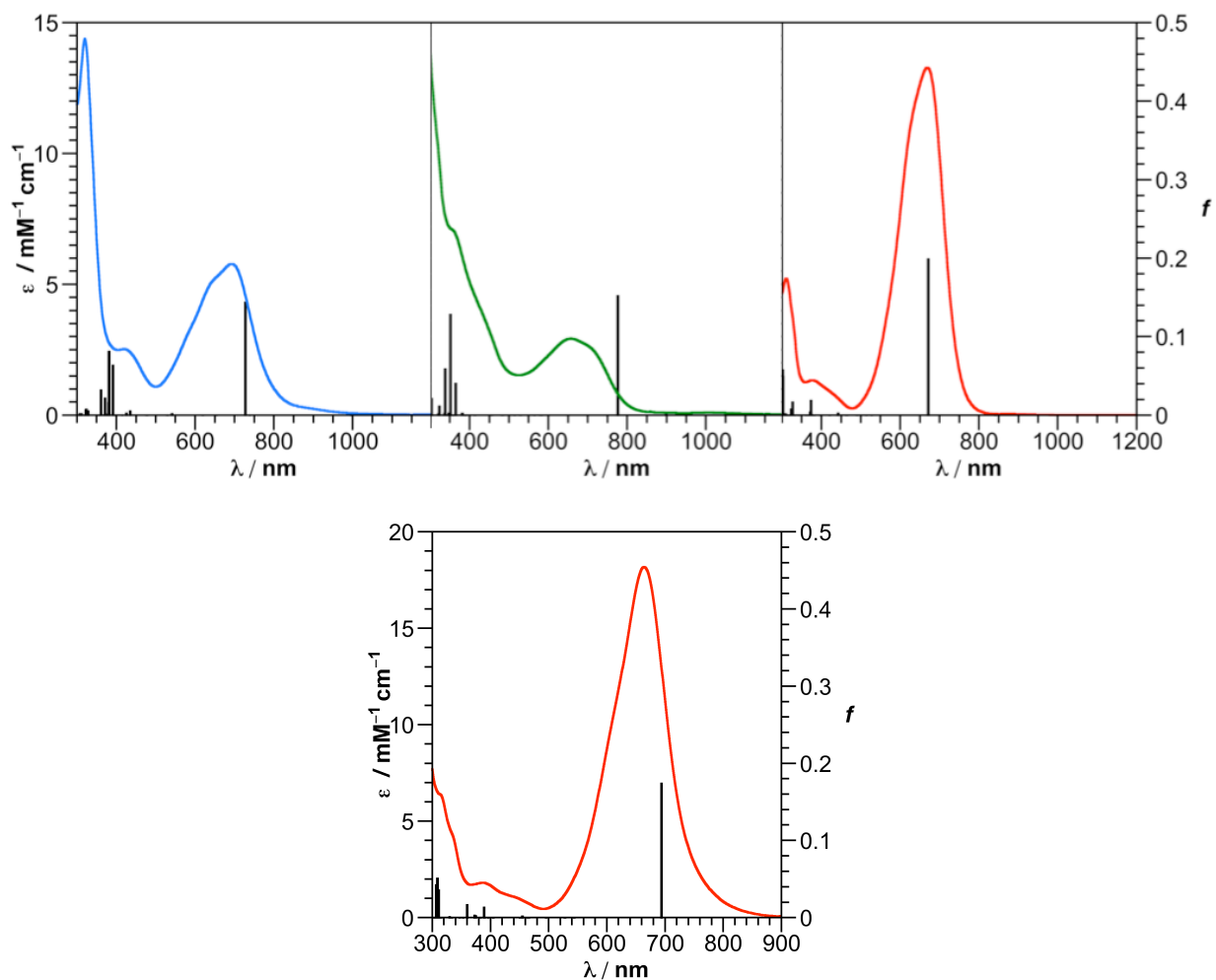
Figure 4.7. Calculated excitations of **1a-c** and **2c** vs. f with experimentally obtained UV-vis-NIR spectra. (**top**) **1a** (blue), **1b** (green), **1c** (red). (**bottom**) **2c**.

Table 4.6. Calculated and Experimental LL′CT absorptions for **1a-c** and **2a-c**.

	M	ELL′CT / eV calc.	ELL′CT / eV obs.	f	Orbital Composition
(bdt)M(bdi)	Ni	1.71	1.79	0.14	HOMO–1 → LUMO (92.3%)
	Pd	1.6	1.88	0.15	HOMO → LUMO (95.8%)
	Pt	1.85	1.85	0.2	HOMO → LUMO (95.6%)
(bds)M(bdi)	Ni	1.66	—	0.13	HOMO–1 → LUMO (91.4%)
	Pd	1.55	—	0.13	HOMO → LUMO (95.6%)
	Pt	1.79	1.87	0.18	HOMO–1 → LUMO (95.4%)

4.3 Discussion

4.3.1 Effects of the Chalcogen on Donor-Acceptor Behavior.

Dithiolene and diselenolene donor ligands were incorporated into our Group 10 (donor)M(bdi) model platform to study the relationship between donor ligand chalcogen heteroatoms and transition metal center. New, mild conditions were employed for preparation of (bdt)M(bdi) complexes (**1a-c**) that produced the desired D-A LL′CT chromophores high yields and purity. The D-A complex (bds)Pt(bdi), was the only diselenolene complex that could be prepared for this report. This is not surprising given the rarity of heteroleptic diselenolene complexes in the literature however, to supplement the experimental findings, detailed DFT and TD-DFT computational studies on were conducted for both (donor)M(bdi) sets on the entire Group 10 series (nickel, palladium and platinum). These calculations in combination with the results obtained for the (cat-tBu$_2$)M(bdi) complexes from Chapter 3, provide new insight into how donor-metal interactions effect D-A behavior which have not previously been investigated to this extent.

Substitution of oxygen for sulfur as the chalcogen atom in the donor ligand resulted in significant changes to the D-A behavior displayed by the (bdt)M(bdi) complexes compared to the catecholate complexes from Chapter 3. LL′CT absorptions of complexes **1a-c** are blue-shifted by as much as 220 nm, from their (cat-*t*Bu$_2$)M(bdi) analogues. Electrochemical measurements for **1a-c** were in good agreement with the absorption data and ΔE for the dithiolene complex are larger than for the corresponding catecholate complex. As the bdi acceptor ligand was not altered between the two sets of D-A complexes, these differences are directly attributable to changes to the donor ligands. Experimental evidence for this is found in the donor-centered oxidations of complexes **1a-c**, which occur at significantly more positive potentials than their catecholate counterparts, as well as the remarkable consistency in the cathodic portion of the voltammograms between complexes **1a-c** and **3.1–3** is evidence of this. While the sulfur atoms in the bdt donor ligand push the donor HOMO to lower energy relative to the acceptor orbitals the diimine-localized LUMO remains well insulated from alterations to the donor ligands.

Ground state electronic structure calculations performed for the model D-A complexes **1a-c**, corroborated the large changes to the frontier MOs in these complexes compared to **3.1–3** caused by the sulfur heteroatoms in the donor ligand. All the calculations in this chapter and Chapter 3 were preformed at the PBE/TZVP level of theory which allows for quantitative comparison of the results of the calculations. The bdt localized 'donor-HOMO' orbitals in **1a-c** are approximately 400 meV lower energy than orbitals in the (cat-tBu$_2$)M(bdi) complexes, and as expected, only small variations in the energy of the bdi-centered LUMOs were observed. The introduction of sulfur atoms that are capable of better overlap with the metal d orbitals resulted elevated energies of the π* orbitals formed from the anti-bonding combination of the metal d$_{yz}$ and chalcogen p$_z$ orbitals. For example, the 'donor-HOMO' and Ni-bdt π* orbitals in

(bdt)Ni(bdi), **1a** , are virtually degenerate while in (cat-*t*Bu₂)Ni(bdi) the 'donor-HOMO' was 500

meV above the Ni-(catecholate) π* orbital. This effect is most dramatic for the nickel complex,

but the energy difference between the donor-HOMO and M-bdt π * orbitals in **1b** and **1c** are both

smaller than in their catecholate analogues.

The large changes that resulted from substituting oxygen for sulfur were not observed

when selenium was used in place of sulfur as the donor chacolgen atom. The UV-vis absorption

spectra of (bds)Pt(bdi) and (bdt)Pt(bdi) were virtually indistinguishable from one another aside

from an increase in the extinction coefficient the LL′CT transition in **2c** and ΔE for **1c** and **2c** are

nearly identical at 1.85 V and 1.83 V, respectively. In these complexes substituting sulfur for

selenium in the donor ligand has negligible effect on the π system energy. This behavior is

consistent with the previous studies of Dibdrov et. al. and Nomura et. al. on the spectroscopic

and electrochemical properties of (L)M(bpy) and (Cp)Ni(L) (L = bdt, bds; M = Ni, Pt).[5,24] DFT

calculations on the GS electronic structure of **2c** and its nickel and palladium congeners, **2a** and

2b respectively, corroborated the experimental findings, and the 'donor-HOMO' orbitals of **2a-c**

are predicted within 10 meV of the same orbitals in **1a-c**.

While the 'donor-HOMO' orbital energies are unaffected by the change to selenium,

elevated energies are observed for the M-bds π* orbitals formed from the anti-bonding

combination of the metal d_{yz} and chalcogen p_z orbitals. In both **2a** and **2c** the M-bds π

antibonding orbital is pushed above the 'donor-HOMO', and ΔDA is a more predictive measure

of the D-A behavior for these complexes. TD-DFT calculation preformed using the

(donor)M(bdi) model systems support the use of ΔDA as an accurate indicator of D-A character

in these complexes.

The LL′CT transitions predicted for the (donor)M(bdi) model complex were consistent with the LL′CT absorptions observed spectroscopically for **1a-c** and **2c**, and the calculated excitations occurred exclusively between the 'donor-HOMO' and the LUMO. No 'M-donor π*' →LUMO excitations were predicted with a significantly large probability for any of the complexes studied, including those where the 'M-donor π*' is higher energy than the 'donor-HOMO'. The increased metal involvement in the HOMOs of these (donor)M(bdi) complexes points to more MMLL′CT character that was observed for the (cat-tBu$_2$)M(bdi) complexes. Beyond the substitution of oxygen for sulfur the chalcogen atom has little effect on the D-A properties in LL′CT dyes.

4.3.2 The Chalcogen and the Metal

These (donor)M(bdi) model complexes also allow us to gain some new insight into the role that metal-donor interactions play in determining the spectroscopic and electrochemical properties of these systems as how changes to these interactions effect the metal atoms participation in the LL′CT process. Experimental and computational evaluations of the Group 10 (donor)M(bdi) complexes suggest that the introduction of donor ligands that can interact more strongly with the metal atom, resulted in smaller differences in the D-A properties between the nickel, palladium and platinum complexes.

Less variation in the LL′CT absorption maxima and ΔE was found between the nickel(II), palladium(II) and platinum(II) derivatives of the (bdt)M(bdi) model system than observed between the different metals in the (cat-tBu$_2$)M(bdi) complexes. While the LL′CT state energies of complexes **3.1–3.3** (E_{CT}) differ by about 300 meV depending on the identity of metal center, **1a-c** are very similar to one another, with a E_{CT} range of only 100 meV. Electrochemically, ΔE values of **1a-c** differ by just 120 mV across the entire series while the

catecholate analogues differ by more than 300 mV. Complexes **1a-c** suggest, counterintuitively, that the presence of the larger sulfur *p* orbitals, which are capable of better overlap with the metal *d* orbitals, evens out the differences between the metals. Unfortunately, a similar comparison of experimental data could not be made for the Group 10 diselenolene series because (bds)Pt(bdi) was the only of these compounds that could be prepared for this report. However, DFT calculations preformed on the other members of the diseleonlene series predict the same behavior as the dithiolene complexes in terms of the calculated and experimentally observed LL′CT absorptions.

The ground state electronic structure calculations performed on the bdt and bds (donor)M(bdi) model complexes provide some insight into why the complexes show smaller metal dependence in the D-A properties. In chapter 3 it was shown that catecholate-centered HOMOs had almost no contribution from the metal *d* orbitals and the important metal contribution of **3.1-3.3** was the amount of and metal-dependent d_{xz} character in the LUMO. As expected{ref}, MPA calculations on the frontier orbitals of the dithiolene and diselenolene containing complexes predicted significant increases in metal d_{xz} orbital contribution to the 'donor-HOMO'. Although the *d* orbital character in the 'donor-HOMO' was, in all cases, significantly greater than in catecholate complexes, the metal d_{xz} orbital mixing into the LUMO was slightly less in the (bdt)M(bdi) and (bds) complexes. Metal dependent variations in the amount of d_{xz} character found in the donor and acceptor orbitals of **1a-c** and **2a-c** and the trend in the amount of d_{xz} mixing in the ligand orbital was Ni > Pt > Pd for both sets of (donor)M(bdi) complexes. This trend differs from the trend detailed in Chapter 3 as well as previously reported (bdt)M(bpy) complexes where platinum was observed to have the largest contribution to the ligand center D-A orbitals.[2] For the complexes introduced in this chapter ΔHL cannot be directly

related to the amount of metal contribution in either the donor or bdi orbitals. It appears that the relative uniformity observed in the spectroscopic and electrochemical properties of complexes **1a-c** and in the calculated properties of **1a-c** and **2a-c** is caused by the interaction of the metal *d* orbital with both the donor and acceptor attenuating the metal ions influence in these D-A complexes.

4.4 Summary

The nickel(II), palladium(II) and platinum(II) (bds)M(bdi) (**1a-c**) and (bds)Pt(bdi) (**2c**) were synthesized and characterized. DFT and TD-DFT calculations preformed **1a-c** along with **2c** and its the nickel(II), (**2a**), and palladium(II), (**2b**) analogues. The UV-vis-NIR absorption spectra and electrochemistry of **1a-c** showed that substitution of oxygen for sulfur as the donor-ligand heteroatom resulted in a significant decrease in the variation in the spectroscopic and electrochemical properties between the different Group 10 metal ions from the catecholate complexes discussed in Chapter 3. Comparison of (bdt)Pt(bdi) and (bds)Pt(bdi) revealed that the substitution of sulfur for selenium had virtually no effect on the observed spectroscopic and electrochemical properties from **1c** to **2c.** Comparison of **1a-c** and **2a-c** revealed that the energy of the 'donor-HOMO' orbital between the bdt and bds complexes was nearly identical. In fact the only significant difference observed between the electronic structures of **1a-c** and **2a-c** was the energy of the M-donor π* orbital between the metal d_{yz} orbital and the chalcogen p_z orbital. This chapter represents the first combined experimental and computational investigation into the effect of chalcogen heteroatom identity of the donor ligand on the degree of metal contribution to the HOMO and LUMO of these donor acceptor complexes.

DFT and TD-DFT analysis of **1a-c** showed a significant increase in the amount of metal mixing in the bds 'donor-HOMO' orbitals from the catecholate complexes of Chapter 3. The

percentage of metal d_{xz} character in the dithiolene-centered donor-HOMO orbitals was comparable amount of metal d_{xz} character in the diimine-localized LUMO, regardless of the metal atom, which is attributed to the observed decrease in the metal influence over the D-A propertied observed experimentally.

4.5 Experimental

General Methods. The complexes described below are air- and moisture-sensitive; therefore, manipulations were carried out under an inert atmosphere of argon or nitrogen using standard Schlenk, vacuum-line, and glovebox techniques. All reactions were carried out at ambient temperature (20–28 °C). Hydrocarbon solvents were sparged with argon then passed through activated alumina and Q5 columns to remove water and oxygen respectively. Ethereal and halogenated solvents were sparged with argon, then dried by passage through two activated alumina columns. To test for water and oxygen removal, nonhalogenated solvents were treated with a drop of a solution of sodium benzophenone ketyl in THF. The ligand *mes*-BDI was prepared according to established procedures.[25] The metal precursors (BDI)MCl$_2$ (M = Ni, Pd, Pt) were prepared by a previously reported procedure.[26,27]

General (bdt)Ni(bdi) Synthesis. A slurry of (bdi)MCl$_2$ in a THF or DCM solution was treated with one equivalent of 1,2-benzenedithiol and 2.1 equivalents of amine base. A dark blue color was observed immediately upon the addition of the base. The reaction mixture was allowed to stir for 12 h then filtered to remove the insoluble ammonium chloride salt. The volume of the filtrate was reduced under vacuo, diluted with pentane and stored at –35 °C. The resulting precipitate was collected by filtration, washed with aliquots of cold pentane and dried under reduced pressure to obtain the desired product as a darkly colored solid.

Synthesis of (bdt)Ni(bdi) (1a). Complex **1a** was prepared according to the general method described above in THF using 225 mg (BDI)NiCl$_2$ (0.5 mmol, 1.0 equiv), 1,2-benzenedithiol (57 μL, 0.50 mmol 1.0 equiv), and triethylamine (153.4 μL, 1.1 mmol 2.2 equiv). The product was isolated as a dark blue solid in 77.1% yield (198 mg)
 Anal. Calcd. (Found) for C$_{36}$H$_{48}$N$_2$S$_2$Ni: C, 64.75 (64.26); H, 6.21 (6.05); N, 5.39 (5.19). ^{1}H NMR (CDCl$_3$, 500 MHz) δ/ppm: 7.06 (dd, J = 5.4, 3.2 Hz, 2H), 7.01 (s, 4H), 6.68 (dd, J = 5.8, 3.2 Hz, 2H), 2.39 (s, 6H), 2.33 (s, 12H), 1.64 (s, 6H). UV-vis-NIR (CH$_2$Cl$_2$) λ_{max}/nm (ε/M^{-1} cm^{-1}): 664 (5700).

Synthesis of (bdt)Pd(bdi) (1b). Complex **1b** was prepared according to the general method described above in DCM using 293 mg (BDI)PdCl$_2$ (0.50 mmol, 1.0 equiv), 1,2-benzenedithiol (57 μL, 0.50 mmol 1.0 equiv), and triethylamine (153.4 μL, 1.1 mmol 2.2 equiv). The product was isolated as a dark blue-green solid in 8 5% yield (241 mg)

¹H NMR (CDCl₃, 500 MHz) δ/ppm: 7.29 (s, 2H), 7.06 (s, 4H), 6.64 (s, 2H), 2.44 (s, 6H), 2.29 (s, 12H), 1.58 (s, 6H). UV-vis-NIR (CH₂Cl₂) λ_{max}/nm (ε/M⁻¹cm⁻¹): 658 (2900).

Synthesis of (bdt)Pd(bdi) (1c). Complex **1c** was prepared according to the general method described above in DCM using 250 mg (BDI)PdCl₂ (0.50 mmol, 1.0 equiv), 1,2-benzenedithiol (57 μL, 0.50 mmol 1.0 equiv), and triethylamine (155.5 μL, 1.1 mmol 2.2 equiv). The product was isolated as a dark blue solid in 83 % yield (270 mg)

Anal. Calcd. (Found) for C₃₆H₄₈N₂S₂Pt: C, 51.28 (51.05); H, 4.92 (4.56); N, 4.27 (3.90). ¹H NMR (CDCl₃, 500 MHz) δ/ppm: 7.02 (s, 4H), 6.97 (s, 2H), 6.68 (s, 2H), 2.38 (s, 6H), 2.28 (s, 12H), 1.99 (s, 6H). UV-vis-NIR (CH₂Cl₂) λ_{max}/nm (ε/M⁻¹cm⁻¹): 664 (13000).

Synthesis of (bds)Pd(bdi) (1c). Monomeric (bds)²⁻ was prepared in a on a nitrogen manifold in dry, degassed MeOH by reduction of the [bds]ₙ oligomer (46.8 mg, 0.2 mmol, 2 equiv) with NaBH₄ (50 mg, 1.30 mmol, excess) as previously described.[28] The MeOH solution of (bds)²⁻ was concentrated under vacuum to give a yellow film. The reaction vessel was then transferred to a nitrogen glovebox and redissolved in THF (10 mL). This solution was added drop wise to a slurry of 59 mg (BDI)PtCl₂ (0.1 mmil, 1 equiv), the reaction mixture immediately developed a dark blue color. The solution was allowed to stir 1 h after which the solvent was removed *in vacuo*. The desired product was extracted from the residue by washing with 15 mL DCM, the resulting slurry was then filtered. The volume of the filtrate was reduced under vacuo, diluted with pentane and stored at –35 °C. The resulting precipitate was collected by filtration, washed with aliquots of cold pentane and dried under reduced pressure to obtain the desired product as a darkly colored solid in 60% yield (44.6 mg).

¹H-NMR (400 MHz; CDCl₃): δ 7.44 (dd, *J* = 5.9, 3.3 Hz, 2H), 7.05 (s, 4H), 6.67 (dd, *J* = 5.9, 3.3 Hz, 2H), 2.44 (s, 6H), 2.31 (s, 13H), 1.42 (s, 6H). UV-vis-NIR (CH₂Cl₂) λ_{max}/nm (ε/M⁻¹cm⁻¹): 664 (18100).

Physical Methods. NMR spectra were collected on Bruker Avance 500 MHz spectrometers in dry, degassed CDCl₃. ¹H NMR spectra were referenced to tetramethylsilane (TMS) using the residual proteo impurities of the solvent; ¹³C NMR spectra were referenced to TMS using the natural abundance ¹³C impurities of the solvent. All chemical shifts are reported using the standard à notation in parts per million; positive chemical shifts are to a higher frequency from the given reference. IR spectra were recorded as KBr pellets with a Perkin-Elmer Spectrum One FTIR spectro- photometer. Electronic absorption spectra were recorded with a Perkin-Elmer Lambda 800 UV-vis spectrophotometer. Perpendicular-mode X-band EPR spectra were collected using a Bruker EMX spectrometer equipped with an ER041XG microwave bridge.

Electrochemical Methods. Electrochemical Methods. Electrochemical experiments were performed on a Gamry Series G 300 potentiostat/galvanostat/ ZRA (Gamry Instruments, Warminster, PA) using a 3.0 mm glassy carbon working electrode, a platinum wire auxiliary electrode, and a silver wire reference electrode. Electrochemical experiments were performed at ambient temperature (20–24 °C), either in a nitrogen-filled glovebox or under an atmosphere of argon. Sample concentrations were 1.0 mM in THF with 0.10 M NBu4PF6 as the supporting

electrolyte. All potentials are referenced to $[Cp_2Fe]^{+/0}$ using ferrocene or decamethylferrocene as an internal standard (-0.49 V vs $[Cp_2Fe]^{+/0}$). The typical solvent system window 2with our configuration was $+1.0$ V for the oxidation limit and -3.4 V for the reduction limit (vs $[Cp_2Fe]_{-}$/ 0). Decamethylferrocene (Acros) was purified by sublimation under reduced pressure and tetrabutylammonium hexafluorophosphate (Acros) was recrystallized from ethanol three times and dried under vacuum.

Computational Methods: All calculations were performed using the TURBOMOLE program package.[ref] The geometric and electronic structures were optimized without symmetry constraints using the PBE functional[20,21] and a polarized triple-ζ basis set (TZVP). [22] All molecules were treated in the gas phase without accounting for solvent. The energy was converged to 10^{-7} Hartree. Mulliken population analyses [29] and plots were also obtained at the PBE/ TZVP level; the contour values were 0.03 for the molecular orbital plots.

Crystallographic Methods. X-ray diffraction data were collected on crystals mounted on glass fibers using a Bruker CCD platform diffractometer equipped with a CCD detector. Measurements were carried out at 93 or 163 K using Mo Kα ($\lambda = 0.710\ 73$ Å) radiation, which was wavelength-selected with a single-crystal graphite monochromator. The SMART program package was used to determine unit-cell parameters and to collect data. The raw frame data were processed using SAINT and SADABS to yield the reflection data files. Subsequent calculations were carried out using the SHELXTL program suite. Structures were solved by direct methods and refined on F^2 by full-matrix least-squares techniques. Analytical scattering factors for neutral atoms were used throughout the analyses. Hydrogen atoms were included using a riding model. ORTEP diagrams were generated using ORTEP-3 for Windows.

4.6 References

1. Cocker, T.; Bachman, R. *Inorg Chem* **2001**, *40*, 1550.
2. Mitsopoulou, C. A. 2010; Vol. 254, pp. 1448–1456.
3. Cummings, S.; Eisenberg, R. *J Am Chem Soc* **1996**, *118*, 1949.
4. Paw, W.; Cummings, S.; Adnan Mansour, M.; Connick, W.; Geiger, D.; Eisenberg, R. *Coordination Chemistry Reviews* **1998**, *171*, 125.
5. Dibrov, S.; Bachman, R. *Inorganica Chimica Acta* **2004**, *357*, 1198.
6. Espa, D.; Pilia, L.; Marchiò, L.; Pizzotti, M.; Robertson, N.; Tessore, F.; Mercuri, M. L.; Serpe, A.; Deplano, P. *Dalton Trans*. **2012**, *41*, 12106.
7. Zuleta, J. A.; Bevilacqua, J. M.; Proserpio, D. M.; Harvey, P. D.; Eisenberg, R. *Inorg Chem* **1992**, *31*, 2396.
8. Cummings, S. D.; Cheng, L.-T.; Eisenberg, R. *Chem. Mater* **1997**, *9*, 440.
9. Weinstein, J. A.; Zheligovskaya, N. N.; Mel'nikov, M. Y.; Hartl, F. *J. Chem. Soc., Dalton Trans*. **1998**, 2459.
10. Espa, D.; Pilia, L.; Marchiò, L.; Mercuri, M. L.; Serpe, A.; Barsella, A.; Fort, A.; Dalgleish, S. J.; Robertson, N.; Deplano, P. *Inorg Chem* **2011**, *50*, 2058.
11. Ford, S.; Morley, C. P.; Di Vaira, M. *Inorg Chem* **2004**, *43*, 7101.
12. Sproules, S.; Eagle, A. A.; Taylor, M. K.; Gable, R. W.; White, J. M.; Young, C. G. *Inorg Chem* **2011**, *50*, 4503.
13. Pilia, L.; Espa, D.; Barsella, A.; Fort, A.; Makedonas, C.; Marchiò, L.; Mercuri, M. L.; Serpe, A.; Mitsopoulou, C. A.; Deplano, P. *Inorg Chem* **2011**, *50*, 10015.

14. Archer, S.; Weinstein, J. A. *Coordination Chemistry Reviews* **2012**, *256*, 2530.

15. Makedonas, C.; Mitsopoulou, C.; Lahoz, F.; Balana, A. *Inorg Chem* **2003**, *42*, 8853.

16. Best, J.; Sazanovich, I. V.; Adams, H.; Bennett, R. D.; Davies, E. S.; Meijer, A. J. H. M.; Towrie, M.; Tikhomirov, S. A.; Bouganov, O. V.; Ward, M. D.; Weinstein, J. A. *Inorg Chem* **2010**, *49*, 10041.

17. Adams, C. J.; Fey, N.; Parfitt, M.; Pope, S. J. A.; Weinstein, J. A. *Dalton Trans*. **2007**, 4446.

18. Oblad, P. F.; Bercaw, J. E.; Hazari, N.; Labinger, J. A. *Organometallics* **2010**, *29*, 789.

19. Deplano, P.; Pilia, L.; Espa, D.; Mercuri, M. L.; Serpe, A. *Coordination Chemistry Reviews* **2010**, *254*, 1434.

20. Perdew, J. P.; Burke, K.; Ernzerhof, M. *Phys. Rev. Lett*. **1996**, *77*, 3865.

21. Perdew, J. P.; Burke, K.; Ernzerhof, M. *Phys. Rev. Lett*. **1997**, *78*, 1396.

22. Weigend, F.; Ahlrichs, R. *Phys. Chem. Chem. Phys*. **2005**, *7*, 3297.

23. Nomura, M.; Cauchy, T.; Geoffroy, M.; Adkine, P.; Fourmigué, M. *Inorg Chem* **2006**, *45*, 8194.

24. Nomura, M.; Cauchy, T.; Fourmigué, M. *Coordination Chemistry Reviews* **2010**, *254*, 1406.

25. Zhong, H. A.; Labinger, J. A.; Bercaw, J. E. *J Am Chem Soc* **2002**, *124*, 1378.

26. van Asselt, R.; Elsevier, C. J.; Amatore, C.; Jutand, A. *Organometallics* **1997**, *16*, 317.

27. Scollard, J. D.; Day, M.; Labinger, J. A.; Bercaw, J. E. *HCA* **2001**, *84*, 3247.

28. Sandman, D. J.; Allen, G. W.; Acampora, L. A.; Stark, J. C.; Jansen, S.; Jones, M. T.; Ashwell, G. J.; Foxman, B. M. *Inorg Chem* **1987**, *26*, 1664.

29. Mulliken, R. S. *J. Chem. Phys*. **1955**, *23*, 1833.

Chapter 5
Computational Study of LL′CT Behavior in (donor)Rh(phdi)X$_2$ Complexes

5.1 Introduction

We are interested in expanding the scope of the D-A LL′CT chromophore 'toolbox' described in Chapter 1 to include octahedral *trans*-(donor)M(acceptor)X_2 complexes with the Group 9 metals. These octahedral D-A LL′CT complexes are desirable for several reasons. The octahedral *trans*-X_2 geometry of the Group 9 dyes removes the open, axial coordination site of the square-planar dyes, removing the possibility of dye ligand displacement by coordinating solvents or external ligands. The stability inherent to the d_6 electron configuration of Co(III), Rh(III) and Ir(III) in octahedral coordination environments renders such complexes kinetically inert, due to filled 't_{2g}' orbitals. This increased stability could be key to the development of robust and long-lived dyes which is important to the long-term viability of dye-sensitized artificial photosynthetic applications. Additionally, octahedral Group 9 D-A LL′CT chromophores could be used as hole-injecting dyes in the water oxidation side of a water splitting tandem-cell. A photocathode capable of preforming the oxygen evolving reaction ($H_2O \longrightarrow O_2 + 2\ H^+ + 2\ e^-$) requires low energy holes (~1.5 V vs SHE),[1] a D-A LL′CT dye capable of injecting such a low energy hole must have a lower energy 'donor-HOMO' than we have been able to incorporate in square-planar Group 10 complexes. One of the requirements of donor-acceptor (D-A) LL′CT dyes is that the metal *d* orbitals must be energetically removed from the ligand-based frontier orbitals to avoid metal-based excited states that can deactivate the LL′CT excited state.[2] The large ligand field splitting displayed by Group 9 metals in the +3 oxidation state further stabilizes the filled metal *d* orbitals allowing for the incorporation of more oxidizing donor ligands than can be used in d_8 Group 10 donor-acceptor complexes. The ability to synthesize D-A chromophores with low-lying donor orbitals is crucial if these complexes are to be used for hole injection into p-type semiconductors capable of direct water oxidation.

**Scheme 5.1**. Synthesis of *trans*-(donor)M(acceptor)X_2 D-A LL′CT complexes **1a**, **1b** and **2**.

dpp = 2,6-diisopropylphenyl   R = CH_3 X = Cl, (**1a**), Br (**1b**) R = CF_3; X = Cl (**2**)
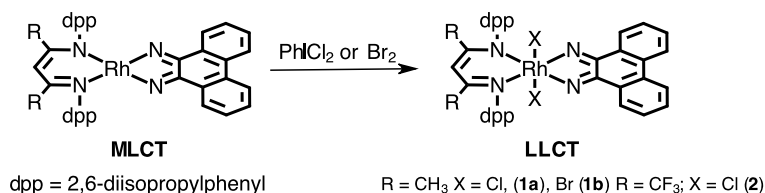
We have previously reported a series of (dpp-nacnac^R)Rh^I(phdi) complexes {(dpp-nacnacR)$^-$ = CH[C(R)-(N-iPr$_2$C$_6$H$_3$)]$_2$$^-$ (R = CH$_3$, CF$_3$), phdi =9,10-phenanthrenediimine}.[3] Though strong charge transfer absorptions are observed from both rhodium(I) complexes, the introduction of electron-withdrawing -CF$_3$ groups to the nacnac ligand has little effect on the absorption maxima, suggesting that the nacnac is not involved in the charge transfer and that the transition is more metal-to-diimine in character. Oxidation of the species to rhodium(III), using either PhICl$_2$ or Br$_2$ (Scheme 5.1) to form *trans*-(dpp-nacnac^R)Rh^{III}(phdi)X$_2$ [R = CH$_3$, X= Cl (**1a**), Br (**1b**); R = CF$_3$ X = Cl (**2**)], resulted in a new charge transfer absorption that is strongly dependent on the nacnac ligand backbone substituents.[4] As shown in Figure 5.1, the charge transfer absorption of the nacnac^{CF3} complex is significantly blue-shifted from the absorption its nacnac^{CH3} analogue. The substituent effect shows that oxidation of the Rh(I) to Rh(III) activates D-A LL′CT behavior from the nacnac ligand to the phdi ligand.

These complexes represent rare examples of octahedral D-A complexes directly analogous to the square-planar Group 10 systems discussed in the previous chapters. While there are reports of heteroleptic derivatives of Ru-bpy that display mixed MLCT/LL′CT,[5-10] a thorough search of the literature on this topic revealed only three other reports of octahedral complexes which display directional LL′CT resembling the kind observed in complexes **1–2**.[11-13]
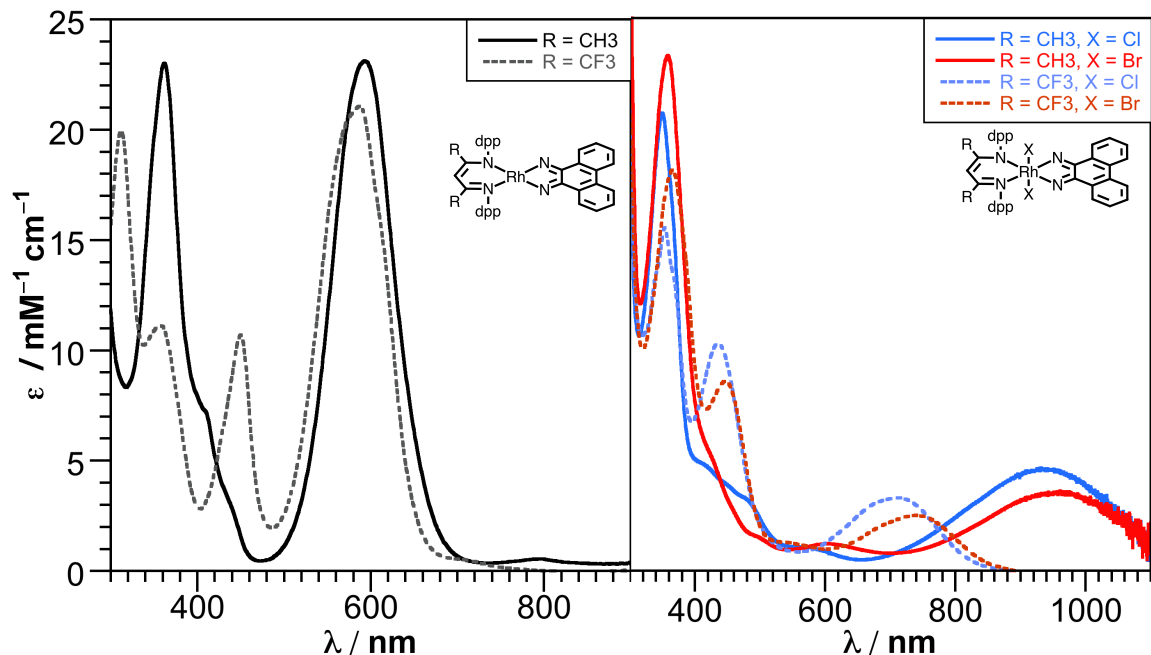
Figure 5.1. (Left) UV-vis-NIR spectra of (dpp-nacnac^CH3)Rh^I(phdi) (——) and (dpp-nacnac^CH3)Rh^I(phdi) (- - -) in DCM at 298 K. (Right) (dpp-nacnac^CH3)Rh(phdi)Cl₂ (**1a**), (dpp-nacnac^CF3)Rh(phdi)Cl₂ (**1b**), (dpp-nacnac^CH3)-Rh(phdi)Cl₂ (**2**), and (dpp-nacnac^CF3)RhBr₂(phdi) in DCM at 298 K.[3]

This chapter presents a detailed computational study of the (dpp-nacnac^R)Rh(phdi)X₂ D-A LL′CT complexes. A benchmarking DFT and TD-DFT study was conducted and it was determined that PBE0 was the functional that most accurately described the properties of these octahedral rhodium(III) complexes. Using this method we were able to determine the influence of the halide ligand on the frontier orbitals that participate in the LL′CT. The effects of donor ligand modification on the electronic structure of these octahedral LL′CT dyes was also investigated by preforming calculations on model complexes with (dpp-nacnac^R)⁻ (R= CH₃, CF₃) (dpp-NacAc)⁻ and acac (dpp-NacAc = [C(CH₃)-O]CH[C(CH₃)-(N-iPr₂C₆H₃)]₂⁻, acac = acetylacetonate) as the donor ligands. These calculations showed that the LLCT complexes showed that the frontier molecular orbitals (MOs) can be tuned in the same way as more traditional LL′CT complexes.
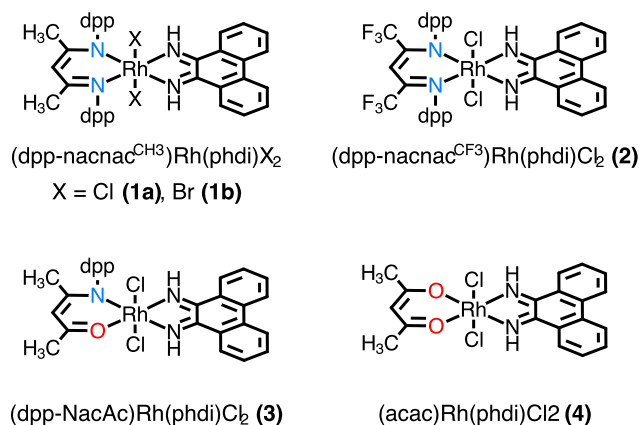
Figure 5.2. Octahedral (donor)Rh(phdi)X$_2$ complexes **1-4**.

5.2 Results
5.2.1 Functional Benchmarking.

While the density functional theory (DFT) studies performed in the previous chapters at the PBE/TZVP level of theory were found to adequately describe the properties of the Group 10 square-planar (donor)M(acceptor) complexes, the octahedral (donor)Rh(phdi)X$_2$ had not yet been studied in great detail. Because there was no need for a quantitative comparison of the results obtained for complexes **1-4** to those of the previous chapters, and in order to maximize the accuracy of these studies, it was necessary to determine the best computational method to describe the properties of the previously reported complexes **1-2** prior to any theoretical investigation with this new octahedral D-A platform. For this benchmarking study calculations were performed using the experimentally characterized model complexes (^{dpp}nacnac-CH$_3$)Rh(phdi)Cl$_2$, **1a**, (^{dpp}nacnac-CH$_3$)Rh(phdi)Br$_2$, **1b** and (^{dpp}nacnac-CF$_3$)Rh(phdi)Cl$_2$, **2**. The pure GGA functional PBE[14,15] and the hybrid GGA functionals PBE0[16,17] and B3LYP[18] were compared in this benchmarking study complexes **1a**, **1b** and **2**. Additionally, for complex **1a**, the hybrid metta-GGA functional, TPSSH,[19,20] was also tested. All the geometry optimization calculations were done using the simpler def2-SV(P) basis set, and all electronic property and

TD-DFT calculations were preformed using the higher quality def2-TZVP to ensure accurate results for these more complicated computations. The performance of each functional was evaluated based on its accuracy at describing: (1) the X-ray crystal structures of **1a** and **2** (no structural data was available for complex **1b**) and (2) the energy of the dpp-nacnac^R→phdi LL′CT transitions observed in the UV-vis-NIR spectra of **1a**, **1b** and **2**.

Table 5.1. Comparison of calculated and observed bond lengths of **1** and **2**.

	Bond lengths / Å								
	1a					**2**			
	PBE	**PBE0**	**B3LYP**	**TPSSH**	**obs.**	**PBE**	**PBE0**	**B3LYP**	**obs.**
Rh-Cl1	2.40	2.37	2.41	2.39	2.35	2.40	2.37	2.41	2.36
Rh-N1	2.09	2.07	2.10	2.08	2.09	2.10	2.09	2.12	2.08
N1-C1	1.34	1.32	1.33	1.33	1.32	1.33	1.31	1.32	1.31
C1-C2	1.41	1.40	1.41	1.41	1.40	1.41	1.40	1.41	1.40
Rh-N3	2.01	2.01	2.04	2.01	2.04	2.03	2.01	2.03	2.02
N4-C4	1.32	1.29	1.30	1.31	1.29	1.32	1.29	1.30	1.29
C4-C5	1.46	1.47	1.48	1.47	1.47	1.47	1.47	1.48	1.48

Metrical parameters obtained for the optimized geometries of **1a** and **2** are shown in Table 5.1. For both complexes, PBE0 produced bond distances closest to the experimental values. In the case of **1a,** the calculated and observed bond distances differed by no more than 0.03 Å using PBE0 as the functional, and for **2** the PBE0 bond lengths were within 0.01 Å. The results of the TD-DFT calculations for the LL′CT transitions of **1a**, **1b** and **2** are given in Table 5.2. Calculations using PBE0 again produced results that most accurately described the experimental

results, while PBE, B3LYP and TPSSH considerably underestimated the energy of the LL′CT excitations. For both metrics, calculations employing the PBE0 functional most accurately reproduced the experimental data, and all other calculations discussed in this chapter were performed using exclusively PBE0 as the functional.

Table 5.2. Comparison of calculated and observed LL′CT energies of **1a**, **1b**, and **2**.

	$E_{LL'CT}$				
	PBE	**PBE0**	**B3LYP**	**TPSSH**	**obs.**
1a	**1.11**	**1.26**	**1.12**	**1.12**	**1.33**
1b	**1.02**	**1.18**	**1.05**	**—**	**1.29**
2	**1.18**	**1.52**	**1.36**	**—**	**1.74**

5.2.3 Halide involvement in LL′CT.

The UV-vis-NIR spectra in Figure 5.1b show a minor red-shift in the LL′CT absorption upon exchange of the chloride ligands in **1a** for bromide in **1b**. Complexes **1a** and **1b** differ only in the identity of their halide ligands, and this red-shift indicate that there is some halide contribution to orbitals responsible for the LL′CT transition. Electronic structure calculations were conducted on complexes **1a** and **1b** to determine in which frontier molecular orbitals was the halide influence largest. The Kohn-Sham (KS) orbitals of **1a** are shown in Figure 5.3 and are qualitatively similar to those of **1b**. Computationally, the difference between chlorine and bromine as the axil halide ligand is manifested as a small decrease in the HOMO-LUMO gap (ΔHL) of (dpp-nacnac^{CH3})Rh(phdi)Br$_2$, **1b**, from (dpp-nacnac^{CH3})Rh(phdi)Cl$_2$, **1a**. The HOMOs of both complexes are largely composed of a (dpp-nacnac^{CH3})$^-$ π non-bonding orbital with smaller contributions from the metal d_{xz} orbital and halide ligands. The LUMO is composed almost entirely of π* orbitals from the phdi acceptor ligand. The parentage of the frontier molecular

orbitals of **1a** and **1b** was quantified using Mulliken population analysis. This analysis confirmed the qualitative assessment that the HOMOs are primarily ^{dpp}nacnac-CH$_3$ centered (**1a**: 83.5 %; **1b**: 80.7 %) and that the LUMO is acceptor-based (**1a**: 89.0%; **1b**: 88.6%). Virtually no halide character was founding in the phdi-centered LUMO of either complex. The HOMO has the greatest contribution from halogen orbitals; chloride character makes up 5.4% of the HOMO in **1a**, while 8.5% of the HOMO in **1b** is from the bromide ligands. Table 5.3 contains the energy of the HOMO and LUMO, ΔHL and the composition of all model complexes presented in this chapter.
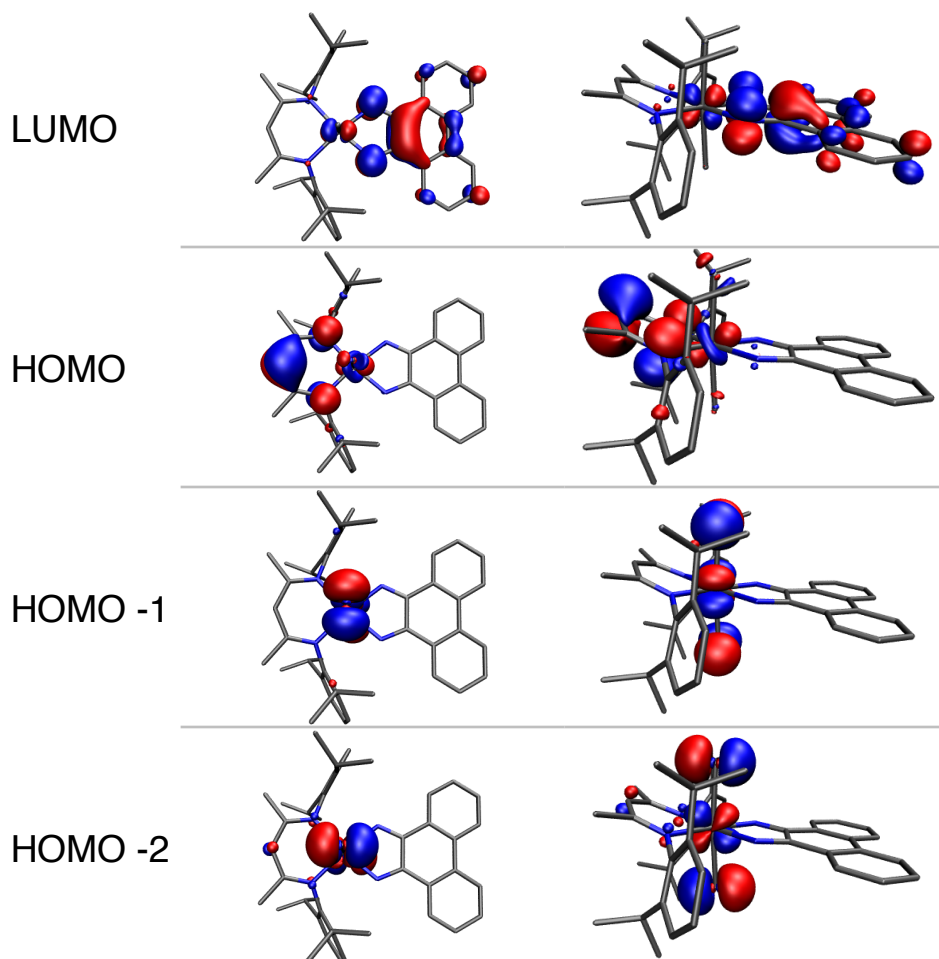
Figure 5.3. Top and side views of the calculated KS orbitals of complex **1a**. From top to bottom: LUMO, HOMO, HOMO–1 and HOMO-2.

TD-DFT calculations were preformed to confirm the identity of the orbitals involved in the charge-transfer absorptions. For both complexes **1a** and **1b** the calculated low-energy excitations occurred exclusively from the HOMO to the LUMO, or from the nacnac donor to the phdi acceptor. The calculated energies of these LL′CT transitions were in good agreement with the experimental absorption spectra for both complexes and showed the excitation of **1a** to be higher energy than for **1b**. Based on the results of these calculations, it can be concluded that the small red-shift observed in going from **1a** to **1b** is due to a larger halide contribution to the HOMO and LUMO in the bromide complex which raises the energy of the HOMO slightly due to the increased halide contribution to the donor orbital.

Table 5.3. Energy and composition of the frontier orbitals of (donor)Rh(phdi)X_2 complexes **1-4**. (donor = (dpp-nacnac^{CH3})⁻, X = Cl(**1b**), Br(**1b**); (dpp-nacnac^{CF3})⁻ (**2**) , (dpp-NacAc)⁻ (**3**) and acac (**4**); X = Cl)

	Gap / eV	Orbital	E / eV	Composition			
				M	donor	phdi	Cl
1a	1.90	HOMO	-5.23	7.7	83.5	3.4	5.4
		LUMO	-3.33	7.8	2.6	89.0	0.6
1b	1.86	HOMO	-5.21	8.2	80.7	37.9	8.5
		LUMO	-3.34	7.4	2.1	88.6	1.9
2	2.24	HOMO	-5.86	10.7	80.1	1.4	7.8
		LUMO	-3.62	6.8	0.6	91.3	1.4
3	2.22	HOMO	-5.65	9.5	79.6	1.6	9.2
		LUMO	-3.43	8.5	0.7	89.1	1.6
4	2.62	HOMO	-6.10	18.6	50.5	3.0	28.0
		LUMO	-3.48	9.4	0.6	87.9	2.0

5.2.3 Modification to the Donor Ligand.

The UV-vis-NIR spectra of complexes **1a** and **2** show a dramatic blue-shift of the LL′CT absorption of **2** caused by the substitution of the nacnac backbone methyl groups in **1a** for the

electron withdrawing perfluoromethyl substituents in the nacnac backbone in **2**. This effect is similar to the results observed from the (cat-R)Ni(diimine) complexes discussed in Chapter 2, where the complexes using the relatively electron poor (cat-Cl$_4$)$^{2-}$ donor display LL$'$CT absorptions that are much higher energy than those with the (cat-tBu$_2$)$^{2-}$ donor. These modifications to the ligand electronics through changing the substituents in the backbone represent just one possible way to tune the energetics of the donor ligand orbitals.

It is well known in the chemistry of catecholate (cat) and its nitrogen-containing analogues, *o*-aminophenol (ap), and *o*-phenylenediamine (da), that the energy of the ligand orbitals follows the trend da > ap > cat.[21] The same logic can be applied to the exchange of one or both nitrogens in the (dpp-nacnac^{CH3})$^-$ donor ligand for oxygen. For this ligand series the expected ordering of the donor orbital energies would be nacnac (N,N) > NacAc (N,O) > acac (O,O). Ground and excited-state calculations of the (donor)Rh(phdi)Cl$_2$ complexes shown in Figure 5.1 [donor = (dpp-nacnac^{CH3})$^-$ (**1a**), (dpp-nacnac^{CF3})$^-$ (**2**) , (dpp-NacAc)$^-$ (**3**) and acac (**4**)] were performed to understand the D-A behavior displayed by complexes **1a** and **2** and to investigate how we might extend this chemistry to develop a new family of octahedral D-A LL$'$CT chromophores.

Table 5.4. Energy, f, and composition of calculated excitations of 1-4 that display LL′CT character.

	E_{LL}			
	calc	expt	f	Composition
1a	1.26	1.33	0.060	HOMO→LUMO (98.9%)
1b	1.18	1.29	0.040	HOMO→LUMO (98.6%)
2	1.52	1.74	0.044	HOMO→LUMO (98.6%)
3	1.47	–	0.034	HOMO→LUMO (84.1 %) + HOMO–1→LUMO (13.9%)
	1.77	–	0.038	HOMO–1→LUMO (83.5 %) + HOMO→LUMO (14.4%)
4	1.84	–	0.071	HOMO→LUMO (89.1 %) + HOMO–2→LUMO (9.1%)

The changes observed in the optimized molecular structures of complexes **3** and **4** from complex **1a** and **2** are consistent with the sequential exchange of the nitrogen atoms of the nacnac ligand for oxygen. The calculated structure of **3** displayed Rh–N_{phdi} bond lengths similar to those of the dpp-nacnac^R complexes (Rh–N_{transO} =1.98 Å and Rh–N_{transN} = 2.02 Å) while the Rh-N_{phdi} bonds of **4** (1.96 Å) were slightly shorter. The Rh-O bond lengths predicted for both **3** and **4** (2.06 Å and 2.00 Å respectively) are in good agreement with those expected for an (acac)Rh(III) complex.[22] Additionally, while the Rh-Cl bonds of the calculated structures of **1a**, **2**, and **3** were all ~ 2.37 Å, the Rh-Cl bonds of **4** were predicted to be slightly shorter at 2.34 Å, indicative of a more electron poor metal center. The calculated intraligand bond distances in the phdi acceptor ligand in complexes **3** and **4** were unaffected by changes to the donor ligands and were in good agreement with those observed in the X-ray structures of complexes **1** and **2**. The molecular structures predicted for the model NacAc and acac complexes appear to be reasonable and the electronic structure calculations were carried out with confidence that they would also produce informative results.
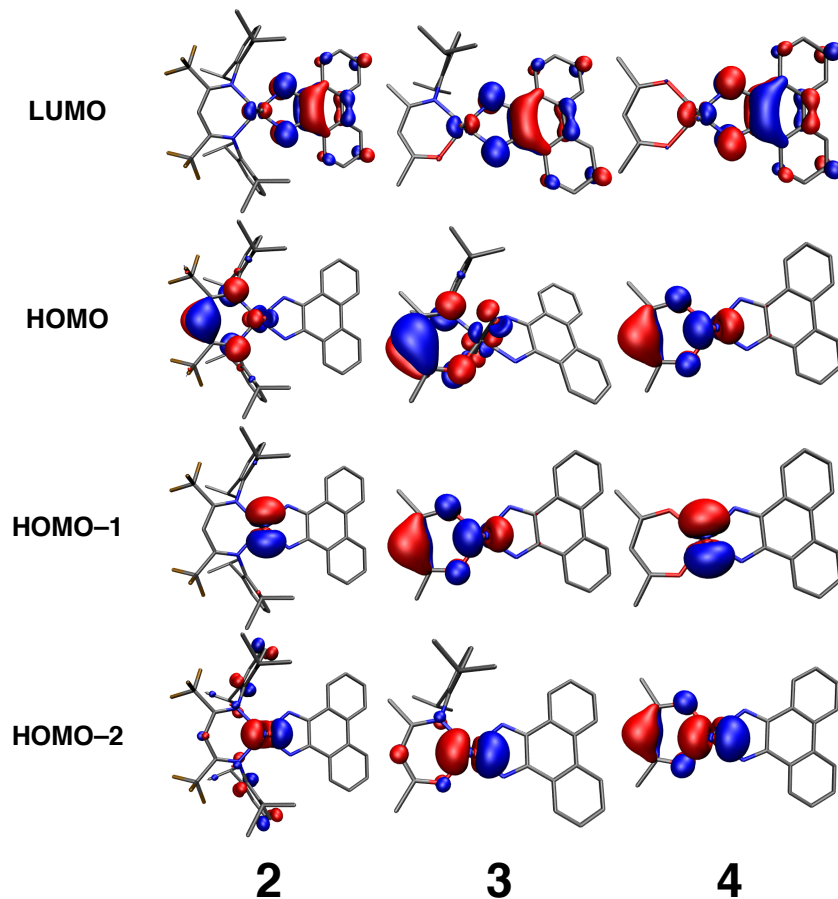
Figure 5.4. KS LUMO, HOMO, HOMO–1 orbitals of complexes **2-4**.

The calculated frontier MOs of the (donor)Rh(phdi)Cl$_2$ complexes illustrate how changes to the changes donor ligands influences the energy and composition of the MOs. As with all the other D-A LL′CT complexes discussed in the previous chapters, the energy of the LUMO was consistent across the series, the energy of the HOMO was shown to decrease in the order: **1a** > **3** > **2** > **4** and the order of ΔHL increases correspondingly where ΔHL **1a** < **3** ≅ **2** < **4**. The KS frontier MOs of the D-A complexes **2-4** are shown in Figure 5.4. The calculated energies of the HOMO, LUMO, ΔHL, and Muliken population analyses of each orbital are tabulated in Table 5.3. Like complex **1a**, the HOMOs of complexes **2**, **3** and **4** are primarily composed from the π^{nb}

orbital of the donor ligand. Muliken population analysis of the HOMOs in complexes **1-4** show the effect of these changes to the donor ligands on the composition of the molecular orbital. The amount of mixing in the HOMO observed from the rhodium d_{xz} orbitals and p_x orbitals of the chloride ligands in the occupied frontier orbitals is dependent on the identity of the donor ligand. The d_{xz} and chloride p_x orbital mixing increased as the energy of the donor ligand π system was pushed to lower energies with electron withdrawing -CF$_3$ groups in the nacnac backbone or by the substitution of nitrogen for oxygen. Complexes **2** and **3** showed moderate increases in the amount of mixing from the metal and chlorides compared to **1b**, but the acac complex, **4**, showed much larger metal and chloride character than any of the other complexes studied. The metal d_{xz} made up nearly 20% of the HOMO in **4** and the chlorides p_x 28%. In every member of this series the LUMO is steadfastly localized on the acceptor, with Muliken population analysis showing between 88-91% of the orbital coming from the phdi ligand. Complexes **3** and **4** show significant donor-π^{nb} character in the HOMO–2 that was not observed for either **1a** and **2**, which is also a result of the lower energy donor π systems of the NacAc and acac ligands.

TD-DFT (PBE0/TZVP) calculations predicted low energy HOMO→LUMO LL′CT transitions for complexes **2-4**, similar to that found for **1a**. Shown in Table 5.4 are the calculated and experimental (for **1a** and **2**) LL′CT energies, and the orbitals involved in the calculated excitations. Like **1a**, the LL′CT of **2** was, calculated to be exclusively HOMO→LUMO. The excitations of **3** and **4** on the other hand showed small amounts of character from transitions involving other orbitals. For complex **4,** the other contribution to the LL′CT excitation is a HOMO–2→LUMO transition. Given the large amount of donor orbital character in the HOMO–2 of **4**, this can still be described as having LL′CT character. In the case of complex **3**, there is significant character of a HOMO–1→LUMO transition in the predominantly HOMO→LUMO

excitation. Also, a unique second low-energy excitation, within 0.3 eV of the LL′CT transition and with a similar oscillator strength to the LL′CT, was also predicted for complex **3**. This excitation was primarily HOMO–1→LUMO (84%) but also showed a small contribution (14%) from the HOMO→LUMO transition. The HOMO-1 in complex **3**, and all the other complexes in this report, is a π* orbital between the rhodium d_{yx} and the p_y orbitals of the chlorides. This HOMO–1→LUMO transition can be described as MLCT transition. Because the MLCT HOMO–1 →LUMO excitation is only observed for complex **3**, it is unclear whether this transition is real with out further experimental and computational investigation. The observed order of the LL′CT excitations (majority HOMO→LUMO) for this series was: **4** (1.84 eV) > **2** (1.52 eV) > **3** (1.47 eV) > **1a** (1.26 eV) consistent with the more electronegative O-atom donors effecting a higher ΔHL.

5.3 Discussion

5.3.1 Optimizing the DFT and TD-DFT Computational Method for the Study of the (donor)Rh(phdi)X2 Complexes.

DFT and TD-DFT benchmarking studies were conducted using the PBE, B3LYP, PBE0 and TPSSH functionals to assess the ability of each functional to describe the X-ray structures of **1a** and **2** and the LL′CT absorptions of **1a**, **1b** and **2**. The widely used B3LYP is a semi-empirical functional, meaning it was constructed to fit a specific set of experimental parameters. Alternatively, PBE, PBE0 and TPSSH are non-empirical functionals, which means that no experimental parameters were used in their construction.[23] Non-emperical functionals are generally considered to provide more accurate results because they are not subject to the constraints inherited from forcing the functional to fit a set of experimental parameters. B3LYP, PBE0 and TPSSH are hybrid functionals that incorporate a one-parameter component that allows

for exact electron exchange to be calculated. Hybrid functionals often provide more accurate results than pure functionals like PBE.[24-26] For these systems PBE0 provided the most accurate description of both experimentally observed parameters and was used for the rest of the calculations preformed for this report.

5.3.2 The Axial Ligands Involvement in the LL′CT (dpp-nacnacCH3)Rh(phdi)X2 (X = Cl, Br)

Electronic structure calculations of the (dpp-nacnac^{CH3})Rh(phdi)X$_2$ D-A LL′CT complexes **1a** (X = Cl) and **1b** (X = Br) show the observed red-shift in LL′CT absorption in the UV-vis-NIR spectra of **1b** from **1a** can be attributed to increased halide contribution in the HOMO with bromide is the halide. The LUMOs of both complexes have virtually identical energies and the difference in ΔHL was due to a slight increase in the HOMO energy, relative to the LUMO, in **1b** from **1a**. The LUMO in both complexes is localized predominantly on the phdi ligand and there no halide character is observed in the LUMO of either **1a** or **1b**. The amount of halide character in the nacnac centered HOMOs increased from 5.4% with chloride in **1a** to 8.5% with bromide in **1b**. The halide character in (dpp-nacnac^{CH3})Rh(phdi)X$_2$ HOMO was from the antibonding interaction of the halide p_x orbitals with the rhodium d_{xz} orbital and the increased halide contribution to the HOMO of **1b** is indicative of the M-X π bonding being stronger for bromine than for chloride. This halide effect suggests that the axial ligands of the octahedral D-A dyes provide another variable which can be modified in order to fine-tune the spectroscopic and electrochemical properties of dyes based on this design.

5.3.3 Predicting the effect of Modifications to the Donor Ligands on LL′CT Properties of (donor)Rh(phdi)Cl2 D-A Dyes.

Chapters 1,2 and 4 of this dissertation illustrates that control over the energy of the HOMO and consequently ΔHL of Group 10 square-planar D-A LL′CT dyes is possible through

alterations of donor ligand electronics alone. DFT and TD-DFT calculations on a series of (donor)M(phdi)Cl$_2$ complexes **1a** and **2-4** predict that similar control over the electronic structure is can be achieved for octahedral D-A complex. Experimentally evidence of this is found in the UV-vis-NIR spectra of **1a** and **2**, which show a large blue-shift of the LL′CT transition upon substitution of (dpp-nacnac^{CH3})$^-$ in **1a,** for the weaker (dpp-nacnac^{CF3})$^-$ donor ligand in **2**. Like many of the other D-A complexes discussed in previous chapters, DFT calculations show that the donor and acceptor orbitals are electronically isolated from each other. Despite the electron withdrawing CF$_3$ substituents of **2** pushing the HOMO of **2** (–5.86 eV) to significantly lower in energy than the HOMO of **1a** (–5.23 eV) the energy and composition of the LUMOs of both complexes are practically identical; this resulted in a ΔHL for **2** (2.24 eV) that is much larger than for **1a** (1.90 eV). These two complexes represent one way of tuning the D-A properties of these dyes that is directly analogous to the (cat-R)Ni(diimine) complexes (cat-R = cat-tBu$_2$ or catCl$_4$) presented in Chapter 1, and offer one possible route forward for the further expansion of octahedral D-A LL′CT dyes.

Electronic structure calculations on the model complexes **3** and **4** show that exchange of nitrogen for oxygen may also be a viable way to modulate the energy of the donor centered HOMO and the HOMO-LUMO gap of the Group 9 D-A LL′CT dyes. As expected a lower energy HOMO and an increase in ΔHL was observed each time nitrogen was replaced with oxygen. Introduction of a single oxygen to the donor with the (dppNacAc)$^-$ ligand with **3** had basically the same effect on the energy and composition of the dppNacAc-localized HOMO, compared to **1a** , as was observed in complex **2** for the introduction of the electron withdrawing perfluoromethyls groups. The calculated ΔHL of **2** and **3** are practically identical (2.22 eV and

2.24 eV, respectively) and population analysis showed only slight differences in the overall composition of the HOMOs the two complexes.

Introduction of the second oxygen with acac resulted a further lowering of the HOMO of **4** No significant change in the LUMO was observed between **3** and **4** and (acac)Rh(phdi)Cl$_2$ was predicted to have the largest ΔHL of this series. The introduction of two oxygens make this donor ligand significantly more oxidizing than the nacnac ligands. Although the HOMO of **4** is still predicted to be primarily localized on the acac donor, the lower energy of the acac π^{nb} orbital allowed for more mixing of the Rh-Cl π^* character and a much larger percentage of the HOMO is due to contributions from the rhodium and the chloride ligands. Additionally, there was much more acac π^{nb} character in the HOMO–2 of **4**. As expected, DFT predicted that substitution of oxygen for nitrogen as the donor ligand heteroatom significantly lowers the energy of the donor-centered HOMO. This is the same behavior observed for the more traditional square-planar D-A LL′CT dyes and suggest that dyes based on this design may offer the same degree of tunability of the D-A properties displayed in Chapter 1.

The predicted trend for ΔHL of this series is, **1a** < **3** ≅ **2** < **4**. TD-DFT of **3** and **4** predicted LL′CT excitations that followed the trends shown in the electronic structure calculations where E$_{LL'CT}$ **1a**< **3** ≅ **2** < **4**. Unlike **1a** and **2** though, the excitations of **3** and **4** did not display exclusively HOMO→LUMO character. For complex **4** a small amount of HOMO–2→LUMO character was predicted. This additional character may be an effect of the large amount of mixing between the HOMO and HOMO–2 that was observed in the ground state electronic structure of **4**. The calculated LL′CT HOMO→LUMO excitation of complex **3** showed contribution from the HOMO–1→LUMO transition. This HOMO–1→LUMO transition was also predicted as the primary contribution, with some HOMO→LUMO character as well, to a second intense, low-

energy excitation that was completely unique to **3**. This mixing from the primarily Rh-Cl π*

orbitals, the HOMO–1 and HOMO–2, in the predicted LL′CT excitations of **3** and **4** indicate

stronger metal involvement in the LL′CT of complexes **3** and **4**. However, through substitution

of the axial ligands from π donating halide ligands, which raise the energy of the metal d_{xz} and

d_{yz} orbitals, to π accepting or π non-bonding ligands, these potential issues could resolved. The

potential for this additional parameter provided by the octahedral geometries of these octahedral

LL′CT complexes that can be used to tune their D-A properties represents another possible

advantage of these complexes over traditional square-planar D-A LL′CT dyes.

5.4 Summary

A unique LL′CT system activated by the oxidation of Rh(I) nacnac phdi was observed in our

lab previously.[4] This system is a rare example of an octahedral analogue to the 'traditional'

square-planar D-A LL′CT dye design. We have performed a detailed DFT and TD-DFT

computational study gain insight into the electronic structure and the orbitals involved in the LL

′CT excitations of the previously reported (donor)Rh(phdi)X$_2$ dyes **1a**, **1b** and **2**. Additionally,

calculations were performed on two other model complexes where the nacnac donor was

replaced with NacAc and acac (**3** and **4**) to predict the effect of substitutions of the nitrogen for

oxygen on the electronic structure and LL′CT properties of these complexes.

The spectroscopic and electrochemical properties of (donor)Rh(phdi)X$_2$ D-A LL′CT dyes

may be controlled through modification of ligand electronics in a manner analogous to the d_8

(donor)M(acceptor) dyes. Additionally, the UV-vis-NIR spectra and electronic structure

calculations of complexes **1a** and **1b** indicate that the presence of the axial ligands provide an

additional variable with which to tune the frontier orbitals of these dyes. This study also shows

that it is possible to incorporate strongly oxidizing donor ligands in LL′CT complexes. Strongly

oxidized dyes are necessary if D-A LL′CT dyes are to be used for hole injection applications.

These complexes discussed in this chapter represent the foundation of a new class of octahedral

D-A complexes.

5.5 Experimental

Computational Details.

All calculations were performed using the TURBOMOLE program package. The geometric and electronic structures were optimized without symmetry constraints using the PBE[14,15], PBE0[16,17], B3LYP[18], and TPSSH[19,20] functionals. Geometry optimization calculations were performed with a polarizable split--ζ basis set [def2-SV(P)] while electronic and excited state properties were computed using a polarized triple-ζ basis set (TZVP).[27] All molecules were treated in the gas phase without accounting for solvent. The energy was converged to 10^{-7} Hartree. Mulliken population analyses [28] and plots were also obtained at the PBE/ TZVP level; the contour values were 0.045 for the molecular orbital plots.

5.6 References

1.   McCrory, C. C. L.; Jung, S.; Peters, J. C.; Jaramillo, T. F. *J Am Chem Soc* **2013**, *135*, 16977.
2.   Cummings, S.; Eisenberg, R. *J Am Chem Soc* **1996**, *118*, 1949.
3.   Shaffer, D. W.; Ryken, S. A.; Zarkesh, R. A.; Heyduk, A. F. *Inorg Chem* **2011**, *50*, 13.
4.   Shaffer, D. W.; Ryken, S. A.; Zarkesh, R. A.; Heyduk, A. F. *Inorg Chem* **2012**, *51*, 12122.
5.   Das, D.; Scherer, T. M.; Das, A.; Mondal, T. K.; Mobin, S. M.; Fiedler, J.; Luis Priego, J.; Jimenez-Aparicio, R.; Kaim, W.; Lahiri, G. K. *Dalton Trans.* **2012**, *41*, 11675.
6.   Zhang, C.-R.; Han, L.-H.; Zhe, J.-W.; Jin, N.-Z.; Wang, D.-B.; Wang, X.; Wu, Y.-Z.; Chen, Y.-H.; Liu, Z.-J.; Chen, H.-S. *Computational and Theoretical Chemistry* **2013**, *1017*, 99.
7.   Zhang, Y.-M.; Wu, S.-H.; Yao, C.-J.; Nie, H.-J.; Zhong, Y.-W. *Inorg Chem* **2012**, *51*, 11387.
8.   Das, D.; Sarkar, B.; Kumbhakar, D.; Mondal, T. K.; Mobin, S. M.; Fiedler, J.; Urbanos, F. A.; Jimenez-Aparicio, R.; Kaim, W.; Lahiri, G. K. *Chemistry–A European Journal* **2011**, *17*, 11030.
9.   Wächtler, M.; Guthmuller, J.; González, L.; Dietzek, B. *Coordination Chemistry Reviews* **2012**, *256*, 1479.
10. Das, A.; Scherer, T. M.; Mondal, P.; Mobin, S. M.; Kaim, W.; Lahiri, G. K. *Chemistry–A European Journal* **2012**, n.
11. Wang, Y.; Hauser, B. T.; Rooney, M. M.; Burton, R. D.; Schanze, K. S. *J. Am. Chem. Soc.* **1993**, *115*, 5675.

12. Li, Z.; Leed, N. A.; Dickson-Karn, N. M.; Dunbar, K.; Turro, C. *chemical Science* **2013**.
13. Cummings, S. D.; Cheng, L.-T.; Eisenberg, R. *Chem. Mater* **1997**, *9*, 440.
14. Perdew, J. P.; Burke, K.; Ernzerhof, M. *Phys. Rev. Lett.* **1996**, *77*, 3865.
15. Perdew, J. P.; Burke, K.; Ernzerhof, M. *Phys. Rev. Lett.* **1997**, *78*, 1396.
16. Adamo, C.; Barone, V. *J. Chem. Phys.* **1999**, *110*, 6158.
17. Ernzerhof, M.; Scuseria, G. E. *J. Chem. Phys.* **1999**, *110*, 5029.
18. Stephens, P. J.; Devlin, F. J.; Chabalowski, C. F.; Frisch, M. J. *J. Phys. Chem.* **1994**, *98*, 11623.
19. Staroverov, V. N.; Scuseria, G. E.; Tao, J.; Perdew, J. P. *J. Chem. Phys.* **2003**, *119*, 12129.
20. Staroverov, V. N.; Scuseria, G. E.; Tao, J.; Perdew, J. P. *J. Chem. Phys.* **2004**, *121*, 11507.
21. Masui, H.; Lever, A. B. P.; Auburn, P. R. *Inorg Chem* **1991**, *30*, 2402.
22. Fennis, P. J.; Budzelaar, P. H. M.; Frijns, J. H. G.; Orpen, A. G. *Journal of Organometallic Chemistry* **1990**, *393*, 287.
23. Perdew, J. P.; Ruzsinszky, A.; Tao, J. M.; Staroverov, V. N.; Scuseria, G. E.; Csonka, G. I. *Journal of Chemical Physics* **2005**, *123*.
24. Autschbach, J. *Spectroscopic Properties Obtained from Time-Dependent Density Functional Theory (TD-DFT)*; John Wiley & Sons, Ltd: Chichester, UK, 2006.
25. Laurent, A. D.; Jacquemin, D. *Int. J. Quantum Chem.* **2013**.
26. Neese, F.; Petrenko, T.; Ganyushin, D.; Olbrich, G. *Coordination Chemistry Reviews* **2007**, *251*, 288.
27. Weigend, F.; Ahlrichs, R. *Phys. Chem. Chem. Phys.* **2005**, *7*, 3297.
28. Mulliken, R. S. *J. Chem. Phys.* **1955**, *23*, 1833.